Since 1955

Strojniški vestnik
Journal of Mechanical Engineering

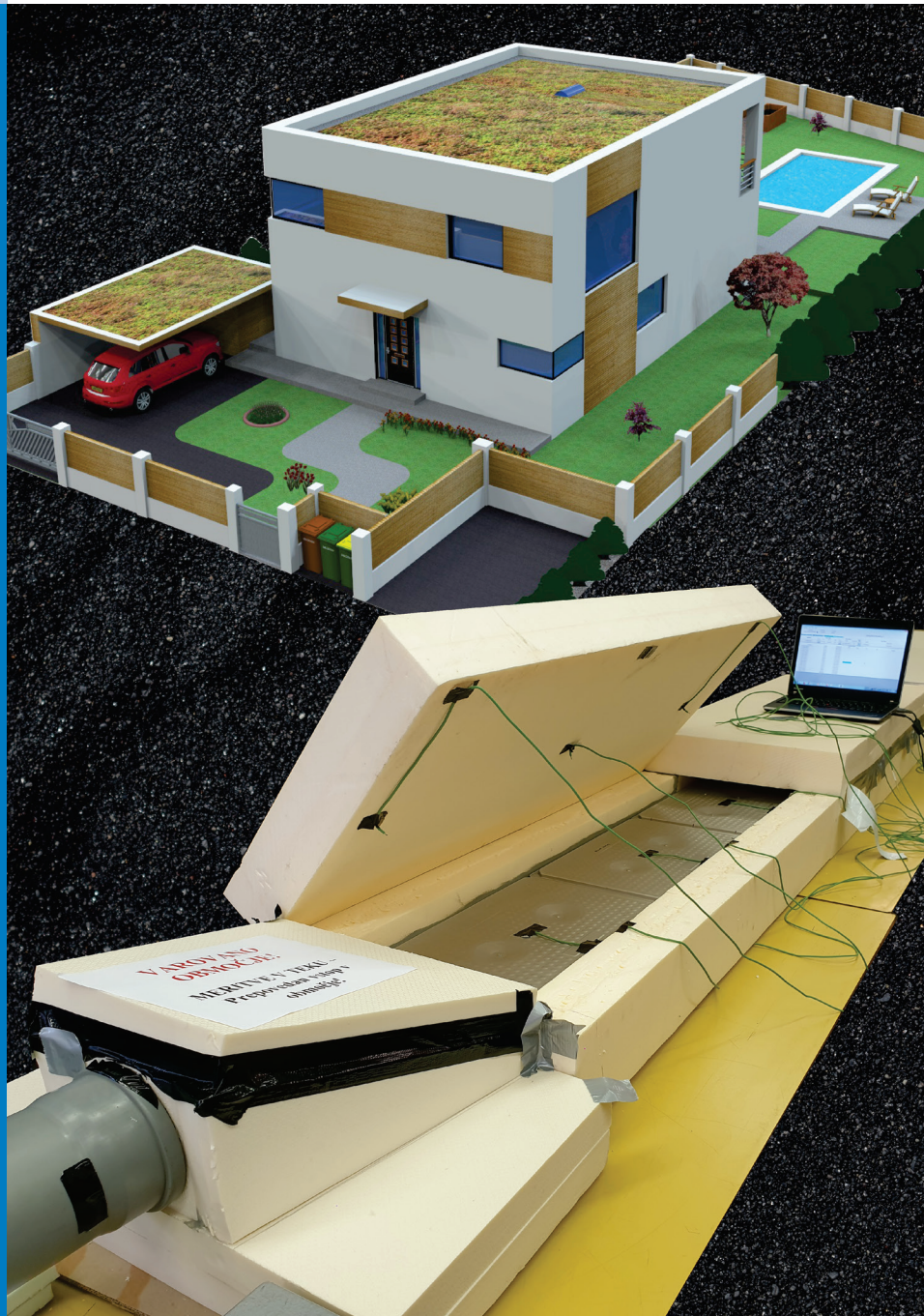

no. 1
year 2020
volume 66

Strojniški vestnik – Journal of Mechanical Engineering (SV-JME)

Aim and Scope
The international journal publishes original and (mini)review articles covering the concepts of materials science, mechanics, kinematics, thermodynamics, energy and environment, mechatronics and robotics, fluid mechanics, tribology, cybernetics, industrial engineering and structural analysis.
The journal follows new trends and progress proven practice in the mechanical engineering and also in the closely related sciences as are electrical, civil and process engineering, medicine, microbiology, ecology, agriculture, transport systems, aviation, and others, thus creating a unique forum for interdisciplinary or multidisciplinary dialogue.
The international conferences selected papers are welcome for publishing as a special issue of SV-JME with invited co-editor(s).

Editorial Office
University of Ljubljana, Faculty of Mechanical Engineering
SV-JME, Aškerčeva 6, SI-1000 Ljubljana, Slovenia
Phone: 386 (0)1 4771 137
Fax: 386 (0)1 2518 567
info@sv-jme.eu, http://www.sv-jme.eu

Print: Koštomaj printing office, printed in 275 copies

Founders and Publishers
University of Ljubljana, Faculty of Mechanical Engineering, Slovenia
University of Maribor, Faculty of Mechanical Engineering, Slovenia
Association of Mechanical Engineers of Slovenia
Chamber of Commerce and Industry of Slovenia, Metal Processing Industry Association

Cover:
The research presented in the journal is a preliminary study of decreasing building cooling needs with active/passive PCM.
Figure above shows a preliminary simulation with Designbuilder. Figure below represents an upgraded/preliminary study based experimental testing line in laboratory.

Image courtesy:
University of Ljubljana,
Faculty of Mechanical Engineering,
Laboratory for Heating, Sanitary, Solar and Air Conditioning Engineering, Slovenia

General information
Strojniški vestnik – Journal of Mechanical Engineering is published in 11 issues per year (July and August is a double issue).

Institutional prices include print & online access: institutional subscription price and foreign subscription €100,00 (the price of a single issue is €10,00); general public subscription and student subscription €50,00 (the price of a single issue is €5,00). Prices are exclusive of tax. Delivery is included in the price. The recipient is responsible for paying any import duties or taxes. Legal title passes to the customer on dispatch by our distributor. Single issues from current and recent volumes are available at the current single-issue price. To order the journal, please complete the form on our website. For submissions, subscriptions and all other information please visit: *http://www.sv-jme.eu.*

You can advertise on the inner and outer side of the back cover of the journal. The authors of the published papers are invited to send photos or pictures with short explanation for cover content.

We would like to thank the reviewers who have taken part in the peer-review process.

ISSN 0039-2480, ISSN 2536-2948 (online)

The journal is subsidized by Slovenian Research Agency.

Strojniški vestnik - Journal of Mechanical Engineering is available on *https://www.sv-jme.eu.*

Contents

Strojniški vestnik - Journal of Mechanical Engineering
volume 66, (2020), number 1
Ljubljana, January 2020
ISSN 0039-2480

Published monthly

Papers

Strojniški vestnik - Journal of Mechanical Engineering 66(2020)1, 3-14

DOI:10.5545/sv-jme.2019.6244
Original Scientific Paper
Received for review: 2019-07-12
Received revised form: 2019-10-01
Accepted for publication: 2019-10-10

Overheating Reduction in Lightweight Framed Buildings with Application of Phase Change Materials

Eva Zavrl[1] – Gašper Zupanc[2] – Uroš Stritih[1] – Mateja Dovjak[2,*]
[1] University of Ljubljana, Faculty of Mechanical Engineering, Slovenia
[2] University of Ljubljana, Faculty of Civil and Geodetic Engineering, Slovenia

The trend of lightweight framed building structures is gaining in popularity. Due to lower accumulation capability and thermal stability, buildings might be inclined to higher risk of overheating. The purpose of this study is to investigate overheating in lightweight framed buildings from the aspect of thermal comfort and energy efficiency in cooling season. Single-family house was modelled using DesignBuilder™ and located in moderate climate (Ljubljana, Slovenia). Heavyweight structure was compared to lightweight structure coupled with all 14 variations of phase change materials (PCM). Different strategies of PCM encapsulation (microencapsulated plasterboards, macroencapsulated additional layer), melting points (23 °C, 24 °C, 25 °C, 26 °C, 27 °C), capacities (M182, M91 M51, M27) and thicknesses (125 mm, 250 mm) of PCM were investigated and compared. The best passive solution was primarily evaluated based on the thermal comfort characteristics: average zone operative temperature (T_o) bends in cooling season. Secondarily, the additional energy needed for cooling within each solution was compared to the maximum allowed annual energy consumed for cooling specified in legislation. Consequently, the most influential parameter was the melting point of the PCM structure. Based on the chosen criteria, the overheating was significantly reduced using macroencapsulated layer with melting point of 24 °C and minimum capacity of M51 (max. T_o 26.3 °C). Heavyweight structure enabled lower T_o (27.1 °C) in the building compared to microencapsulated plasterboard solution with melting point at 23 °C and thickness of 250 mm (28.8 °C). Correctly designed passive solution can be used for the improvement of the design strategy and legislation towards overheating prevention.
Keywords: overheating, lightweight framed buildings, phase change materials, thermal comfort, energy efficiency

Highlights
- *The study shows that PCM in lightweight structure can completely reduce the energy needed for cooling by decreasing the temperatures for 1.2 °C more compared to the heavyweight structure.*
- *When reducing the overheating the heavyweight structure showed results comparable to PCM enhanced lightweight structure with melting point at 25 °C from the aspect of thermal comfort and energy efficiency.*
- *Microencapsulated PCM products are not sufficient for reducing the overheating.*
- *Overheating was completely reduced by using macroencapsulated PCM with melting point of 24 °C and minimum capacity of M51 in lightweight structure.*

0 INTRODUCTION

In accordance with the requirements of EU Regulation on construction products **[1]** are lightweight structures, as a part of building envelope system, describes as "structural loadbearing elements, which have to enable the required mechanical stability, at lower weight than it is general achievable by other heavyweight building structures". It can be reached either by decreasing the amount of material used for structure or by using higher rate of functionality within the lightweight structure **[2]**. The lightweight framed buildings (hereinafter lightweight buildings) are gaining in popularity in current construction and renovation, mainly due to shorter construction time; lower construction expenses and minimised environmental impact with higher reuse potential **[3]** and **[4]**. To control and prevent heat, water and sound transfer, protective layers - constructional products are added, in a function of thermal and sound insulations, waterproofing membrane, vapour barrier, etc. Additionally, lightweight construction is stimulated in many international and national policies and strategies based on lowering the carbon footprint **[5]**. The Kyoto protocol pushed the global market trend of lightweight buildings to grow to minimize global warming **[2]**.

Beside economic and environmental advantages, their weakness compared to heavyweight buildings is related to the performance and mutual relation to energy consumption and comfort. Thermally well insulated lightweight framed buildings prevent heat losses through their envelope and perform well when reducing the energy demand over the heating season. However, the heat capacity of the thermal insulation is relatively low. Thus, in summer time, it cannot accumulate the environmental heat. As a consequence, the building lacks thermal stability and its interior overheats **[6]**. This results in deteriorated thermal comfort over the summer time, also known as overheating.

The climate data show a trend of major global temperature growth **[7]**. According to the assumptions

*Corr. Author's Address: University of Ljubljana, Faculty of Civil and Geodetic Engineering, Chair of Buildings and Constructional Complexes, Jamova c. 2, 1000 Ljubljana, Slovenia, mdovjak@fgg.uni-lj.si

by Intergovernmental Panel on Climate Change (IPPC), due to human activity the global mean surface temperature grew up to 0.8 °C to 1.2°C above mean pre-industrial (1850 to 1900) level. With current grow rate the surface temperatures will increase for 1.5 °C between 2030 and 2052. Moreover, IPCC reports that the number of heat waves will increase and present a high to moderate risk to health **[7]**. Consequently, the temperatures in buildings will reach highly dangerous levels for the vulnerable population groups. Since 2014, the trend of heat related symptoms such as heat strokes and deaths was estimated to increase by 66 % until 2020 and 257 % until 2050 **[8]**.

Overheating mainly occurs due to low accumulation capabilities in dwellings, across the entire Europe, even in Northern European countries **[9]**. Since the overheating of modern lightweight prefabricated structures is an increasingly common problem on a global scale, a large number of scientific researches have recently studied it **[6]**. Most of the researchers either measured or simulated internal air temperatures or surface temperatures of the peripheral structural layers **[10]** and **[11]**. Some also involved the evaluation of thermal comfort with the help of various questionnaires, filled in by the by the occupants **[6]**.

Overheating is regulated by international and national legislation and is based on the qualitative and quantitative criteria of thermal comfort and energy efficiency. For example, CPR 305/2011 defines energy efficiency, hygiene and health needs as basic requirements for building as a whole and for constructional products **[1]**. European Directive on Energy Performance of Buildings (EPBD 2010/31/EU) explains that "the permissible annual cooling load required for cooling of residential buildings $Q_{(NC)}$, calculated per unit of cooled area $A_{(u)}$, shall not exceed 50 kWh per year per square meter area ($Q_{(NC)}/A_{(u)} \leq 50$ kWh/(m²a))" **[12]**. European requirements are implemented into national legislation. For example, Slovenian rules on efficient energy use in buildings require the maximum permissible value for cooling demand **[13]**. Similarly, the Slovenian Environmental Public Fund - ECO Fund defines the limit for heating demand for co-funding conditions **[14]**. On the other hand, the thermal stability of a building is a direct indicator of overheating in correlation to the structural complex. Thermal stability is usually described through air temperature, as suppression factor ν or phase delay η. These values are usually not defined with legislation. However, one of the rear criteria for thermal stability in healthcare facilities is the fraction of the massive structure within the building, published in Spatial Technical Guideline for Health Facilities in Slovenia, recommended that "at least 25 % of exterior wall's floor level height should present the massive building material on its inner side" **[15]**. Moreover, the Slovenian rules on the ventilation and air conditioning of buildings and also American and European standards define the limiting value of operative temperature during the cooling season to be 26 °C **[16]** to **[18]**.

Therefore, the strategy for preventing overheating in buildings depends on the building design. In order to prevent and control overheating, comprehensive measures are needed that follow the holistic principles of bioclimatic planning all the way to the introduction of passive and active building systems **[19]**. Phase change materials (PCM) can be used in buildings as both active or passive systems. Due to their high heat capacity they present an alternative to improve the thermal stability of a lightweight structure, as proved in many studies **[10]**, **[11]** and **[20]**. First example of PCM for heat storage applications in buildings in Slovenia presents research by Orel et al. **[21]**. These studies experimentally and numerically showed that PCM could reduce overheating during the entire year and improve the thermal comfort of the occupants. However, studies evaluated the performance of PCM either on the level of single surface temperature or based on the air temperature. However, air temperature does not report the effect of radiant temperature and is a limited parameter within thermal comfort analyses.

The purpose of this study is to investigate overheating in lightweight buildings from the aspect of thermal comfort and energy efficiency in cooling season. The main criterion for thermal comfort is the operative temperature (T_o) and for the energy efficiency, the energy cooling demand.

According to the purpose of this research, a model of a typical single-family house was located in a moderate climate. A comparative study of the influence of lightweight and heavyweight structure on overheating of the interior spaces was conducted. Additionally, PCM as passive system for the reduction of overheating problems was applied in the model and tested. The research goals were:

1. To compare four types of exterior walls, namely heavyweight, lightweight, lightweight coupled with additional PCM layer and lightweight with macro encapsulated PCM in plasterboard;
2. To determine the impact of influential parameters of PCM products, namely the encapsulation strategy, melting point, capacity and thickness;
3. To prove that overheating is present, even if the existing criteria (based on the operative

temperature and energy consumption for cooling) do not indicate it;
4. To define the optimal solution simultaneously within both criteria. The defined solution can then be used for the improvement of the design strategy and legislation.

1 METHODS

The comfort is assessed based on air and operative temperature data and the energy efficiency based on the energy consumed for mechanical cooling (active cooling). The chosen case was a family house with net floor area of 177.45 m², located in moderate climate, Ljubljana Slovenia. The geometry of the building is shown in Fig. 1. The chosen case study presents a typical prefabricated lightweight single-family house, currently expanded on the Slovenian market.

Fig. 1. *Front of the building*

DesignBuilder™ v3.4 was used as a calculation tool for the determination of energy consumption (of HVAC, lighting and operation) [22]. The geometry was inserted and the simulation conditions specified as below in Table 1. The model performed calculation within one thermal zone. Most of the data remained unchanged, unless specified otherwise. Different types of structural complexes (SC) of the building's envelope are shown in Figs. 2 to 5 with corresponding characteristic in Table 2. The first type is the heavyweight (HW) type of external wall, which bears the load with a thick layer of the bricks. The second type is the lightweight (LW) SC, which bears the weight with timber elements (frame). In order to improve the thermal capacity characteristics of LW, $LW_{PCM.a}$ and $LW_{PCM.b}$ present two different strategies of PCM installation. The strategies vary in PCM location among the layers of SC and in the way that PCM is implemented (macroencapsulated and microencapsulated). The first strategy (designated by symbol 'a') is macroencapsulated PCM blanket. It is attached as a single additional layer on the inner side of the exterior wall, right after the plasterboard. The second strategy (designated by symbol 'b') is microencapsulated and has a final layer of plasterboard improved with PCM microcapsules. The PCM product used within the first strategy – macroencapsulated additional layer of PCM ($LW_{PCM.a}$) is commercially called BioPCM™.

Table 1. *Simulation conditions*

Fixed input data	Value
Clothing insulation	0.5 clo
CO_2 emissions	(The amount was defined based on the function of the space)
Occupancy rate	/
Internal heat gains	/
Air leakage of all SC*	0.7 ac/h, constant
Thermal transmittance of the windows (U_W)	1.058 W/(m²K)
Total solar energy transmittance (g)	0.579
Shading type:	blinds outside
Light gains	
Ventilation	hybrid ventilation; (1 ACH**)
Air conditioning	The inclusion point was set when the internal air temperature exceeded 26 °C and the coefficient of cooling efficiency was 3.2
Season	Summer (1.8. to 7.8.2002)***
	Whole year 2002
Location	Ljubljana Slovenia
PCM melting point (initial)****	25 °C and thickness

*Structural complex (SC), **Air change per hour (ACH), ***The hottest week in 2002, for 5 days the outdoor temperature exceeded 30 °C, ****Phase change materials (PCM)

There are several different melting points available (27 °C, 25 °C and 23 °C) as in product abbreviations 27Q, 25Q and 23Q. Within the chosen melting point, various capacities can be chosen, namely M182, M91, M51, M27 [23] to [25]. BioPCM™ material is produced out of fatty acids and their derivatives, such as alcohols, amines and esters [26]. Its characteristics are: latent heat (L): 210 J/g to 250 J/g, energy storage capacity ($c_{p,e}$): 400 kJ/m² to 1250 kJ/m², specific heat (s): 2.2 J/(gK) to 4.5 J/(gK), thermal conductivity (λ): 0.15 W/(mK) to 2.5 W/(mK) and relative density (RD): 0.85 g/(mL) to 1.4 g/(mL). The PCM used for the second strategy (PCM_b) is a plaster board with addition of microcapsules of paraffin [27]. Characteristics

of the PCM_b are: thermal conductivity (λ) 0.23 W/(mK), density (ρ) 880 kg/m^3, board weight (W) 11 kg/m^2 where PCM weights 2 kg/m^2, heat capacity (c_p) 12.76 kJ/(kgK) and 1.17 kJ/(kgK), melting peak (T) 23 °C and thickness (d) 1.25 cm (commercially determined thickness of the plasterboard). Descriptions of the various SC of the external wall types are shown in Figs. 2 to 5.

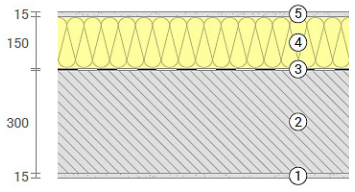

Fig. 2. *SC of the external heavyweight wall; ① plaster 15 mm, ② brick 300 mm, ③ polyethylene foil, ④ expanded polystyrene, ⑤ 150 mm, and ⑥ facade plaster 15 mm*

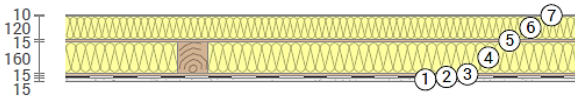

Fig. 3. *SC of the external lightweight wall with timber elements; ① gypsum cardboard 15 mm, ② polyethylene foil, ③ wooden panel 15 mm, ④ wooden frame with cellulose flakes 160 mm, ⑤ oriented strand board (OSB) panel 15 mm, ⑥ mineral wool panels, and ⑦ facade silicone plaster 10 mm*

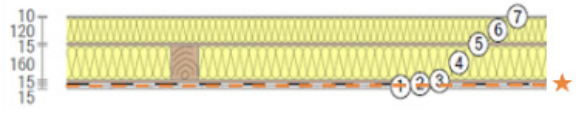

Fig. 4. *SC of the external lightweight wall with timber elements with macroencasulated PCM layer; ① gypsum cardboard 15 mm, *Additional layer of PCM on top of the LW.WF – melting point 25 °C and thickness of 7.4 cm (BIO PCM® M182/Q25), ② polyethylene foil, ③ wooden panel 15 mm, ④ wooden frame with cellulose flakes 160 mm, ⑤ oriented strand board (OSB) panel 15 mm, ⑥ mineral wool panels, and ⑦ facade silicone plaster 10 mm*

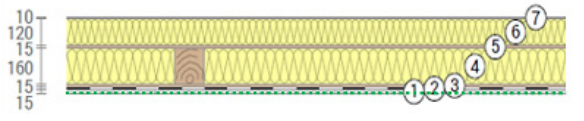

Fig. 5. SC of the external lightweight wall with timber elements with microencasulated PCM in gypsum board; ① gypsum cardboard with PCM 12.5 mm, ② polyethylene foil, ③ wooden panel 15 mm, ④ wooden frame with cellulose flakes 160 mm, ⑤ oriented strand board (OSB) panel 15 mm, ⑥ mineral wool panels, and ⑦ facade silicone plaster 10 mm

Within the simulation, the performance parameters of the structural complexes were determined based on the calculation procedure presented in ISO 7726:1998 **[28]**.

Table 2. *Heat transfer coefficients U [W/(m^{2}K)] of the designed structural complexes*

U [W/(m^{2}K)]	*HW*	*LW*	$LW_{PCM.a}$	$LW_{PCM.b}$
Exterior wall	0.201	0.139	0.130	0.138
Roof	0.182	0.111	0.111	0.111
Floor	0.260	0.260	0.260	0.260

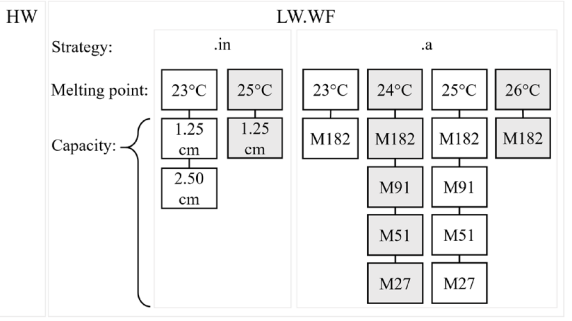

Fig. 6. *Systematic scheme of variations investigated and obtained results*

Fig. 6 explains the research approach with input data, simulation variations and physical quantities of the results. LW was chosen as a typical representative of the lightweight wooden building where summer overheating occurs. PCM type 'a' and type 'b' were chosen as standard solution strategies to overcome summer overheating (variation: strategy). PCM solutions applied on LW are compared to the traditional massive building type (HW). In order to investigate the impact of different variations on the results, other variations were tested as well. Within the type 'a' strategy, the PCM layer of all capacities with various melting point temperatures (23°C (PCM.a.23), 24°C (PCM.a.24), 25°C (PCM.a.25), 26°C (PCM.a.26) and 27°C (PCM.a.27)) was investigated (variation: melting point temperature). Afterwards, the effect of capacity of PCM.a.25 was tested by decreasing the initial capacities from M182 to M91, M51 and M27 (PCM.a.25.182, PCM.a.25.91, PCM.a.25.51 and PCM.a.25.27 respectively) (variation: heat capacity). Because the comparable PCM product was available only for the melting points of 23 °C, 25 °C and 27 °C, the characteristics (enthalpy – air temperature relation) of products with MP at 24 °C and 26 °C had to be manually determined. Characteristics of PCM.a.24 (if capacity is not designated, it is referred to as all: 27 to 182) were determined based on the linear interpolation between PCM.a.23 and PCM.a.25 and for PCM26.a.26.182 between PCM.a.25.182 and PCM.a.27.182. Within the second strategy type 'b', two different melting point temperatures were investigated. Similar approach was used to determine

the characteristics of PCM.b.25, where the properties were extrapolated from PCM.b.23. To validate this method, two simulations were performed. First, the exact values (enthalpy – air temperature relation) obtained from the research by Soares et al. were used to simulate case **[29]**. Second, the values were extrapolated from PCM.b.23 to the exact case of the plasterboard (PCM.b.23) by following the referred approach. The results obtained from simulating with 2 different types of values had negligible deviations. PCM.b.23 was tested for two thickness, 1.25 cm and 2.50 cm (PCM.b.23.125 and PCM.b.23.150, respectively) and PCM.b.25 for one thickness 1.25 cm (PCM.b.25.125). To evaluate the performance of the structural complexes, thermal comfort and energy consumption were investigated. The data were extracted as: outdoor air temperature [°C], inner air temperature and operative temperature [°C], delay and overheating recalculated out of T_{ai} and T_o [h] and the energy consumed for cooling the building [kWh] when T_{ai} and T_o exceeded the recommended limit. The upper and lower limits of T_{ai} and T_o were defined within Category III of indoor environment during the cooling season determined in EN15251:2007 **[18]**. The upper and lower limits for T_{ai} are 26 °C and 23 °C and for T_o 27 °C and 22 °C, respectively. The same limits stand when determining the electricity consumed for cooling to keep the building running within these limits. The electricity – electrical chiller is in case of thermal comfort investigations switched OFF and in case of energy efficiency investigations turned ON. The results are presented for the 1st week of August (as the week with the highest outdoor air temperatures of the TRY) and for the entire year. List of variations: HW; LW; $LW._{PCM.a.23}$: M182/Q23; $LW._{PCM.a.24}$: M182/Q24, M91/Q24, M51/Q24 and M27/Q24; $LW._{PCM.a.25}$: M182/Q25, M91/Q25, M51/Q25 and M27/Q25; $LW._{PCM.a.26}$: M182/Q26; $LW._{PCM.a.27}$: M182/Q27; $LW_{PCM.b.23}$: two thicknesses of 1.25 cm and 2.50 cm and $LW_{PCM.b.25}$: thickness of 1.25 cm.

2 RESULTS

The results of the analysis of overheating from the aspects of thermal comfort are presented with operative temperatures. The energy cooling demand is defined with [kWh/m²] needed for cooling.

2.1 Evaluation of Thermal Comfort Based on Operative Temperatures T_o

Fig. 7 shows the outdoor air temperature (T_{ao}) which presents the environmental conditions during which T_{ai} and T_o were measured. The horizontal dash line shows maximum (27 °C) operative temperature for obtaining the thermal comfort in the summer time determined in EN15251:2007 (static method) **[18]**. The first column set always shows the maximum temperatures obtained and the second column set the minimum temperatures obtained. The graphs always show operative temperatures on y-axis, but in case of 'Outside Dry-Bulb Temperature', where air temperatures are presented. The other two columns present the types of building external wall structures without PCM. The operative temperatures obtained in the space with the heavyweight wall (HW) are presented by the diagonal line patterned column and the lightweight wooden frame (LW) is presented with light grey column.

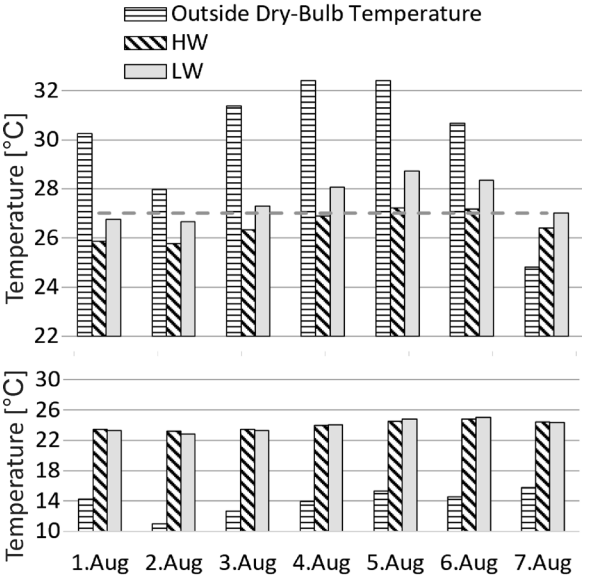

Fig. 7. *Temperatures [°C] obtained with HW and LW structure during the 1st week of Aug (max. temperatures in 1st set of columns and min. temperatures in 2nd)*

The results indicate that the T_o of the HW structure slightly (max. +0.2°C) exceeded the upper limit of 27 °C on 5th of Aug (14:00 to 18:00 h) and Aug, 6th of Aug (13:00 to 16:00 h). The maximum T_o reached with LW structure is 28.7 °C on the 5th of Aug at 17:00. However, the temperature exceeded the upper limit also on the 4th, 6th and 7th of Aug. Compared to LW, the HW structure alone, was less responsive to the outdoor temperature fluctuations.

Fig. 8 shows the results obtained with the LW structure alone and with PCM strategy type b – microencapsulated gypsum boards. The melting points were at 23 °C (1.25 cm and 2.50 cm) and at 25°C (1.25 cm). Compared to LW, the application of

microencapsulated PCM with the melting point of 23°C and thickness of 1.25 cm ($LW_{PCM.b.23.125}$) does not affect the temperature fluctuations. The peak temperature is reached at 28.8 °C at 17:00 (5th of Aug). Similar was shown with $LW_{PCM.b.23.250}$, where the double thickness negligibly softened the main temperature peak to 28.6 °C. Thus, the melting point of 23 °C is inappropriate choice for such building type and such climate conditions. On the other hand, the usage of $LW_{PCM.b.25.125}$ slightly reduced the daily maximum temperatures. The main peak from 5th of Aug was reduced by 0.8 °C (to 27.9 °C).

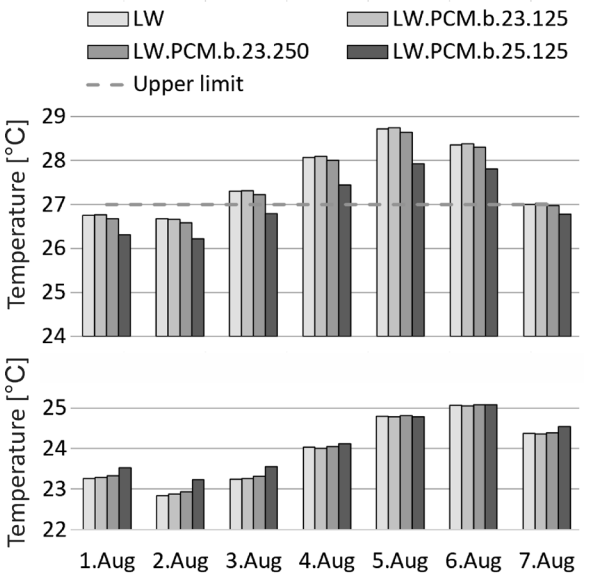

Fig. 8. T_o [°C] obtained with *microencapsulated (.b) strategy during the 1st week of Aug (max. temperatures in 1st set of columns and min. temperatures in 2nd)*

Fig. 9 shows the performance of strategy type a– the additional layer of macroencapsulated PCM on the inner side of the exterior walls at five different melting points (23 °C, 24 °C, 25 °C, 26 °C and 27 °C) within single capacity (M182).

Compared to LW, the macroencapsulated strategy with the melting point of 23°C (LWPCM.a.23.182) reduced T_o during the first exceeding peak (4th of Aug at 17:00) by 0.6 °C (from 28.1 °C to 27.5 °C). However, the second and the third peak were not affected (5th of Aug (17:00 h) and 6th of Aug (15:00 h)). LWPCM.a.25.182 and LWPCM.a.26.182 fluctuated similarly. The maximum T_o obtained was close to the upper limit. On 5th of Aug (17:00 h), with PCM.a.25.182 and LWPCM.a.26.182, the obtained max. To were 27.3 °C (–1.5 °C) and 27.0 °C (–1.8 °C), respectively. LWPCM.a.24.182 could sufficiently decrease the maximum T_o during the hottest week of the year below the upper limit.

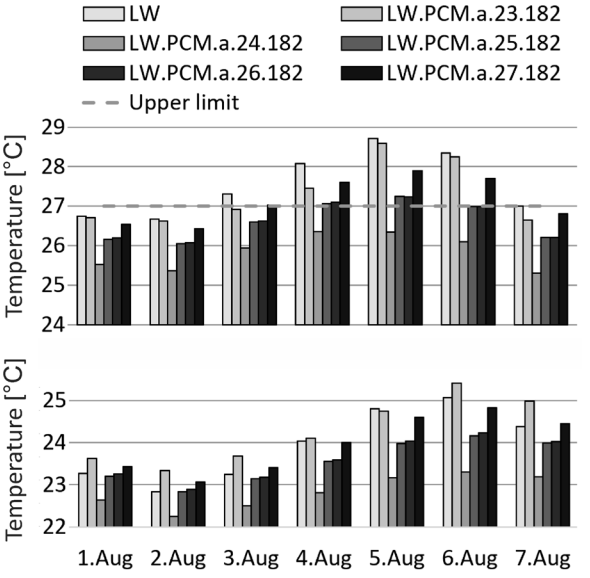

Fig. 9. T_o *[°C] obtained with macroencapsulated (.a) strategy during the 1st week of Aug (max. temperatures in 1st set of columns and min. temperatures in 2nd)*

Both strategies ('b' and 'a') within the melting point of 23 °C compared are shown in Fig. 10.

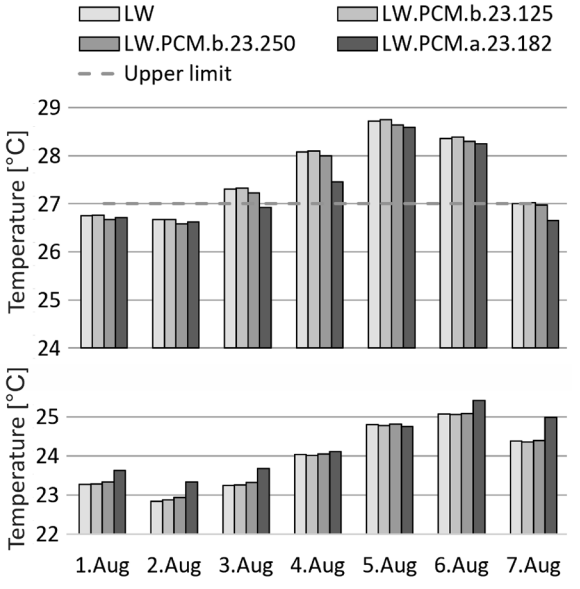

Fig. 10. T_o *[°C] obtained with both PCM strategies with the melting point of 23 °C during the 1st week of Aug (max. temperatures in 1st set of columns and min. temperatures in 2nd)*

$LW_{PCM.a.23.182}$ has the highest capacity among all cases shown in Fig. 10. Regardless from its high accumulation capabilities, it buffers only the first

peak, but not the last two (5th and 6th of Aug). In addition to the figures above (Figs. 7 to 9), it could be concluded that, the mis-determination of the melting point cannot be corrected to the addition of thermal capacity. $LW_{PCM.a.25.182}$ is an existing product with three lower capacities available (M91, M51 and M27) (Fig. 11).

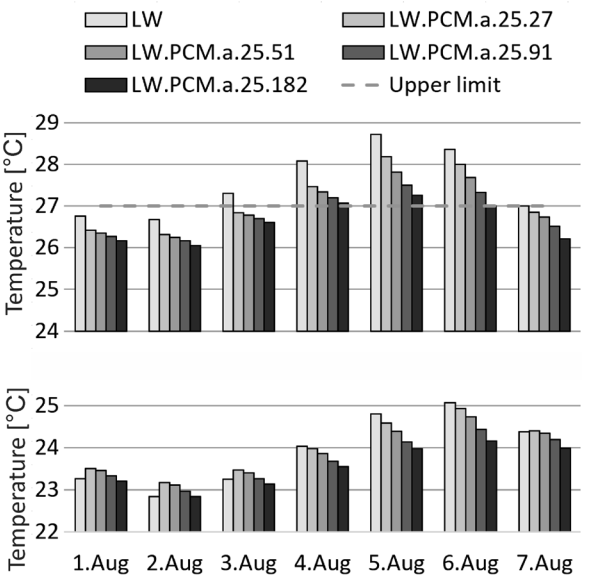

Fig. 11. *T_o [°C] obtained with $LW_{PCM.a.25}$ and various heat capacities during the 1st week of Aug (max. temperatures in 1st set of columns and min. temperatures in 2nd)*

In Fig. 10, different capacities had almost no effect on the performance of the PCM. From Fig. 11 it is clear, that lower capacities within the same melting point affected the results. All of the peaks from the 4th to the 7th of Aug would increase with decreasing capacity. This is most clear within the highest peak from the 5th of August, where T_o would increase from 27.3 °C to 27.5 °C, 27.8 °C and 28.2 °C with M91, M51 and M27, respectively. The performance of $LW_{PCM.a.25.91}$ is similar to the thermal performance of HW.

In Fig. 12, the variations of different capacities of $LW_{PCM.a.24.182}$ are presented. The question is, what is the lowest capacity that can still keep the temperatures below the upper limit.

On the 5th of Aug (17:00 h), $LW_{PCM.a.24.182}$ reduced the maximum peak of LW by 2.4 °C (from 28.7 °C to 26.3 °C). $LW_{PCM.a.24}$ can keep T_o peaks below the upper limit in all studied cases, except in the case with the lowest capacity investigated ($LW_{PCM.a.24.27}$). With the case of $LW_{PCM.a.24}$, the importance of the well-chosen melting temperature is stressed. In this way, also the costs of the material could be reduced. When using $LW_{PCM.a.24.91}$, compared to $LW_{PCM.a.24.182}$, T_o fluctuations remained almost unchanged. The maximum T_o obtained was 26.5 °C, which is only 0.2 °C higher compared to M182. With $LW_{PCM.a.24.51}$, T_o remained below the upper limit, but the maximum increase was to 26.9 °C, which is nearly the upper limit. The capacity of $LW_{PCM.a.24.27}$ would not be large enough to hold T_o below the limit. Thus the maximums exceed it up to 28.2 °C. The fluctuations in Figs. 11 and 12 were similar, without any phase delays.

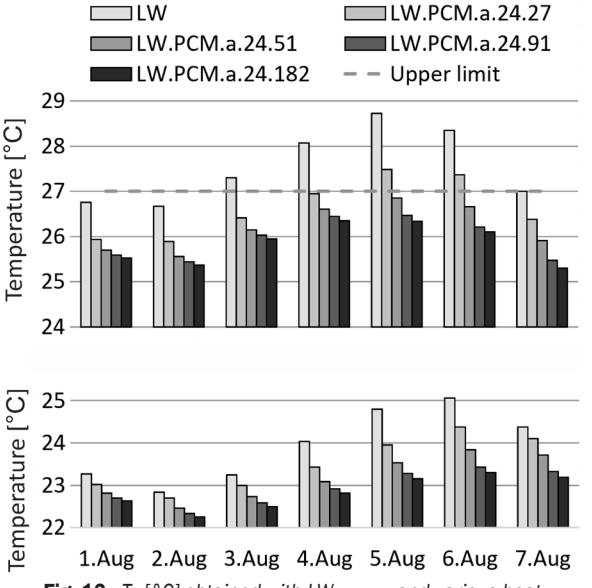

Fig. 12. *T_o [°C] obtained with $LW_{PCM.a.24}$ and various heat capacities during the 1st week of Aug (max. temperatures in 1st set of columns and min. temperatures in 2nd)*

2.2 Energy Efficiency Evaluated Based on the Hours of Overheating

Table 3 shows the number of hours above which the upper air temperature (T_{ai}) and operative temperature (T_o) limits were higher than the defined upper limit. Table 3 shows the hours for the two existing products that were closest to the real usage.

Table 3. *The number of hours of overheating (OH) [h] based on T_{ai} in T_o (1st week of August)*

Type	HW	LW	LWPCM .a.25.182	LWPCM .b.23.125
T_{ai} > 26°C	51	66	48	66
T_o > 27°C	6	30	6	30

Besides T_o, Table 3 includes also T_{ai}, as the T_o limit is chosen for Category III of indoor environment

and could thus be misleading (inaccurate) [18]. As can be seen from Table 3, the number of OH varies strongly in dependence of the strategy. Overheating occurred in both chosen existing cases. Consequently, the building's interior was overheated. The OH was zero in non-existing cases of $LW_{PCM.a.24.182}$, $LW_{PCM.a.24.91}$, and $LW_{PCM.a.24.51}$. For OH reduction, additional cooling with active system is required. Table 4 shows the amount of electrical energy needed to cool the rest of the existing products ($LW_{PCM.b.23.125}$ and $LW_{PCM.a.25.182}$).

Table 4. *Amount of electrical energy needed for cooling* $Q_{(NC)}/A_{(u)}$ *[kWh/m²]*

Type	HW	LW	LWPCM .a.25.182	LWPCM .b.23.125
$Q_{1st.A}$	1.4	1.5	1.3	1.5
Q_y	7.4	9.7	8.4	9.6
$Q_{1st.A} - Q_y$	19%	16%	15%	16%

2.3 Energy Performance Evaluated Based on the Energy Consumed for Cooling

Table 4 presents the energy needed to cool the building to the required operative temperature limits with electric chiller for the 1st week of Aug ($Q_{1st.A}$) and for the entire year (Q_y), per m² of the building. The importance of the 1st week of August is shown in the last row of the table (the percentage of energy consumed for cooling over the first week compared to the entire year), where it is specified that up to 19 % of the total yearly cooling demand can be consumed in the first week of August. The correctly chosen passive system ($LW_{PCM.a.24.182;}$ $LW_{PCM.a.24.91}$ and $LW_{PCM.a.24.51}$) could reduce the yearly demand by 16 % or more.

3 DISCUSSION

Within the first few days (1st to 3rd of Aug), in all of the investigated cases the temperatures remained below the upper limit of thermal environment. On the 4th of Aug, in most of the cases (exception is $LW_{PCM.a.24}$), T_o grew above the upper limit at 13:00 h. On the next day, 5th of Aug, T_o of all the cases exceeded the upper limit and also reached the peak with 1 or 2 hour delay. Afterwards (6th and 7th of Aug), T_o started to decrease. In order to compare the PCM solution to overheating with the traditional building concept, the comparison of the daily T_o peaks of various lightweight framed building combinations to the heavyweight building should be performed (Table 5). When observing the performance of HW structure during the highest daily peaks, it is possible to observe that during the cooler days (1st to 3rd of Aug) the HW structure could reach lower temperatures than in the rest of the cases (exc. $LW_{PCM.a.24}$), as apparently the material used for its mass (brick) accumulates the heat better than the PCM with chosen melting points. However, from the 4th of August on (5th to 7th of Aug), the HW structure could not keep the temperature peaks lower than in the cases with PCM with melting points of 25 °C and 26 °C ($LW_{PCM.a.25.182}$ and $LW_{PCM.a.25.91}$ and $LW_{PCM.a.26.182}$). Also other studies [6], [10], [30] to [33] reported that lightweight assembly compared to heavyweight assembly showed higher air temperatures within identical external conditions.

Table 5. *Temperature differences* T_o *[°C] of the maximum* T_o *obtained with HW and optional case showing positive values*

LW.PCM.	a.23.182	a.24.27	a.24.51	a.24.91	a.24.182	a.25.91	a.25.182	a.26.182
Aug 1st	-0.6	0.0	0.2	0.4	0.4	-0.3	-0.2	-0.3
Aug 2nd	-0.3	0.0	0.2	0.3	0.4	-0.3	-0.2	-0.2
Aug 3rd	-0.5	0.0	0.3	0.4	0.5	-0.2	-0.1	-0.1
Aug 4th	-0.5	0.1	0.4	0.5	0.6	-0.2	-0.1	0.1
Aug 5th	-0.9	0.0	0.4	0.8	0.9	-0.1	0.0	0.2
Aug 6th	-0.8	0.0	0.6	1.0	1.2	0.0	0.2	0.9
Aug 7th	0.2	0.2	0.6	1.0	1.1	0.1	0.3	0.6

The next group of the results is the minimum temperatures obtained in the night time. The minimum temperatures were obtained in the night time, but they never dropped below the lower limit. During the night time, in all of the cases the temperatures were suitable for occupant's sleep.

The first influential parameter of the PCM solution is the strategy. For example, Vik et al. found that 17 m² (Q23/M51) applied on the wall and ceiling of an office of 15 m² floor area reduced the $T_{o,max}$ by about 2 °C or even more, when facing the occupant [34].

The second influential parameter is the melting point. The effect of different melting points was tested. It was shown that the effect of the melting point is stronger compared to the effects of the other two influential parameters (strategy and capacity). Similar findings were mentioned by other studies, such as Pajek et al. [10]. Further, Reddy et al. [35] investigated the temperature of the inside (base) layer in the roof of a building located in Chennai (India) with different melting temperatures, thicknesses and numbers of PCM layers (single- or multi-layer) by using computer

fluid dynamics (CFD). They showed that when choosing the correct PCM melting point combination, the temperature of the layer remained unchanged during the whole daily cycle, even when changing the thicknesses of the PCM layers. The studies support the present findings and expose the importance of the correctly chosen melting point temperatures.

The studies are also in agreement with the conclusions regarding the capacity. The capacity should be large enough to absorb the excess heat and keep the temperatures below the upper limit. If the capacity is too low (i.e. $LW_{PCM.a.24.27}$), then T_o will exceed the comfortable indoor levels. If the capacity is too high (and the strategy and melting point suitable), then the solution is not cost and environmentally optimised. The surplus of the material results in deterioration of the LCA grade for the entire building complex. There is the possibility of self-insulation. As a result, over night the excess material is not completely solidified.

Additionally, the solidification of the PCM may be increased by increasing the ventilation rate in the building. Higher amounts of conditioned (cooled) air remove the heat from the PCM with convection and in this way accelerate its solidification. The increased performance of the PCM was additionally proven within some of the studies **[10].** Moreover, the increased volume flow rate often results in higher velocities in the occupied zones. This affects the thermal comfort (i.e. T_o) and may cause draught to the occupants. However, the energy consumed for the preparation of additional inlet air increases, which results in higher energy consumption for cooling.

Overheating hours as one of the analysed indicators of the presence of the overheating, numerically specifies the OH. Another possibility is coupling the passive strategy with the active one. The number of hours may be determined also with other criteria, such as improved weather files for heat wave analysis **[36]** or focusing on the periods outside the heat waves when the heat is accumulated in the environment **[37]**.

Energy performance shows the amount of energy needed for cooling during certain period. The results of this study correlate with other studies, proving that the correct application of PCM decreased the electrical consumption for cooling. For example, it was shown that a correct usage of PCM can improve overheating reduction from 7 % to 34 % **[38]**. A similar numerical study performed in TRNSYS showed that the PCM in walls combined with thermal insulation reduced the energy costs up to 66.2 % compared to the uninsulated envelope without PCM **[39]**. Reddy et al. showed that using double layered PCM (25 % to 35 %) reduced the heat gains more, compared to single layer PCM (17 % to 26 %) **[35]**.

The limitations of this study are: lack of CFD simulation within the zones, a lack of experimental measurements, the model does not consider the heatwaves. In this stage of our research we focused on one building case study with different building envelopes, where material properties (strategy, capacity and melting point) were variated.

4 CONCLUSIONS

To prevent overheating, a holistic approach based on bioclimatic design principles is needed, where the building is adapted to climate and location characteristics **[19]** and **[40]**. Secondly, a passive system with PCM (system) should be introduced to attain its maximum potential and system efficiency. Based on the study it can be concluded that:

- The presented system can increase the thermal comfort of the building and reduce the cooling demand;
- Results of this study showed that the macroencapsulated layer with melting point of 24 °C and minimum capacity of M51 results in simultaneous attainment of cooling demand (1.25 kWh/m²) and thermal comfort conditions with lower operative temperature (max. T_o 26.3 °C);
- With precise selection of influential parameters (melting point, capacity/thickness) the operative temperatures and energy consumption of lightweight structure are decreased more than in heavyweight structure;
- In order to attain its highest efficacy, it is important to select PCM with optimum melting point temperature, since the mis-determination of the melting point cannot be corrected by the addition of thermal capacity (the melting point at 23 °C has almost no effect on the performance of the lightweight structure and couldn't reduce the overheating at both thicknesses tested);
- The combinations of PCM with multi-layers of different melting points may also be applied in order to cover different temperature ranges;
- Macroencapsulated strategy has the potential to increase the capacity and is thus, more practical for usage;
- The system is highly applicable for the renovation of existing lightweight buildings or geometrically complex structures in the building envelope, by not losing the delicate amount of the floor area in the building;

In the future, the effectiveness of PCM operation should be investigated. The combination of numerical model on micro-scale and macro-scale and also a material for both cooling and heating season will be investigated considering [20]. Furthermore, the research should focus on material discharge (night-time ventilation or water pipe system in the neighbouring layer) and modelling the most efficient combination of a two PCM layers with different melting points. Nevertheless, the system should be investigated in the realistic environment of the single-family house. Also, another subject of further research should be the improvement of international and national legislation in order to define, qualitatively and quantitatively, indicators for the prevention of overheating. The indicators should be specified on the level of buildings, building systems and the environment, including the characteristics of: shading, transparent and non-transparent parts of building envelope (thermal stability, delays, accumulation capabilities, etc.). Active solutions should be coupled with bioclimatic and passive solutions and the limit amount of electricity consumed for cooling with mechanical systems should be defined.

5 ACKNOWLEDGEMENTS

The authors acknowledge the financial support from the Slovenian Research Agency (research core funding No. P2-0158, Structural engineering and building physics and No. P2-0223, Heat and Mass Transfer).

6 NOMENCLATURES

ρ	density, [kg/m³]
$c_{p,e}$	energy storage capacity, [kJ/m²]
c_p	heat capacity, [J/(kgK)]
d	thickness, [cm]
g	total solar energy transmittance, [-]
L	latent heat, [J/g]
λ	thermal conductivity, [W/(mK)]
OH	number of hours of overheating, [h]
RD	relative density, [g/(mL)]
s	specific heat, [J/(gK)]
T	melting peak, [°C]
T_{ai}	indoor air temperature, [°C]
T_{ao}	outdoor air temperature, [°C]
T_o	operative temperature, [°C]
$T_{o,max}$	maximum operative temperature, [°C]
$Q_{(NC)}/A_{(u)}$	amount of electrical energy needed for cooling, [kWh/m²]
$Q_{1st.A}$	electrical energy needed for cooling during the 1st week of Aug, [kWh/m²]
Q_y	electrical energy needed for cooling during the entire year, [kWh/m²]
$Q_{1st.A\text{-}Qy}$	energy consumed for cooling over the 1st week compared to the entire year, [%]
W	weight, [kg/m²]
U	heat transfer coefficient, [W/(m²K)]
U_W	thermal transmittance of the windows, [W/(m²K)]
v	temperature suppression factor, [-]
η	phase delay, [h]

7 REFERENCES

[1] CPR no. 305/2011. Regulation (EU) No 305/2011 of the European Parliament and of the Council of 9 March 2011 laying Down Harmonised Conditions for the Marketing of Construction Products and Repealing Council Directive 89/106/EEC (Text with EEA Relevance), *Official Journal of the European Union*, Strasbourg.

[2] De Geetere, L., Ingelaere, B. (2014). A new building acoustical concept for lightweight timber frame constructions. *Internoise, 43rd International Congress on Noise Control Engineering*, p. 1-8.

[3] Höglmeier, K., Weber-Blaschke, G., Richter, K. (2017). Potentials for cascading of recovered wood from building deconstruction—A case study for south-east Germany. *Resources, Conservation and Recycling*, vol. 117, p. 304-314, **DOI:10.1016/j.resconrec.2015.10.030**.

[4] Asdrubali, F., Ferracuti, B., Lombardi, L., Guattari, C., Evangelisti, L., Grazieschi, G. (2017). A review of structural, thermo-physical, acoustical, and environmental properties of wooden materials for building applications. *Building and Environment*, vol. 114, p. 307-332, **DOI:10.1016/j.buildenv.2016.12.033**.

[5] Ministry of Infrastructure (2018). Amendment to Long-Term Strategy for Mobilising Investments in the Energy Renovation Of Buildings, from: *https://www.energetika-portal.si/fileadmin/dokumenti/publikacije/dseps/dopolnitev_dseps_feb_2018.pdf* accessed on 2019-06-08. (in Slovene)

[6] Adekunle, T. O. and Nikolopoulou, M. (2016). Thermal comfort, summertime temperatures and overheating in prefabricated timber housing. *Building and Environment*, vol. 103, p. 21-35, **DOI:10.1016/j.buildenv.2016.04.001**.

[7] Intergovernmental Panel on Climate Change, (2018). Global Warming of 1.5 °C, *from:https://unfccc.int/news/unfccc-secretariat-welcomes-ipcc-s-global-warming-of-15degc-report*, accessed on 2019-05-12.

[8] Hajat, S., Vardoulakis, S., Heaviside, C. and Eggen, B. (2014). Climate change effects on human health: projections of temperature-related mortality for the UK during the 2020s, 2050s and 2080s. *Journal of Epidemiology and Community Health*, vol. 68, no. 7, p. 641-648, **DOI:10.1136/jech-2013-202449**.

[9] Eurostat. (2012). Share of Population Living in a Dwelling Not Comfortably Cool during Summer Time by Income Quintile and Degree of Urbanization, *from:https://ec.europa.eu/eurostat/*

data/database?node_code=ilc_hcmp03, accessed on 2019-04-04.

[10] Pajek, L., Hudobivnik, B., Kunič, R. and Košir, M. (2017). Improving thermal response of lightweight timber building envelopes during cooling season in three European locations. *Journal of Cleaner Production*, vol. 156, p. 939-952, **DOI:10.1016/j.jclepro.2017.04.098**.

[11] Arkar, C., Domjan, S. and Medved, S. (2018). Lightweight composite timber façade wall with improved thermal response. *Sustainable Cities and Society*, vol. 38, p. 325-332, **DOI:10.1016/j.scs.2018.01.011**.

[12] EPBD 2010/31/EU, Directive 2010/31/EU of the European Parliament and of the Council of 19 May 2010 on the energy performance of buildings, from: *https://eur-lex.europa.eu/LexUriServ/LexUriServ.do?uri=OJ:L:2010:153:0013:0035:EN:PDF*, accessed on 2019-02-07.

[13] PURES (2010). Rules on efficient use of energy in buildings with a technical guideline (O.J. RS, no. 52/10 and 61/17 – GZ), from: *https://www.uradni-list.si/glasilo-uradni-list-rs/vsebina/98727*, accessed on 2019-02-07. (In Slovene)

[14] Slovenian Environmental Public Fund - ECO Fund. (2017). Conditions for obtaining grants in the construction or purchase of almost zero-energy new one or two-dwelling, from: *https://www.ekosklad.si/fizicne-osebe/nameni/prikazi/actionID=155*, accessed on 2019-04-25. (in Slovene)

[15] TSG-12640-001:2008. *Technical Guideline for Health Facilities*. Ministry of Health of Republic of Slovenia. (In Slovene)

[16] Rules on the ventilation and air-conditioning of buildings (O.J, no. 42/02) (2002). from: *http://pisrs.si/Pis.web/pregledPredpisa?id=PRAV4223*, accessed on 2019-04-25. (in Slovene)

[17] ANSI/ASHRAE Standard 55-2013. *Thermal Environmental Conditions for Human Occupancy*. American Society Of Heating, Refrigerating And A-C Engineers, Atlanta.

[18] EN 15251:2007:E. *Indoor Environmental Input Parameters for Design and Assessment of Energy Performance of Buildings Addressing Indoor Air Quality, Thermal Environment, Lighting and Acoustics*. European Committee for Standardization, Brussels.

[19] Manzano-Agugliaro, F., Montoya, F. G., Sabio-Ortega, A. and García-Cruz, A. (2015). Review of bioclimatic architecture strategies for achieving thermal comfort. *Renewable and Sustainable Energy Reviews*, vol. 49, p. 736-755, **DOI:10.1016/j.rser.2015.04.095**.

[20] Osterman, E., Butala, V. and Stritih, U. (2015). PCM thermal storage system for 'free' heating and cooling of buildings. *Energy and Buildings*, vol. 106, p. 125-133, **DOI:10.1016/j.enbuild.2015.04.012**.

[21] Orel, B., Maček, M., Krainer, A. (1993). Advanced phase change (PCM) materials for heat storage applications in buildings. *Solar Energy and Architectural Urban Planning – Proceedings at International Conference*, p. 111-114.

[22] DesignBuilder Software Ltd. (2107). *DesignBuilder Software Ltd - Home*, from: *https://designbuilder.co.uk//*, accessed on 2019-04-25.

[23] Phase Change (2018). BioPCM-Data-Sheet-Q27, from: *https://phasechange.com/technology/data-sheets/*, accessed on 2019-04-26.

[24] Phase Change (2018). BioPCM-Data-Sheet-Q25, from: *https://phasechange.com/technology/data-sheets/*, accessed on 2019-04-26.

[25] Phase Change (2018). BioPCM-Data-Sheet-Q23, from: *https://phasechange.com/technology/data-sheets/*, accessed on 2019-04-26.

[26] Phase Change (2017). Phase Change Materials. from: *https://phasechange.com/wp-content/uploads/2017/06/Phase-Change-Materials-BioPCMs-vs-Salt-Hydrates.pdf*, accessed on 2019-04-25.

[27] Knauf (2016). Generic Heat Storage Capacity Knauf Comfortboard 23, from: *http://micronal-pcm-app.de/files/2016-04-16_-_generic_heat_storage_capacity_comfortboard_23.pdf, accessed 2019-04-25*.

[28] ISO 7726:1998. *Ergonomics of the thermal environment – Instruments for measuring physical quantities,* International Organization for Standardization, Geneve.

[29] Soares, N., Gaspar, A. R., Santos, P., Costa, J. J. (2014). Multi-dimensional optimization of the incorporation of PCM-drywalls in lightweight steel-framed residential buildings in different climates. *Energy and Building*, vol. 70, p. 411-421, **DOI:10.1016/j.enbuild.2013.11.072**.

[30] Albatici, R., Genetti, F. and Marinelli, M. (2015). Summer comfort in exposed concrete free running buildings. *Energy Procedia*, vol. 78, p. 2935-2940, **DOI:10.1016/j.egypro.2015.11.671**.

[31] Mlakar, J., Štrancar, J. (2011). Overheating in residential passive house: Solution strategies revealed and confirmed through data analysis and simulations. *Energy and Buildings*, vol. 43, no. 6, p. 1443-1451, **DOI:10.1016/j.enbuild.2011.02.008**.

[32] Stazi, F., Bonfigli, C., Tomassoni, E., Di Perna, C. and Munafò, P. (2015). The effect of high thermal insulation on high thermal mass: Is the dynamic behaviour of traditional envelopes in Mediterranean climates still possible. *Energy and Buildings*, vol. 88, p. 367-383, **DOI:10.1016/j.enbuild.2014.11.056**.

[33] Jones, R. V. Goodhew, S. and De Wilde, P. (2016). Measured indoor temperatures, thermal comfort and overheating risk: Post-occupancy evaluation of low energy houses in the UK. *Energy Procedia*, vol. 88, p. 714-720, **DOI:10.1016/j.egypro.2016.06.049**.

[34] Vik, T. A., Madessa, H. B., Aslaksrud, P. Folkedal, E. and Øvrevik, O. S. (2017). Thermal Performance of an Office Cubicle Integrated with a Bio-based PCM: Experimental Analyses. Energy Procedia, *8th International Conference on Sustainability in Energy and Buildings*, vol. 111, p. 609-618, **DOI:10.1016/j.egypro.2017.03.223**.

[35] Reddy, K., Mudgal, V., Mallick, T., Reddy, K.S., Mudgal, V., Mallick, T.K. (2017). Thermal performance analysis of multi-phase change material layer-integrated building roofs for energy efficiency in built-environment. *Energies*, vol. 10, no. 9, p. 1367, **DOI:10.3390/en10091367**.

[36] Lomas, K.J., Porritt, S.M. (2017). Overheating in buildings: lessons from research. *Building Research & Information*, vol. 45, no. 1-2, p. 1-18, **DOI:10.1080/09613218.2017.1256136**.

[37] Gasparrini, A., Yuming Guo, Y., Hashizume, M., Lavigne, E., Zanobetti, A., Schwartz, J., Tobias, A., Tong, S., Rocklöv, J., Forsberg, B., Leone, M., De Sario, M., L Bell, M., Leon Guo, Z. L., Wu, C., Kan, H., Yi, S. M., De Sousa Zanotti Stagliorio Coelho, M., Nascimento Saldiva, P. H., Honda, Z., Kim, H. (2015). Mortality risk attributable to high and low ambient temperature: A multicountry observational study. *Lancet*, vol. 386, no. 9991, p. 369-375, **DOI:10.1016/S0140-6736(14)62114-0**.

[38] Jamil, H., Alam, M., Sanjayan, J., Wilson, J. (2016). Investigation of PCM as retrofitting option to enhance occupant thermal comfort in a modern residential building. *Energy and Buildings*, vol. 133, p. 217-229, **DOI:10.1016/j.enbuild.2016.09.064**.

[39] Panayiotou, G.P., Kalogirou, S.A., Tassou, S.A. (2016). Evaluation of the application of phase change materials (PCM) on the envelope of a typical dwelling in the Mediterranean region. *Renewable Energy*, vol. 97, p. 24-32, **DOI:10.1016/j.renene.2016.05.043**.

[40] Krainer A. (2008). Passivhaus contra bioclimatic design. *Bauphysik*, vol. 30, no. 6, p. 393-404, **DOI:10.1002/bapi.200810051**.

Strojniški vestnik - Journal of Mechanical Engineering 66(2020)1, 15-28

DOI:10.5545/sv-jme.2019.6002 Original Scientific Paper
Received for review: 2019-01-15
Received revised form: 2019-05-07
Accepted for publication: 2019-07-11

Heat Dissipation from Stationary Passenger Car Brake Discs

Stergios Topouris[1] – Dragan Stamenković[2,*] – Michel Olphe-Galliard[1] – Vladimir Popović[2] - Marko Tirovic[1]
[1] Cranfield University, School of Aerospace, Transport and Manufacturing, United Kingdom
[2] University of Belgrade, Faculty of Mechanical Engineering, Serbia

This paper presents an experimental investigation of the heat dissipation from stationary brake discs concentrated on four disc designs: a ventilated disc with radial vanes, two types of ventilated discs with curved vanes (a non-drilled and cross-drilled disc), and a solid disc. The experiments were conducted on a purpose-built thermal spin rig and provided repeatable and accurate temperature measurement and reliable prediction of the total, convective and radiative heat dissipation coefficients. The values obtained compare favourably with computational fluid dynamics results for the ventilated disc with radial vanes and solid disc, though the differences were somewhat pronounced for the ventilated disc. The speeds of the hot air rising above the disc are under 1 m/s, hence too low to experimentally validate. However, the use of a smoke generator and suitable probe was beneficial in qualitatively validating the flow patterns for all four disc designs. Convective heat transfer coefficients increase with temperature, but the values are very low, typically between 3 W/(m²K) and 5 W/(m²K) for the disc designs and temperature range analysed. As expected, from the four designs studied, the disc with radial vanes has the highest convective heat dissipation coefficient and the solid disc the lowest, being about 30 % inferior. Convective heat dissipation coefficient for the discs with curved vanes was about 20 % lower than for the disc with radial vanes, with the cross-drilled design showing marginal improvement at higher temperatures.
Keywords: brake disc, heat dissipation, convective cooling, computational fluid dynamics, natural convection

Highlights
- *Heat dissipation from stationary brake discs was investigated.*
- *It was done via a thermal spin rig test, computational fluid dynamics analysis, and a smoke generator test.*
- *Radial vanes provide the highest convective heat dissipation coefficient and solid disc the lowest, with curved vanes being in the middle.*
- *The cross-drilled design shows only marginal improvement.*

0 BACKGROUND

Brake cooling is vital for safe vehicle operation and has attracted substantial research from very early days; however, most research and published data relate to heat dissipation from rotating discs. Cooling of a stationary brake is equally important as many critical cases are related to this driving condition. For instance, brake fluid is much more likely to boil if the vehicle is not moving. The consequences can only become apparent once the vehicle starts moving again, making the situation safety-critical. Convective heat dissipation is drastically reduced, from predominantly forced cooling (at high airspeeds) to natural convection only (airspeed being zero). Instead of the heat being dissipated to the surrounding air, which is propelled away from the brake, much more heat is being transmitted to pads and calliper through conduction and radiation. Furthermore, a considerable portion of the heat being dissipated from the disc by natural convection is heating the calliper as the hot air is forced upwards by the natural convection. The air surrounding the brake assembly is "trapped" within the wheel and wheel arch cavities, and the brake ambient temperature is rapidly increasing, well above the outside ambient air temperature.

The situation might be equally critical during "hot parking" when the vehicle is parked after heavy brake use. In such conditions, some brake components can reach higher temperatures than for a moving vehicle. Traditionally, the risks with "hot parking" were related to the boiling of brake fluid, but vehicle "rollaway" is another potentially critical condition. As the disc and pads cool down they "shrink" (their thickness reduces) whereas the calliper expands as it heats up as a result of a heat transferred from the pads and disc. This leads to the reduction of the clamp force, causing decrease in friction force (braking torque) and potentially leading to rollaway if the vehicle is parked on a gradient. The condition is most critical when installing an electric parking brake (EPB) for which long flexible cables are not used, and there is no flexibility in the system to compensate for reduction in disc and pad thickness. EPB has brought hot parking to an entirely new level, ensuring safe vehicle parking on a gradient (specified at 20 % by UN Regulation No. 13-H [1]). The methodologies used to cope with this challenge include "over-clamping" (i.e., applying much higher force than required in order to "stretch" the calliper, which should compensate for disc and pad shrinkage) and re-parking (i.e., re-applying the brake automatically after the vehicle has been parked).

*Corr. Author's Address: University of Belgrade, Faculty of Mechanical Engineering, Kraljice Marije 16, Belgrade, Serbia, dstamenkovic@mas.bg.ac.rs

With the installation of electric and electronic components into callipers (EPB, "low drag" callipers, etc.), there is a potential danger with overheating and permanent damage to these parts; hence, accurate prediction of brake temperatures in parking conditions is becoming even more critical.

Heat dissipation from stationary brake is also vital for accurately predicting brake temperatures in drive cycles which contain periods when the vehicle is stationary. Though these cycles are typically not safety-critical from the brake performance point of view, brake temperatures are essential in understanding and minimizing residual drag, providing good brake pedal feel and reliably estimating brake wear.

Finally, braking of hybrid and electric vehicles (HEVs) imposes another braking challenge, in addition to complexities related to brake pedal feel, residual drag, and EPB. UN Regulation No. 13-H requires all braking tests (such as repeated brake applications – "fade and recovery") to be successfully performed by friction brakes only, without the use of regenerative braking. Considering that HEVs are typically heavier than equivalent cars with internal combustion engines only, understanding braking requirements is paramount not only regarding safety but also in order to minimize brake mass and resolve brake cooling in the most effective way for both moving and stationary vehicle operation. Though some of these vehicles are relatively low performance, there are some extremely high-performance HEVs with very rapid acceleration characteristics and therefore very high braking demands.

When analysing brake thermal aspects in parking conditions, it should be pointed out that critical cooling times can be quite prolonged; for passenger cars with conventional hand brake designs, rollaways are known to have occurred up to 30 minutes after the vehicle was parked with hot brakes. This was for "medium gradients" (~10 %); as for the higher gradients, the rollaway occurs much quicker. In commercial vehicles, the critical period can be up to 1 hour **[2]**.

As a first step in studying heat dissipation from stationary passenger car disc brake assemblies, the focus will be on the brake disc. Four types of brake discs will be studied, for two passenger vehicles. The first vehicle is Volkswagen Passat (Typ 3C) and the second Lotus Elise S2, with the basic vehicle and disc characteristics given in Table 1.

Brake discs are shown in Fig. 1, with Figs 1a and b presenting VW Passat front and rear discs, respectively. Lotus Elise S2 standard disc is marked Fig. 1c, with Fig 1d presenting a cross-drilled disc (the perspective of the photo can confuse the reader leading to the perception that Lotus discs are unequal in diameter). From Fig. 1 it can be noted that all three ventilated discs are of a "swan neck" type, meaning that the outboard disc friction face is attached to the top hat section but using a "swan neck" type feature in order to minimize disc coning. This design allows air intake from the inboard side, resulting in good cooling characteristics.

Table 1. *Vehicle characteristics*

Characteristics	VW Passat 2.0T FSI 2007	Lotus Elise S2 2011
Gross vehicle mass [kg]	2100	1141
Static front axle load [kg]	1080	570.5
Static rear axle load [kg]	1020	570.5
Wheelbase [mm]	2709	2300
Maximum engine power [kW]	147	89*
Maximum vehicle speed [km/h]	235	205
Front disc type	Ventilated with radial vanes	Ventilated with curved vanes**
Front disc outer diameter [mm]	321	288***
Rear disc type	Solid	Ventilated with curved vanes**
Rear disc outer diameter [mm]	286	288***

* Basic model
** Option: Cross-drilled
*** Front and rear discs are identical

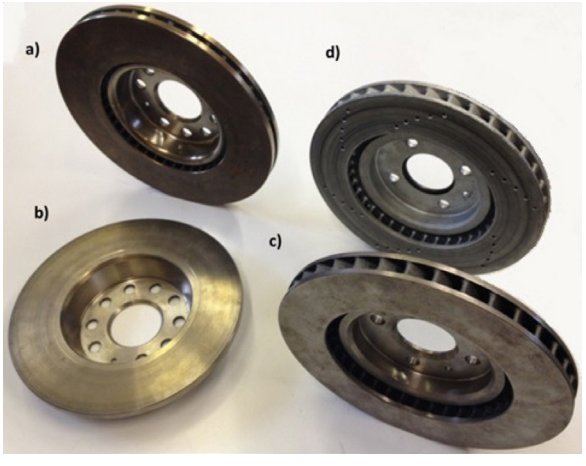

Fig. 1. *Discs Analysed - VW Passat: a) front, b) rear Lotus Elise S2: c) standard, d) cross-drilled*

Detailed design characteristics for all four discs studied are presented in Table 2. At the beginning of the research, all discs were brand new. To stabilize emissivity values they were repeatedly heated and cooled, which caused all surfaces to corrode. The front VW Passat disc (Fig 1a) is the largest and heaviest, owing to the high vehicle mass and maximum speed,

as well as brake force distribution (Front:Rear) of 2.1 for fully laden vehicle. Solid disc (Fig. 1b) has the smallest outer (OD) and inner (ID) diameters; it is the thinnest, has the smallest wetted area and is also the lightest at only 3.2 kg. It is worth pointing out that both vehicles have practically 50:50 static load distribution for fully laden condition.

Table 2. *Disc characteristics*

Fig. 1	Type / Design	OD × ID × thick. [mm]	No. of vanes [-]	Wetted area [m²]	Mass [kg]
a)	Ventilated with radial vanes	321 × 188 × 25	40	0.3086	9.4
b)	Solid	286 × 180 × 12	N/A	0.1678	3.2
c)	Ventilated with curved vanes	288 × 185 × 26	37	0.2562	4.2
d)	Ventilated with curved vanes, cross drilled	288 × 185 × 26	37	0.2586	4.18

In contrast, this substantially changes for unladen state of the VW Passat (with much more load taken by the front axle in unladen and partly laden conditions), there is practically no difference for Lotus Elise as the engine is mounted in the middle and in addition to the driver, there is only place for one passenger (next to the driver) and very little luggage. Consequently, neither the load nor the distribution per axle change much for Lotus. Without entering into further analyses into brake sizing and characteristics, a brief literature review will be presented, which will be followed by the modelling and experimental results obtained.

1 LITERATURE REVIEW

Due to its importance for safe vehicle operation, heat dissipation attracted considerable research attention from early days. However, complex geometry, installation, boundary conditions and service duties limited the application of analytical methods, and the work was predominantly experimental, aiming at measuring maximum brake temperatures at specific duties. The research was also mostly concerned with rotating discs, with analytical methods applied initially to a geometrically perfect disc shape (not an actual brake disc) rotating in still air **[3]**, and in a cross flow **[4]** and **[5]**. Heat dissipation was experimentally investigated in the past for brake discs installed on vehicle **[6]** and **[7]** or inertia dynamometer **[8]**, with the aim of establishing relationships and finding effective solutions in predicting brake disc temperatures. The ability to model the actual brake geometry came with the development of numerical methods (finite element and finite difference), but the complexity of boundary conditions still required substantial experimental work in establishing and validating temperature prediction procedures. Substantial contributions to solving the problem can be found in the literature **[9]** to **[12]**.

The development of computational fluid dynamics (CFD) made possible for actual boundary conditions, i.e., convective heat transfer coefficients, to be reliably theoretically predicted. Still, it took some time for these methods to be sufficiently developed for successful analyses of brake discs. Complex geometry, boundary conditions, and disc rotation required robust algorithms and very powerful computers to deal with models with millions of cells. Stationary disc analysis was not any easier to model. The disc does not rotate, but the energy for air flow is provided by change in air density due to its heating and expansion. Some useful CFD work for rotating disc analysis and optimization for automotive and railway discs is provided in the literature **[13]** to **[17]**.

There are only a few papers published and known to the authors dealing with CFD modelling in predicting temperatures and heat transfer coefficients for a stationary disc **[2]**, **[18]** and **[19]**, and are the results of studies conducted at Cranfield University. The conclusions are multifold but can be summarized in that effective CFD modelling of the stationary discs is possible; nonetheless, it requires meshes with a large number of elements and extreme care in their creation (in particular when modelling boundary layers). Obviously, powerful computers are needed and CPU times are considerable (typically over 48 hours). Menter's shear stress transport (SST) turbulence model was found to be the most suitable in terms of both accuracy and speed. The values of convective heat transfer coefficients are similar, but higher than the values quoted in this paper. This is due to much larger discs (outer diameter being 434 mm) heated to higher temperatures (over 350 °C). It was also concluded that flow patterns change with temperatures, and static disc cooling at higher temperatures can be reduced by the hot air exiting lower ventilation channels and blocking air entry into upper channels. This phenomenon was typical for large anti-coning type discs studied, but some evidence of similar effects has been also detected by the authors and will be presented and discussed later. The analyses **[2]** also employed analytical methods for heat transfer from surfaces (walls and cylinders), developed by other authors **[20]** to **[23]**. Very useful results have been obtained for a wide temperature range, but these are limited to solid discs only.

Convective heat dissipation prediction in friction brakes has been vastly improved in recent years, yet still considerably relies on experimental work. This is not limited to this mode of heat dissipation only, but also to radiative and conductive losses. Both these modes are speed independent, and the radiation is highly temperature-dependent. Consequently, appropriate modelling of these two modes is vital for accurate prediction of convective losses and brake temperatures in any operating duty. Substantial work and contribution in effectively tackling these modes can be found in the literature, for conductive heat transfer **[24]** and **[25]** as well as for radiation **[26]** and **[27]**. Accurate and reliable heat dissipation is required not only for safe prediction of brake temperatures regarding friction characteristics (fade) and brake components and fluid temperatures; it has much broader implications in lightweight designs and noise, vibration and harshness (NVH) characteristics **[28]** and **[29]**.

2 EXPERIMENTAL SET-UP

All tests presented in this paper were conducted on a specially designed thermal spin rig, with its computer-aided design (CAD) model shown in Fig. 2. The rig has an in-line arrangement of the motor, coupling, drive shaft and brake disc, with suitable bearing housing placed on a supporting frame/table. Fig. 3 shows the actual rig. In order to minimize conductive heat losses, contact areas of the disc with the mounting flange were insulated using a low conductivity temperature-resistant gasket (showing green in Fig. 3a). Furthermore, only two bolts were used to secure the disc, and the tightening torque was very low. The bolt contacts with the flange were also insulated by using polytetrafluoroethylene (PTFE) tape (seen white in Fig. 3a). Interestingly, there was no measurable difference in the cooling rates if the insulation was not placed between contact surfaces. The explanation is that both heating and cooling periods were long and, if no insulation was used, the flange was heated to the same temperature and cooled down at a similar rate.

The operational procedure has three distinctive phases:

a) **Heating period**. The disc is rotating at low speed (~100 rpm), and the heater box is placed over the disc (see Fig. 3b) with hot air guns activated, providing a gradual, uniform disc heating. Once the disc reaches the required temperature, typically around 250 °C, the heating is turned off, with the disc continuing to rotate at low speed. Temperatures and other variables are logged during this period but typically not processed.

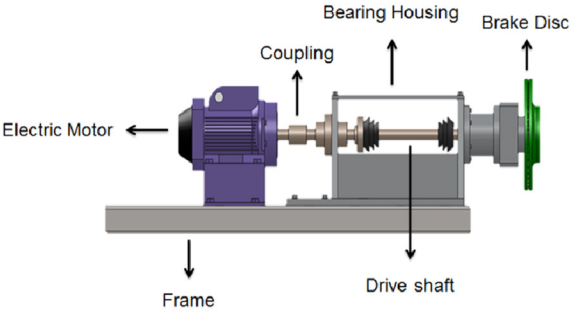

Fig. 2. *Thermal spin rig concept*

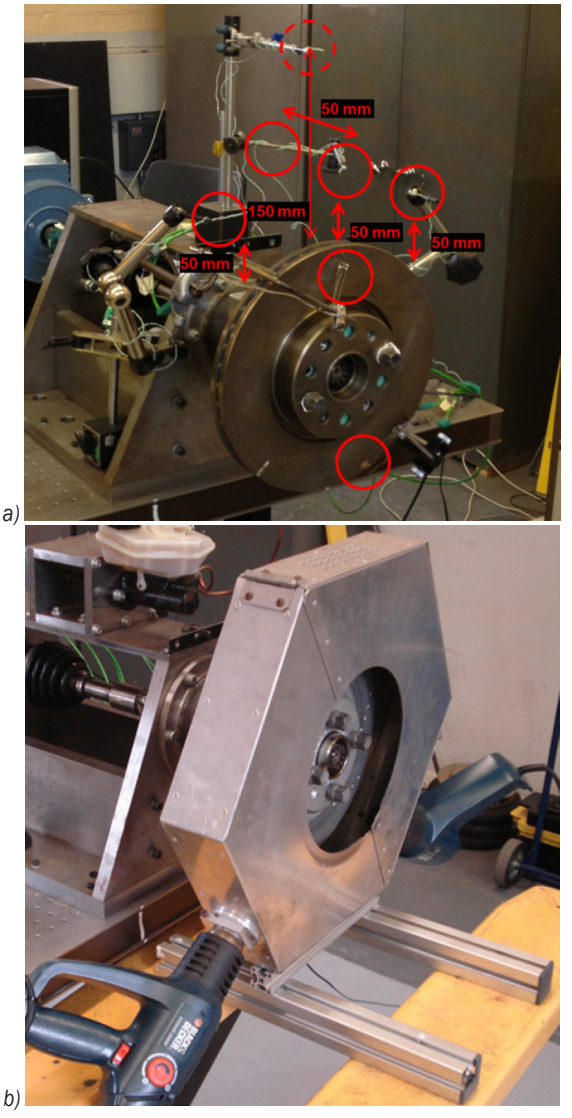

Fig. 3. *Thermal spin rig; a) thermocouples installed, b) heating box*

b) **Soaking period.** The disc is continuing to rotate at low speed for several minutes in order to equalize the temperatures. All variables are logged during this period for monitoring purposes but not typically processed. At the end of this period the heating box is removed.

c) **Cooling down period.** This period starts after the soaking period, and all variables are logged and processed during this period. The disc is typically cooled down to under 50 °C. Disc surface temperatures logged during this period make the actual "cooling curves" and are used to calculate average heat transfer coefficients.

The instrumentation used (see Fig. 3a) consisted of a number of rubbing/contact thermocouples (Fig. 4a, K Type, 0.5 mm diameter) which were positioned around the disc, contacting disc friction surfaces. It should be pointed out that the differences in measured disc temperatures across friction surfaces were very small. This is a result of low cooling rate and thick disc faces made of thermally highly conductive grey cast iron. Fig. 3a shows two contact thermocouples positioned 30 mm radially from the disc's outer diameter, on the bottom and top of the outboard friction face. Two more thermocouples were placed at the same nominal position on the inboard friction surface. The temperature of the air in the plume above the disc was measured using 5 thermocouples, positioned above the disc, as shown in Fig. 3a, using wire type thermocouples (Fig. 4b, also K Type, 0.5 mm diameter). Ambient temperature was measured in 4 places around the laboratory, and all doors and windows were closed to reduce air movement.

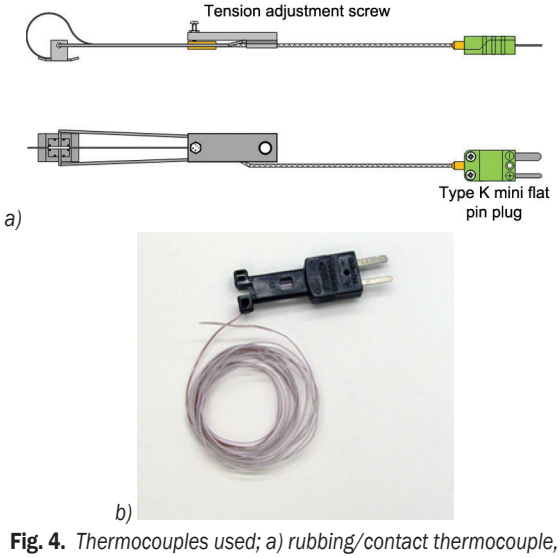

Fig. 4. *Thermocouples used; a) rubbing/contact thermocouple, and b) wire thermocouple*

For signal conditioning and data logging, National Instruments CompactDAQ was used connected to a personal computer, together with NI 9211 thermocouple modules (Fig. 5). The developed code enabled direct temperature measurement and display during the cooling period, as well as the presentation of the entire cooling event, as shown in Fig. 6. It can be observed that all temperatures are very close and the cooling curves are smooth. Consequently, the temperatures can be suitably averaged and reliably used to calculate average heat transfer coefficients. The tests were repeated numerous times and nearly identical values were obtained. More details about the methodology, uncertainty and the results are available in **[2]** and **[30]**.

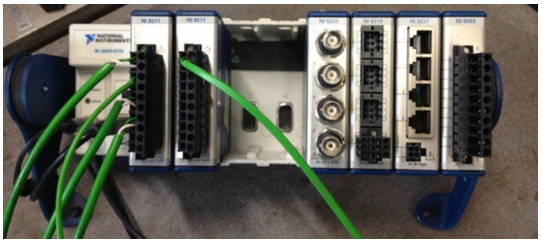

Fig. 5. *National Instruments CompactDAQ with thermocouple modules*

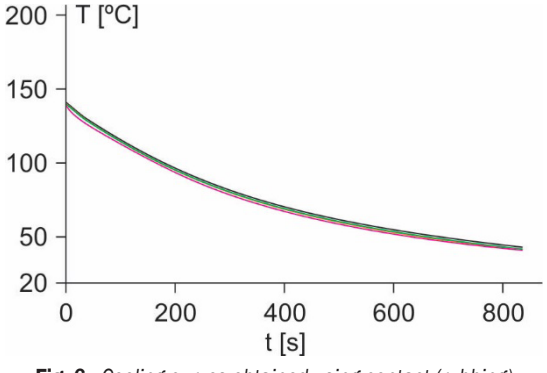

Fig. 6. *Cooling curves obtained using contact (rubbing) thermocouples*

In an attempt to obtain more temperature data across the friction face and hub flange area of the disc, a FLIR A320 thermal imaging camera was also used, with Fig. 7 showing the image and selected points for obtaining temperatures. Unfortunately, this was not providing useful results, as minor differences in disc surface condition lead to small differences in emissivity values, which in turn caused differences in obtained temperature readings. The differences were typically around 5 °C, but sometimes higher, even 10 °C or more, without any reason for the difference (except change in emissivity) and with

contact thermocouples showing identical temperatures in these areas. The cooling curves were smooth and averaging was possible. However, such differences in local temperatures were typically reducing but not diminishing as the disc was cooling down and even existed when the disc was approaching or reaching ambient temperature. Though the use of the infrared camera for temperature measurements of the fast rotating discs at high temperature was found useful by some authors and recently has much improved [27], for the considered disc, the temperature range and stable cooling condition, this method was not considered suitable.

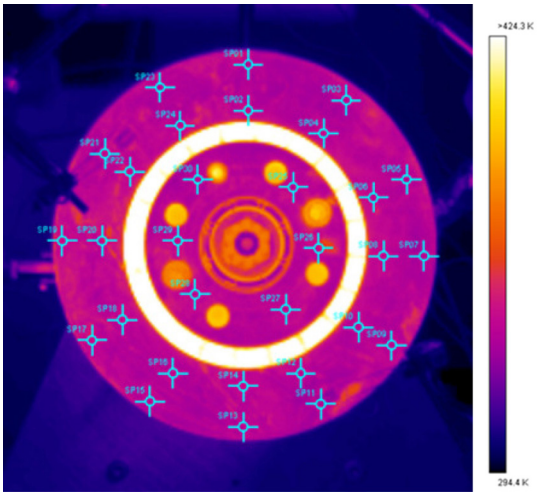

Fig. 7. *Full-field disc thermal image and selected points for infrared temperature measurement*

To compare the results with CFD predictions, an attempt was made to measure air temperatures of the plume above the disc, using wire thermocouples shown in Fig. 4b, with the positions marked in Fig. 3a. Unfortunately, this approach was found to be unsuitable. The temperature variations were irregular ("erratic"), despite every effort to prevent air movement in the laboratory. It is interesting to point out that this method was found reliable, but for much larger and heavier discs, heated to higher temperatures [2].

The problems with better understanding stationary disc cooling are not related to temperature measurements only. As will be shown, air speeds within the plume rising above the disc are also very low, typically under 1 m/s, making the air speed measurements practically impossible. Consequently, measuring disc surface temperatures using contact thermocouples was found to be the only reliable method and these results were used to calculate average heat transfer coefficients, which will be compared with CFD results. As will be shown later, some very useful but qualitative (only) indications of the flows were obtained using smoke generator.

3 CALCULATION OF AVERAGE HEAT TRANSFER COEFFICIENTS FROM MEASURED TEMPERATURES

As explained in the previous section, during the cooling period, there is no heat input. Therefore, the energy dissipated during the time t_1 to t_2 will be equal to the thermal energy loss from the disc. Consequently the average total heat transfer coefficient h_{tot} can be defined as:

$$h_{tot} = -\ln\left(\frac{T_{d2}-T_\infty}{T_{d1}-T_\infty}\right)\frac{m\cdot c_p}{A_w\left(t_2-t_1\right)}, \tag{1}$$

where T_{d2} is disc temperature at the time t_2, T_{d1} disc temperature at the time t_1, T_∞ ambient temperature, m disc mass, c_p specific heat of disc material (grey iron), and A_w total disc wetted area.

The average coefficient of heat transfer due to radiation during the period $(t_2 - t_1)$ can be defined as:

$$h_{rad} = \varepsilon\cdot\sigma\left(\frac{T_d^{\,4}-T_\infty^{\,4}}{T_d-T_\infty}\right)\frac{A_{rad}}{A_w}, \tag{2}$$

where ε is disc surface emissivity, σ Stefan-Boltzmann constant, A_{rad} radiative heat dissipation disc area, and T_d average disc temperature during the period $(t_2 - t_1)$.

Accordingly, the average convective heat transfer coefficient, for the period $(t_2 - t_1)$, can be calculated as:

$$h_{conv} = h_{tot} - h_{rad}. \tag{3}$$

As the disc cools down, the temperature will drop more slowly, hence keeping the same periods (t_2-t_1) for calculating average heat dissipation coefficients may not be the best approach. It was found very useful to keep the temperature differences $(T_{d2}-T_{d1})$ constant for conducting these calculations. Typically, temperature differences of around 20 °C are considered most suitable, providing reliable disc surface temperatures and sufficiently short periods to account for the highly non-linear influence of radiative heat losses. In order to determine disc surface emissivity, the thermal camera (explained above) was used, and the temperature was measured at the same time in the close proximity to the predefined points using contact thermocouples. After extensive surface mapping, an average emissivity value was established for the entire disc surface. There were some variations between discs (which were taken into consideration

when processing the data), but the overall average value was found to be $\varepsilon = 0.82$. It should be pointed out that the disc surface was oxidized, covered in fine corrosion after repeated heating and cooling. There were no pads to polish the disc surface, and the contact/rubbing thermocouples covered only small areas and caused little change to the surface emissivity in the contact paths with the disc (as the disc was rotating during the heating period, but the speeds and interface pressures were very low).

4 CFD MODELLING AND COMPARISON WITH EXPERIMENTAL RESULTS

CFD modelling for VW front and rear discs was conducted using CFX code [31].

4.1 CFD Mesh

Fig. 8 depicts a front ventilated disc model, with Fig. 8a showing the air domain, Figs. 8b and c surface mesh on the outboard and inboard side, respectively. Mesh detail in the area of channel entrance at disc inner diameter is shown in Fig. 8d, where very fine mesh with numerous small cells can be observed.

Figs. 9a and b show the rear solid disc, where the mesh did not require that many cells. Mesh statistics for the two discs are included in Table 3.

Table 3. *CFD Mesh statistics*

Characteristics	Ventilated disc (fine mesh)	Solid disc
Nodes (total)	3,295,654	857,655
Elements (total) of which:	12,117,247	3,226,623
Tetrahedral	8,825,745	2,406,319
Pyramids	112	287
Prisms	3,291,390	820,017

The total number of cells was over 12 million for the ventilated and over 3 million for the solid disc. It should be pointed out that such a fine mesh was necessary for modelling the air flow and heat transfer of stationary discs. A much lower number of cells was needed when modelling rotating disc or disc in a cross flow. A *K-ε* turbulence model was used for both discs, and the results will be first presented alongside qualitative experimental investigations using a smoke generator.

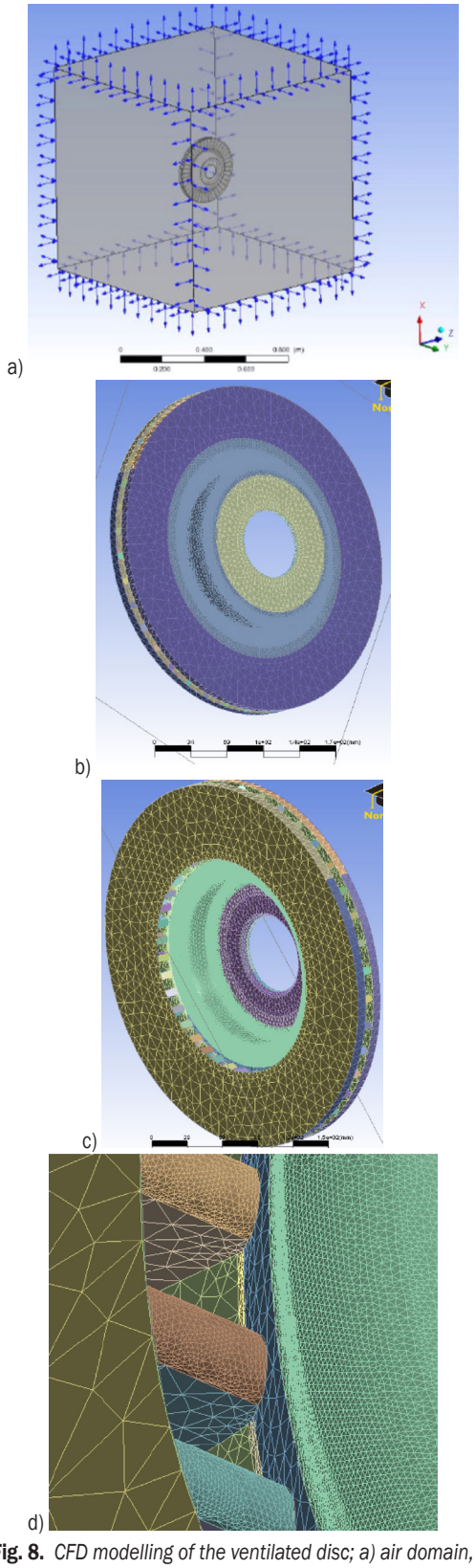

Fig. 8. *CFD modelling of the ventilated disc; a) air domain, b) surface mesh (outboard), c) surface mesh (inboard), and d) mesh detail*

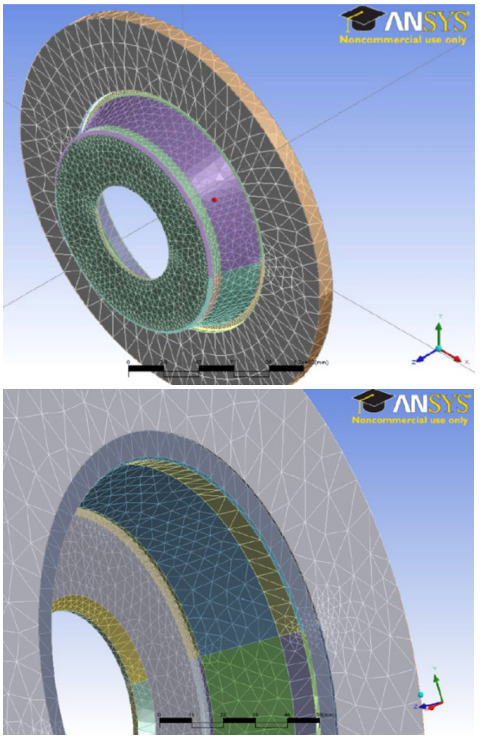

Fig. 9. *CFD Modelling of the solid disc; a) surface mesh and b) mesh detail*

4.2 Air Flow

Fig. 10a shows air velocity contours for the ventilated disc at 250 °C in the middle vertical plane (XZ, see Fig. 8a). It can be seen that the maximum velocity predicted is just over 0.9 m/s; therefore, it was not possible to conduct experimental validation. In order to validate flow pattern, tests were conducted using smoke generator with neutral buoyancy smoke (generated from special oil), with the fine probe releasing the smoke in various areas in the proximity to the disc. Fig. 10b shows the plume rising from the disc faces and channels, which closely resembles the CFD predictions displayed in Fig. 10a. It should be pointed out that, unfortunately, the disc could not be heated to 250 °C, the temperature used for CFD modelling.

The flow air patterns (such as Fig. 10b) are very difficult to photograph and obtain clear flow indications. The best approach established was to take videos and then play them frame by frame and select the clearest pictures with the highest contrast. This approach inevitably reduced picture resolution, with the disc cooling down during filming. The light also played an important part in taking useful images; too much or too little light made the smoke practically invisible or air plume direction difficult to understand. As expected, the cooling is most effective in the upper side of the disc and least effective in the channels which are in the horizontal position.

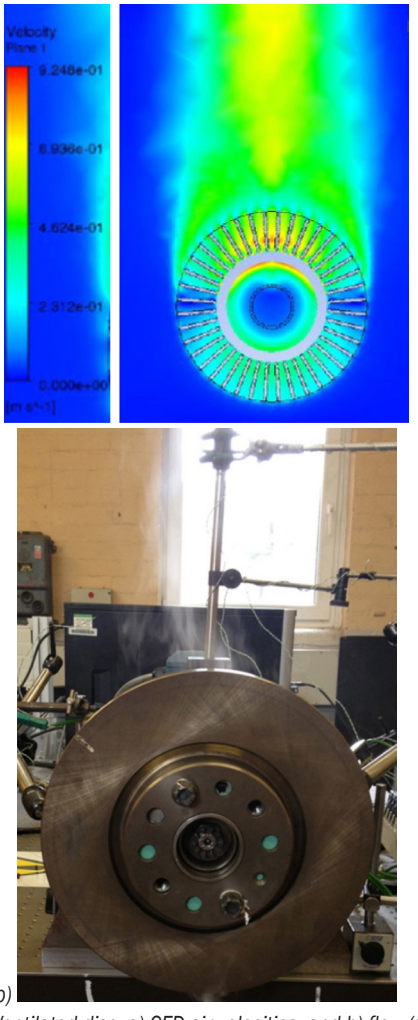

Fig. 10. *Ventilated disc: a) CFD air velocities, and b) flow (smoke) pattern using smoke generator*

Fig. 11a shows air velocity contours in the vertical plane YZ running through the disc axis, with 11b showing horizontal plane XY, again running through the disc axis. It can be observed that upwards air flow in the swan neck area, at disc inner diameter, blocks air entry into the ventilation channels. This phenomenon (effect) diminishes with a drop in disc temperatures. As a result, convective cooling does not drop as drastically as probably expected with disc cooling, owing to (proportionally) more air flow going through ventilation channels at lower disc temperatures.

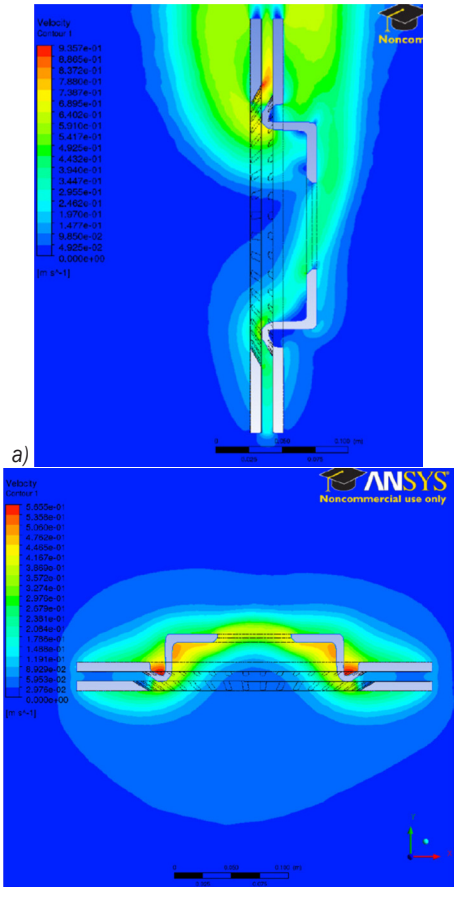

Fig. 11. *Ventilated disc predicted air velocity contours at 250 °C: a) YZ plane, and b) XY plane*

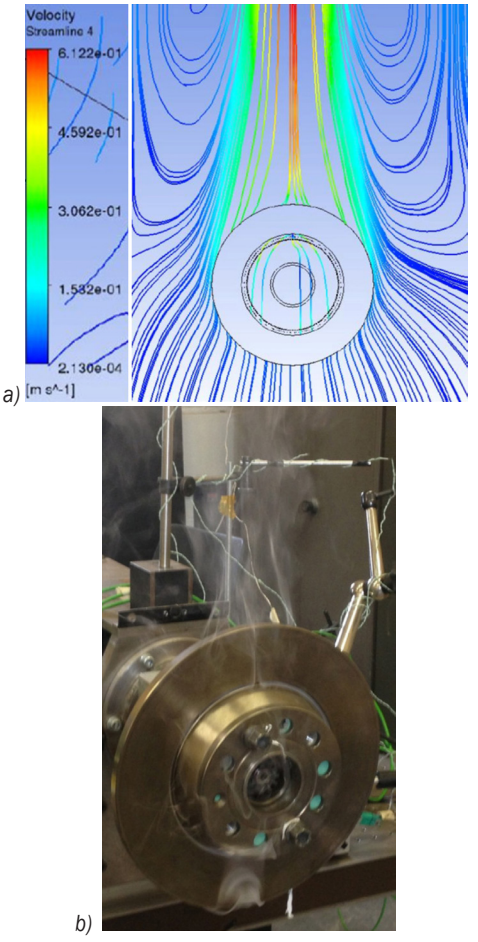

Fig. 12. *Solid disc: a) CFD air velocities, and b) flow (smoke) pattern using smoke generator*

Fig. 12 shows the solid disc. Again, CFD analyses were performed for 250 °C and experiments at 150 °C due to the limitation of the heating system. CFD air velocities are shown in the line form (Fig. 12a), and all indications are that the flow pattern matches very well with the visualization using the smoke generator shown in Fig. 12b. The maximum air speeds predicted were just over 0.6 m/s, more than one disc diameter above the disc, in the middle plane. Unfortunately, this value is very low and could not be experimentally verified but the smoke rising above the disc (Fig. 12b) clearly indicates the same pattern and position of the highest speed.

4.3 Air Temperatures

Despite not being able to accurately measure air temperatures, it is useful to look at the CFD results shown in Fig. 13 for the ventilated (Fig. 13a) and solid (Fig. 13b) discs at 250 °C (note the air temperature is shown in K). Air temperature seems to rapidly drop after rising above the disc. The plume is also relatively narrow. That probably best explains why the efforts in measuring air temperature were not successful in this case. In one study [2], air temperatures were successfully measured, but for much larger and heavier commercial vehicle brake discs heated to higher temperatures. The air temperatures shown in Figs. 13a and b match well with the air speed and flow patterns shown in Figs. 10a to 12b.

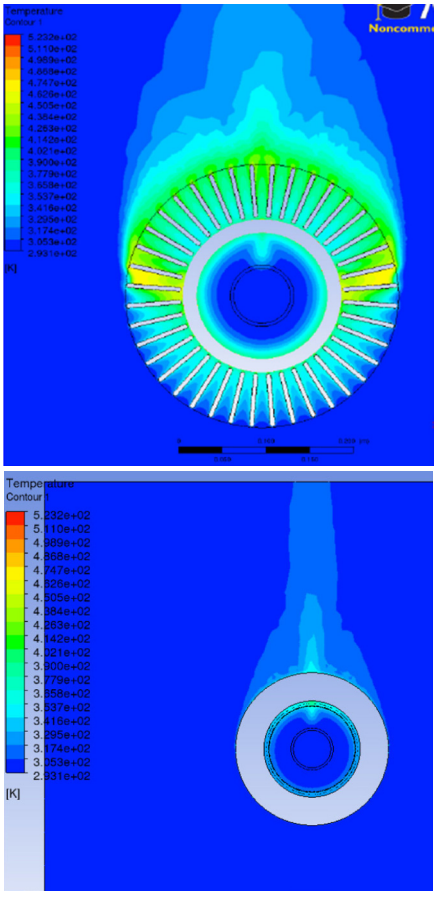

Fig. 13. *Air temperature contour in XZ plane for discs at 250 °C: a) ventilated disc, and b) solid disc*

4.4 Heat Transfer Coefficients

CFD analyses also enabled predictions of the local and average convective heat transfer coefficients over the disc surfaces, with Fig. 14 showing the ventilated and Fig. 15 solid disc. For both designs, it is clear that convective heat dissipation is more effective from the upper part of the disc, as would be expected. On the outboard side of the disc, the effect of the hub (top hat) can also be observed. The flow is blocked, and there is a reduction of the convective cooling in the middle of the disc, above the hub. However, this effect is not present on the inboard side of the disc friction faces. Maximum values of the heat transfer coefficient reach approx. 14.8 W/(m^{2}K) for the ventilated disc (Fig. 14) and 8.2 W/(m^{2}K) for the solid disc (Fig. 15), but these values of the convective heat transfer coefficients are limited to very small areas with no practical significance for disc cooling. For both designs, the highest values covering larger disc areas are around 5 W/(m^{2}K). CFD analyses enabled automatic calculations of average values for the convective heat dissipation coefficients, from the distributions shown in Figs. 14 and 15.

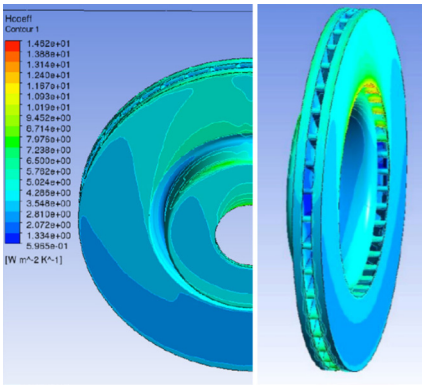

Fig. 14. *Predicted convective heat transfer coefficient distribution for ventilated disc*

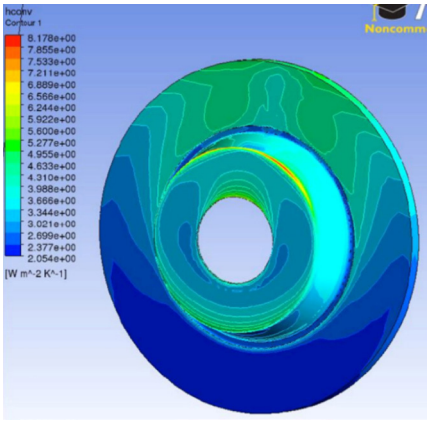

Fig. 15. *Predicted convective heat transfer coefficient distribution for solid disc*

Experimental investigations enabled only the extractions of average convective heat dissipation coefficients, from the average cooling curves (measured surface temperatures during disc cooling). The measurements of disc surface temperatures proved to be very repeatable and reliable. The procedure for calculating average convective heat transfer coefficients from cooling curves was explained earlier, which now enables for these values to be compared with CFD results. To cover the temperature range, CFD analyses had to be repeated for lower temperatures. The comparisons presented in Figs. 16 and 17 for ventilated and solid discs respectively, show quite interesting phenomena. For the ventilated disc (Fig. 16), the average convective heat transfer coefficients calculated from the measured cooling curves have higher values than CFD predictions. The gradient is also steeper, the cooling

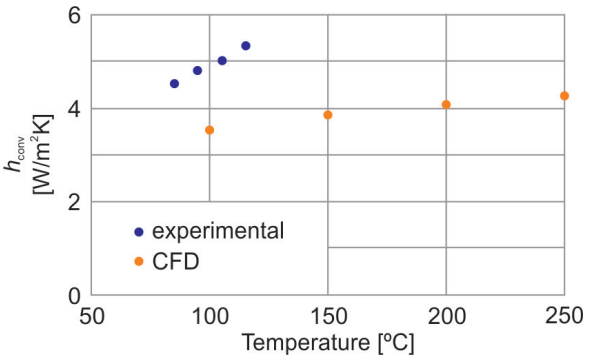

Fig. 16. *Ventilated disc: experimental and CFD average convective heat transfer coefficients*

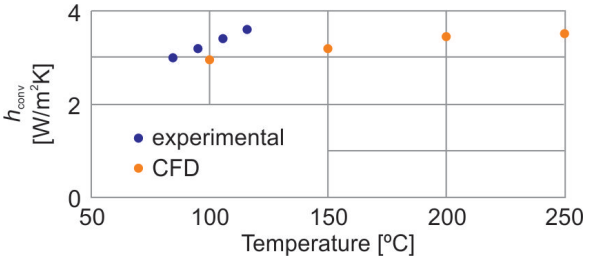

Fig. 17. *Solid disc: Experimental and CFD average convective heat transfer coefficients*

Table 4. *Measured average convective heat transfer coefficients for four designs studied*

Ref. Fig. 1	Disc design	h_{conv} [W/(m²K)]			
		Temperature range [°C]			
		120 to 110	110 to 100	100 to 90	90 to 80
a)	Ventilated with radial vanes	5.3	5.0	4.8	4.5
b)	Solid	3.6	3.4	3.2	3.0
c)	Ventilated with curved vanes	4.2	3.8	3.7	3.5
d)	Ventilated with curved vanes; cross drilled	4.4	4.1	3.7	3.5

is becoming more effective with increase in disc temperature. Unfortunately, with the heating system available it was not possible to heat the disc to higher experimental temperatures, but for disc at around 100 °C, the experimental values are about 40 % higher. For the solid disc (Fig. 17) experimental and CFD values of the convective heat transfer coefficient are much closer. Experimental values are again higher, but only by about 8 %. Though the experiments and CFD analyses were conducted for the same discs and nominal conditions, there were differences in "holding" the discs, as the discs were completely free standing in still air in CFD analyses (see Figs. 8a and 9a), whereas they were mounted to the hub flange and in proximity to the upright in experiments (see Fig. 3a).

5 DISCUSSION

The CFD analyses conducted under-predicted the values of the convective heat transfer coefficients. This was particularly the case for the ventilated disc, which has much more complex flow patterns. It was also established that the ventilated disc has higher values of the convective heat transfer coefficient, with this design also having much higher total wetted area. The combined effects will considerably increase convective dissipation, but the higher thermal capacity of this disc must be also considered. The ventilated disc has approximately 1.8 times higher wetted area and 2.9 times higher mass. Overall, the indications are that the two designs would cool at relatively similar rates in still air, from the same initial temperatures. This might change on the vehicle but generally is a good sign of maintaining relatively comparable temperatures of the front and rear brakes.

In addition to the VW Passat front and rear discs, it is interesting to present the measured values of the two Lotus Elise S2 disc designs. As no CFD analyses were conducted for these discs, only experimental values are presented in Table 4 in order to compare them with those of VW Passat discs.

The overall h_{conv} values (Table 4) indicate that the disc with radial vanes (VW Passat front) has the highest cooling rates and the solid disc (VW Passat rear) the lowest. Curved vanes help in increasing air flow and convective cooling of rotating discs but in stationary conditions curved vanes trap the air, preventing the buoyant flow upwards. It is also interesting to see (Table 4) that cross-drilling has practically no influence at lower temperatures up to about 100 °C, but at higher temperatures there is a measurable improvement of about 5 % at 120 °C. CFD analyses were not performed for curved vane discs, but some of the following photographs effectively illustrates air flow in stationary cooling.

Fig. 18 effectively illustrates the problem with stationary cooling of the curved vane discs. At the mid horizontal plane, at the end where the flow channels (and vanes) point upwards (Fig. 18a), the upwards flow is reasonable and seems very steady. The smoke is rising smoothly. However, at diametrically opposite end (Figs. 18b and c) where the vanes point downwards, there is obvious slowing down of the flow and chocking. The smoke is stagnant. The flow

through the bottom and top of the ventilation channels is not particularly good either.

Fig. 19 presents the cross-drilled disc, showing a similar flow problems to the standard, non-drilled disc (Fig. 18). At the mid horizontal plane, at the end where the flow channels (and vanes) point upwards (Fig. 19a), the flow is reasonable and seems very steady, similarly to the non-drilled disc (Fig. 18a). However, at the diametrically opposite end (Figs. 19b and c), there is obvious obstruction and chocking. To a certain degree the holes drilled through friction faces help the flow, and in Fig. 19c there is a clear view of the smoke rising upwards through the cross-drilled holes. It is reasonable to assume that in some areas the holes will also provide air entry, helping the overall cooling. The effects are expected to be more pronounced with

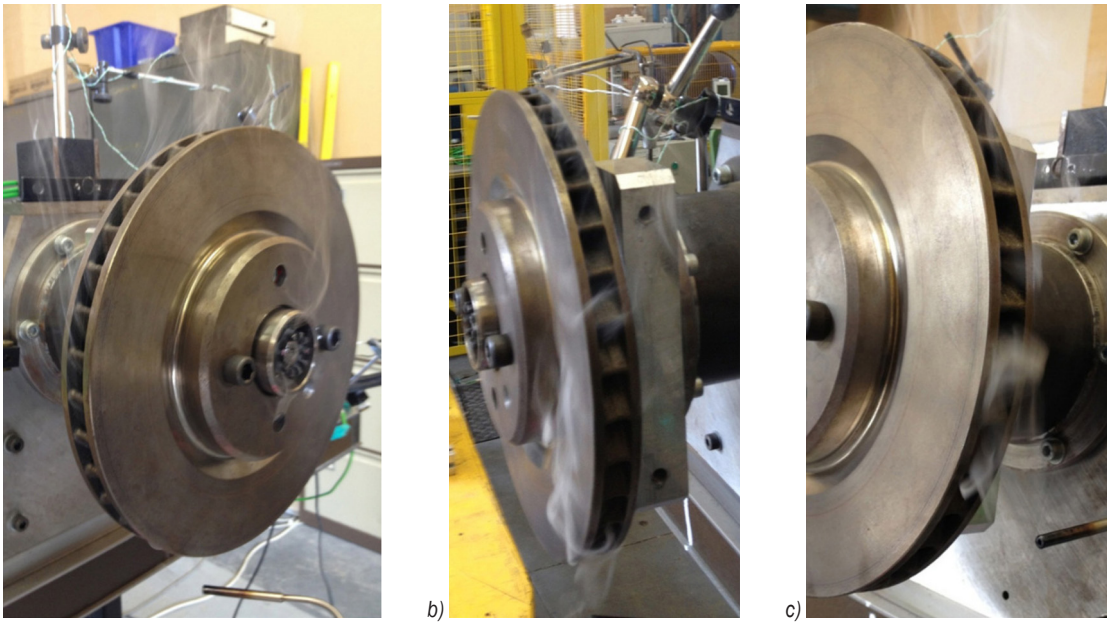

a) b) c)

Fig. 18. *Curved vane standard disc smoke tests: a) flow channels pointing upwards, b) and c) flow channels pointing downwards*

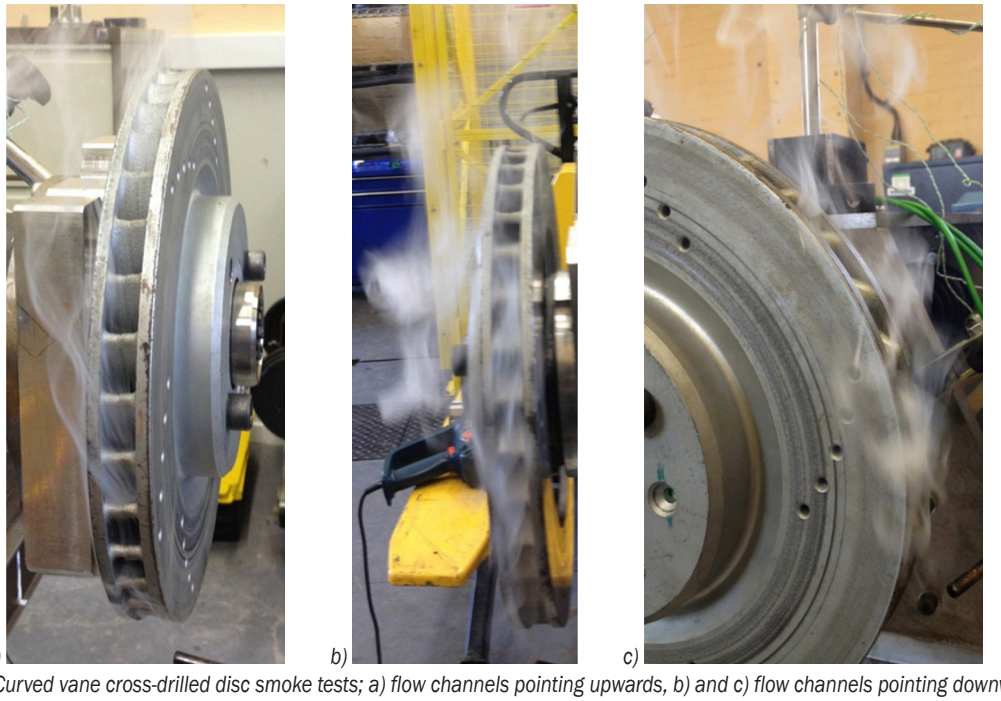

a) b) c)

Fig. 19. *Curved vane cross-drilled disc smoke tests; a) flow channels pointing upwards, b) and c) flow channels pointing downwards*

increased buoyancy, and the values in Table 4 prove that, with the cross-drilled disc showing superior cooling characteristics at higher temperatures (in comparison to the standard disc). The flow through the bottom and top of the ventilation channels can also be marginally helped with cross-drilling.

6 CONCLUSIONS

Experimental investigation of the heat dissipation from stationary discs was successful in ensuring repeatable and accurate measurement and prediction of the total, convective and radiative heat dissipation coefficients. The values compare favourably with CFD analyses, though the differences are somewhat pronounced for the ventilated discs. The speeds of the hot air rising above the disc are far too low and flow pattern narrow and relatively irregular, making the validation of air speeds and air temperatures practically impossible. However, the use of smoke generator (with neutral buoyancy smoke) and suitable probe was very useful in qualitatively validating the flow patterns.

Convective heat transfer coefficients increase with temperature but the values are very low, typically between 3 W/(m^{2}K) and 5 W/(m^{2}K) for the disc designs and temperature range analysed. As expected, out of the four designs studied, the disc with radial vanes has highest convective heat dissipation coefficient and the solid disc the lowest. The reduction is about 30 %, with the disc with curved vanes values being about 20 % lower than for the disc with radial vanes.

Low values of convective heat transfer coefficients indicate low dissipated energy (heat), in particular for the solid disc. Consequently, cooling times are very long and the contribution of the other two heat dissipation modes, conduction and radiation, higher. At high disc temperatures (>400 °C), radiative losses in stable conditions can be an order of the magnitude higher than convective.

When installed on the vehicle, with the addition of the calliper assembly, wheel, mudguard and dust shield, the cooling of brake discs is likely to be even further reduced. Future work is concentrated in addressing this challenge in two ways, by improving CFD modelling and equipping the thermal spin rig with induction heater to heat the disc much more rapidly and to much higher temperatures.

Cross drilling of the disc with curved vanes seems to only marginally improve static cooling, predominantly at higher temperatures.

7 ACKNOWLEDGEMENTS

Some of the presented results are part of a project financed by the Serbian Ministry of Education, Science and Technological Development (Project TR 35045 - "Scientific-Technological Support to Enhancing the Safety of Special Road and Rail Vehicles").

8 NOMENCLATURES

A_w	total disc wetted area, [m^2]
A_{rad}	radiative heat dissipation disc area, [m^2]
c_p	specific heat of disc material (grey iron), [J/(kgK)]
h_{tot}	total average heat transfer coefficient, [W/(m^{2}K)]
h_{conv}	average convective heat transfer coefficient, [W/(m^{2}K)]
h_{rad}	average radiative heat transfer coefficient, [W/(m^{2}K)]
m	disc mass, [kg]
T_d	average disc temperature during time period ($t_2 - t_1$), [K]
T_{d1}	disc temperature at the time t_1, [K]
T_{d2}	disc temperature at the time t_2, [K]
T_∞	ambient air temperature, [K]
t	time, [s]
ε	disc surface emissivity, [-]
σ	Stefan-Boltzmann constant ($5.67 \cdot 10^{-8}$), [W/(m^{2}K^2)]

9 REFERENCES

[1] UN Regulation No. 13-H (Revision 4) (2018). *Uniform Provisions Concerning the Approval of Passenger Cars with Regard to Braking*. United Nations, Geneve.

[2] Stevens, K. (2013). *An Investigation into Heat Dissipation from a Stationary Commercial Vehicle Brake Disc in Parked Conditions*, EngD Thesis, Cranfield University, Cranfield.

[3] Wagner, C. (1948). Heat transfer from a rotating disk to ambient air. *Journal of Applied Physics*, vol. 19, no. 9, p. 837-839, **DOI:10.1063/1.1698216**.

[4] Cobb, E.C., Saunders, O.A. (1956). Heat transfer from a rotating disk. *Proceedings of the Royal Society A: Mathematical, Physical and Engineering Sciences*, vol. 236, no. 1206, p. 343-351, **DOI:10.1098/rspa.1956.0141**.

[5] Richardson, P.D., Saunders, O.A. (1963). Studies of flow and heat transfer associated with a rotating disc. *Journal of Mechanical Engineering Science*, vol. 5, no. 4, p. 336-342, **DOI:10.1243/JMES_JOUR_1963_005_044_02**.

[6] Newcomb, T.P. (1959). Transient temperatures attained in disk brakes. *British Journal of Applied Physics*, vol. 10, no. 7, p. 339-340, **DOI: 10.1088/0508-3443/10/7/311**.

[7] Newcomb, T.P., Spurr, R.T. (1967). *Braking of Road Vehicles*. Chapman & Hall, London.

[8] Grkić, A., Mikluc, D., Muždeka, S., Arsenić, Ž., Duboka, Č. (2015). A Model for the estimation of brake interface temperature. *Strojniški vestnik - Journal of Mechanical Engineering,* vol. 61, no. 6, p. 392-398, **DOI:10.5545/sv-jme.2014.2364**.

[9] Noyes, R.N., Vickers, P.T. (1969). Prediction of surface temperatures in passenger car disc brakes. *SAE Technical Paper*, no. 690457, **DOI:10.4271/690457**.

[10] Morgan, S., Dennis, R.W. (1972). A theoretical prediction of disc brake temperatures and a comparison with experimental data, *SAE Technical Paper*, no. 720090, **DOI:10.4271/720090**.

[11] Limpert, R. (1975). Cooling analysis of disc brake rotors. *SAE Technical Paper*, no. 751014, **DOI:10.4271/751014**.

[12] Sisson, A.E. (1978). Thermal analysis of vented brake rotors. *SAE Technical Paper*, no. 780352, **DOI:10.4271/780352**.

[13] Daudi, A.R. (1999). 72 curved fins and air director idea increase airflow through brake rotors. *SAE Technical Paper*, no. 1999-01-0140, **DOI:10.4271/1999-01-0140**.

[14] Galindo-Lopez, C.H., Tirovic, M. (2008). Understanding and improving the convective cooling of brake discs with radial vanes. *Proceedings of the Institution of Mechanical Engineers, Part D: Journal of Automobile Engineering*, vol. 222, no. 7, p. 1211-1229, **DOI:10.1243/09544070JAUTO594**.

[15] Galindo-Lopez, C.H., Tirovic, M. (2013). Maximizing heat dissipation from ventilated wheel-hub-mounted railway brake discs. *Proceedings of the Institution of Mechanical Engineers, Part F: Journal of Rail and Rapid Transit*, vol. 227, no. 3, p. 269-285, **DOI:10.1177/0954409712462337**.

[16] Pevec, M., Potrc. I., Bombek, G., Vranesevic, D. (2012). Prediction of the cooling factors of a vehicle brake disc and its influence on the results of a thermal numerical simulation. *International Journal of Automotive Technology*, vol. 13, no. 5, p. 725-733, **DOI:10.1007/s12239-012-0071-y**.

[17] Son, J.K., Jung, Y.-S., Jeon, H.-H. (2018). Optimization analysis and design of brake cooling system. *EuroBrake 2018 Conference Proceedings*, paper EB2018-SVM-003.

[18] Stevens, K., Tirovic, M. (2018). Heat dissipation from a stationary brake disc, Part 1: Analytical modelling and experimental investigations. *Proceedings of the Institution of Mechanical Engineers, Part C: Journal of Mechanical Engineering Science*, vol. 232, no. 9, p. 1707-1733, **DOI:10.1177/0954406217707983**.

[19] Tirovic, M., Stevens, K. (2018). Heat dissipation from a stationary brake disc, Part 2: CFD modelling and experimental validations. *Proceedings of the Institution of Mechanical Engineers, Part C: Journal of Mechanical Engineering Science*, vol. 232, no. 10, p. 1898-1924, **DOI:10.1177/0954406217707984**.

[20] McAdams, W.H. (1954). *Heat Transfer*. McGraw-Hill, New York.

[21] Morgan, V.T. (1975). The overall convective heat transfer from smooth circular cylinders. *Advances in Heat Transfer*, vol. 11, p. 199-264, **DOI:10.1016/S0065-2717(08)70075-3**.

[22] Churchill, S.W., Chu, H.H.S. (1975). Correlating equations for laminar and turbulent free convection from a horizontal cylinder. *International Journal of Heat Mass Transfer*, vol. 18, no. 9, p. 1049-1053, **DOI:10.1016/0017-9310(75)90222-7**.

[23] Necati Özisik, M. (1989). *Heat Transfer: A Basic Approach*. McGraw-Hill, New York.

[24] Tirovic, M., Voller, G.P. (2005). Interface pressure distributions and thermal contact resistance of a bolted joint. *Proceedings of the Royal Society A: Mathematical, Physical and Engineering Sciences*, vol. 461, no. 2060, p. 2339-2354, **DOI:10.1098/rspa.2005.1452**.

[25] Teimourimanesh, S., Vernersson, T., Lundén, R. (2014). Modelling of temperatures during railway tread braking: Influence of contact conditions and rail cooling effect. *Proceedings of the Institution of Mechanical Engineers, Part F: Journal of Rail and Rapid Transit*, vol. 228, no. 1, p. 93-109, **DOI:10.1177/0954409712465696**.

[26] Eisengräber, R., Grochowicz, J., Schuster, M., Augsburg, K., Koch, L. (1999). Comparison of different methods for the determination of the friction temperature of disc brakes. *SAE Technical Paper*, no. 1999-01-0138, **DOI:10.4271/1999-01-0138**.

[27] Dufrenoy, P., Berte, E., Witz, J-F., Desplanques, Y. (2018). A new camera for quantitative measurements of temperature and emissivity during braking. *EuroBrake Conference Proceedings*, paper EB2018-VDT-033.

[28] Grieve, D.G., Barton, D.C., Crolla, D.A., Buckingham, J.T. (1998). Design of a lightweight automotive brake disc using finite element and Taguchi techniques. *Proceedings of the Institution of Mechanical Engineers, Part D: Journal of Automobile Engineering*, vol. 212, no. 4, p. 245-254, **DOI:10.1243/0954407981525939**.

[29] Tang, J., Bryant, D., Qi, H. (2018). Experimental investigation of the dynamic thermal deformation and judder of a ventilated disc brake. *EuroBrake Conference Proceedings*, paper EB2018-FBR-002.

[30] Topouris, S. (2017). *Design and Optimisation of a High Performance Lightweight Monoblock Cast Iron Brake Disc*, PhD Thesis. Cranfield University, Cranfield.

[31] Olphe-Galliard, M. (2011). *Study of Thermodynamics and Fluid Mechanics Involved in the Cooling of Brake Discs,* MSc Thesis. Cranfield University, Cranfield.

Strojniški vestnik - Journal of Mechanical Engineering 66(2020)1, 29-37

DOI:10.5545/sv-jme.2019.6297 Original Scientific Paper
Received for review: 2019-08-22
Received revised form: 2019-11-04
Accepted for publication: 2019-12-03

The Influence of Machining Parameters on the Surface Porosity of a Closed-Cell Aluminium Foam

Boštjan Razboršek* – Janez Gotlih – Timi Karner – Mirko Ficko
University of Maribor, Faculty of Mechanical Engineering, Slovenia

Aluminium foam elements foamed into moulds, have a porous core, surrounded by a thin layer of non-porous outer surface. This layer affects the homogeneity and mechanical properties of the element significantly. To produce functional elements, the foams can be machined to a desired end shape. Machining deforms the surface structure, which results in a reduction of strength properties. This article describes an experimental approach to determine the effects of machining parameters on the surface porosity of closed-cell aluminium foam samples. The samples were machined by incremental forming and friction rolling with precisely defined processing parameters (deformation depth, feed rate and spindle speed). High-resolution digital photos of the treated surfaces were taken and analysed using image segmentation with a multispectral threshold algorithm. The change of surface porosity was calculated for each sample, and the influence of the selected machining parameters was determined by the use of response surface methodology. The optimal machining parameters are presented.
Keywords: aluminium foam, machining, incremental forming, friction rolling, surface porosity, integral skin

Highlights
- *Machining experiments of closed-cell aluminium foam samples were performed.*
- *Incremental forming and friction stir rolling processes were used to reduce surface porosity.*
- *Image segmentation with a multispectral threshold algorithm was used to analyze the machined surface.*
- *Relationships between machininig parameters and change of surface porosity were explored.*

0 INTRODUCTION

In recent years, interest in metal foams has increased significantly. The main reasons are new concepts in the construction of ultra-light and energy absorbing products and structures, especially in transportation and construction [1]. With their unique combination of structural properties on the one hand and basic material properties on the other hand, metal foams have great potential for future use in many applications [2].

Foamed materials retain some of the physical properties of their basic material (e.g. non-combustibility, electrical conductivity), while some physical, thermal, electrical and acoustic properties change significantly [3]. Metal foams are materials with cellular structure, consisting of hard metal and air pores, which comprise 75 % to 95 % of the total volume. Based on their cellular structure (morphology), they form closed-cell elements or stay as open-cell elements. Because of their typical behaviour under compressive load, and a long, nearly horizontal curve of stress – strain (stress plateau), they represent an ideal material for the absorption of impact energy [4].

Research of aluminium foams is oriented in three directions: production, processing and application. Historic production processes controlled foam density rather than the growth of cellular structures, which led to unpredictable structural and mechanical properties of the end products. Improvements in production processes made commercial use of aluminium foams much wider [5]. Today, for design purposes numerical simulations of aluminium foams are applied [6]. With further development of additive or other cost effective manufacturing techniques, cellular materials show huge potential to become important light-weight structural materials of the future [7].

Aluminium, nickel, magnesium, lead, brass, titanium, copper, steel and even golden foams are known. Among them, aluminium foams are the most researched and commercially interesting, due to their extremely low density, high transformability, low thermal conductivity and competitive production prices [8]. To further improve their mechanical properties, metal matrix syntactic foams have been developed. In these porous materials the porosity is ensured by incorporating either ceramic or metallic hollow spheres [9]. The influence of different hollow spheres and structures at different conditions and temperatures on mechanical properties was investigated by Movahedi et al. [10], Zhao et al. [11], Taherisharg et al. [12] and Linul et al. [13].

To achieve the final shape of aluminium foam products, machining is an widely used option [1]. The problem is that after machining, the outer surface becomes extremely porous, with strongly deformed cells, which changes the mechanical properties of the product. Machining of aluminium foam with a porous outer surface was studied by Hunt [14]. It

*Corr. Author's Address: University of Maribor, Faculty of Mechanical Engineering, Smetanova ulica 17, 2000 Maribor, Slovenia, bostjan.razborsek@um.si

was found that, with a special process of infiltration of a particular medium into the outer surface pores and appropriate cutting parameters, it is possible to achieve no deformation, and that surface porosity remains the same as before the treatment. For the same reason Mane [15] used ice as an infiltrant. Michailidis et al. [16] investigated milling of porous aluminium. They found that an increase of the chip thickness have a beneficial effect in avoiding burr formation and pore closures through permanent deformations of the workpiece. De Jaeger et al. [17] compared four different methods of cutting open-cell aluminium foam, namely, cutting with a circular saw, band saw, cutting with wire, and electrical discharge machining (EDM). It was observed that cutting with a circular saw and band saw resulted in significant plastic deformation of the cut surface. Cutting with saw wire and via EDM does not result in any local compression. Surface roughness of the EDM process was considerably worse than the result obtained with saw wire. Ghose et al. [18] investigated the processing of closed-cell aluminium foam by EDM. They identified various control parameters of EDM for effective machining of aluminium foam and achieving optimal surface roughness. Matz et al. [19] examined the influence of flushing on the EDM process. They found that high feed rate can be achived due to the good flushing conditions and low density of the material. Michalidis et al. [20] optimized the EDM process to eliminate surface cell damages, affecting the mechanical response under quasi-static and high-velocity impact loads. Liu et al. [21] used laser cutting process for efficiently and directly cutting of three different types and two levels of pore density of metal foams into regular shapes. The results show that metal foam with a good surface quality can be obtained without damaging the pore structure.

In general, the surface quality of metal foams is not sufficient for many constructive applications. Due to the foaming process, the surface of foams contains many cracks and oxides and is rough and wavy. Fluids or gases can penetrate into the foam along the cracks and open pores. If exposed to a corrosive environment, corrosion will not only start on the surface, but also within the foam. Furthermore, the integral skin is very thin, and cannot be machined to a decent surface finish [22]. When machining elements produced by indirect foaming in moulds, a thin layer of integral skin is removed (non-porous surface). This results in collapsing of the surface compactness and interruption of stress forces. Such products have reduced strength and they wear easily if exposed to friction, due to their porous surface and low hardness. Several methods and procedures, like thermaly sprayed coatings [22], age-hardening heat treatment [23] and surface treatment by resin [24], have been developed in order to improve the quality of the outer porous surface, and, thus, wear and corrosion resistance and mechanical properties of the metal foams. Qiao et al. [25] investigated the effect of surface structure on mechanical properties of open-cell aluminium foam after machining. They found that the strenght of these materials may be enhanced trought surface structural gradients. On the other hand, some forming processes have been applied to control the surface porosity of porous metals. To improve mechanical properties, for example, the surface of lotus-type porous copper has been formed by wire-brushing [26]. In this process the cell walls near the surface were plastically deformed, and a non-porous layer was fabricated at the surface with fine grains. Friction stir incremental forming process was applied on the surface of porous aluminium foam to fabricate a non-porous layer. In the process, the cell walls near the surface were plastically deformed by a rotating tool with a high rotation rate. A non-porous layer thinner than 0.4 mm was fabricated at the surface without internal fracture of the aluminium foam [27]. Kwon at al. [28], modified the surface region of EDM aluminium foams by the friction-surface-modifying and rolling (FSMR) process. A new surface was obtained successfully through the FSMR process, which was considerably smoother and denser than that of the unprocessed aluminium foam.

According to the literature, the quality of the aluminum foam surface depends on its treatment processes. The aim of our research work is to determine the influence of different processing parameters on its surface porosity. Two different forming processes were used, namely, friction stir incremental forming (FSIF) and friction stir rolling (FSR). Both processes are well-known in the forming of sheet metal, where plastic deformation and surface transformation occur due to a rotating tool [29]. The result of such sheet metal forming is a fine-grained surface structure of the product. The structure is formed by dynamic recrystallization at high temperatures, caused by friction [27].

1 MATERIALS AND METHODS

In this research work, a closed-cell aluminium foam, with the commercial name Foamtech® (supplier AlCarbon) (Fig. 1) was used for FSIF and FSR studies. The technical properties of Foamtech® are given in Table 1.

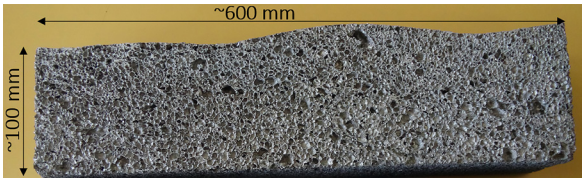

Fig. 1. *Closed-cell aluminium foam - Foamtech®*

Table 1. *Technical properties of Foamtech®*

Classification		Unit	Values
Basic properties	Material composition / alloy	/	Al. (≥97.5 %) / AA.1070
	Structure	/	Closed Cell
Physical properties	Compressive strength	MPa	1.0 ~ 1.8
	Flexural strength (by 4-point bending)	MPa	0.9 ~ 2.0
	Tensile strength	MPa	0.5 ~ 1.2
	Shear strength	MPa	0.7 ~ 1.5
	Density	g/cm³	0.15 ~ 0.3
	Heat conductivity	W/(mK)	Approx. 0.1
	Specific energy absorption (50 % deformation)	MJ/m³	0.61 (at density 0.2 g/cm³)
Dimension:	Thickness min. – max.	mm	9 ~ 100
	Standard panel size	mm	1200 (L) × 600 (W)

Samples were prepared with a band saw, using a low feed rate (~0.05 m/min) and coolant, resulting in minimum deformation of the sawn surface. The dimensions of the samples were (50 × 40 × 40) mm. A clamping device for the samples was designed and manufactured. The device was designed to allow rigid clamping of the samples without causing any structural deformation due to the clamping force. For forming, a carbide rod tool was used with 20 mm diameter and 1.5 mm rounding radius. The surface roughness of the tool was Ra1.6. The experimental work was carried out on a 4-axis, horizontal CNC milling machine Heller BEA1. Two processing methods were used. The first method was machining with the flat part of the tool (incremental forming, FSIF) (Fig. 2a). The second method was machining with the side part of the tool (friction rolling, FSR) (Fig. 2b).

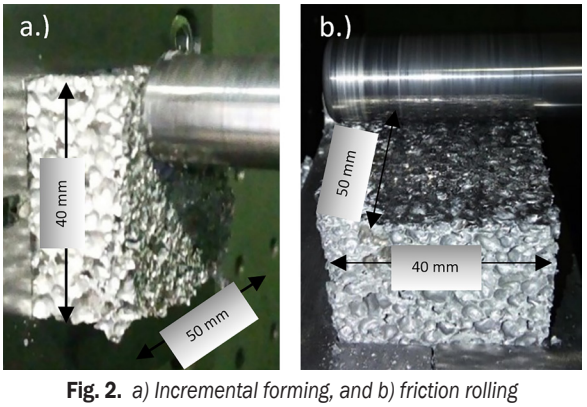

Fig. 2. *a) Incremental forming, and b) friction rolling*

2 EXPERIMENTAL PART

The experiment was designed as a full factorial 3^3 experiment with three factors and three levels for each factor (Table 2). Each factor was tested at each level in every possible combination. A total of 27 experiments of FSIF and 27 experiments of FSR were performed.

Table 2. *Factors and levels of experiment*

Factor	Level		
	0	1	2
Spindle speed [rmp]	16	2000	4000
Feed rate [mm/min]	250	500	1000
Total depth of forming [mm]	2	4	6

The entire surface of the samples was machined in three directional passes of the tool with a depth of 1 mm at each pass. The resulting surface porosity was used as the response of the experiment. The surface of the samples was painted yellow, to obtain a better contrast between the non-porous and the porous parts of the surface. Ten untreated samples were also painted. The mean value of their surface porosity represented the reference surface porosity value. High-resolution images of painted surfaces were taken with a digital camera. Removing a 2.5 mm wide edge reduced the size of the surface to be analysed to (45 × 35) mm, and eliminated the influence of deformation at the edges. Image segmentation with a multispectral threshold algorithm, slicing technique, and interactive selection of the threshold with aid of an image histogram, was used to transform the images to binary form. By thresholding each channel separately and combining the results using Boolean operations, we effectively found segments of the *n*-dimensional channel space (where *n* is the number of channels), where each image pixel was plotted using its channel values for coordinates. After thresholding and combining the red and the green channel for each pixel and excluding the pixels with a high blue value, the result was an image of yellow and black pixels. (Fig. 3a). Yellow pixels, which represent the non-porous surface, were transformed to white pixels, to create the final black and white binary image (Fig. 3b).

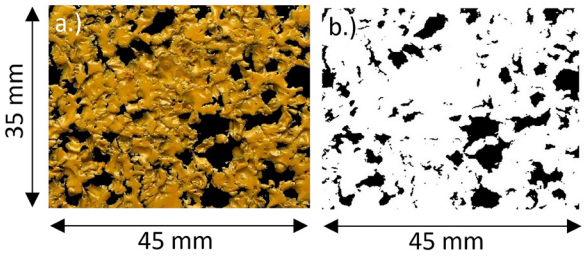

Fig. 3. *a) yellow/black image, and b) binary image*

The proportion of white pixels in relation to the total number of image pixels represented the proportion of the non-porous surface relative to the total area analysed.

The proportion of the non-porous surface S_{np} of a sample was evaluated (the surface coloured yellow). According to Eq. (1), the proportion of surface porosity S_p was calculated, whereby it was presumed that value 1 represents a completely non-porous surface.

$$S_{p,n} = 1 - S_{np,n}. \quad (1)$$

The mean reference value of the surface porosity $S_{p,mid}$ of the ten untreated reference samples was

Table 3. *Reference surface porosity*

Ref. sample	1	2	3	4	5	6	7	8	9	10
Proportion of non-porous surface S_{np} [%]	52.9	41.9	48.5	51.1	45.0	44.3	40.6	49.3	43.8	53.6
Proportion of porous surface S_p [%]	47.1	58.1	51.5	48.9	55.0	55.7	56.4	50.7	56.2	46.4
Mean value of porous surface $S_{p,mid}$ [%]	52.6									
Standard deviation [%]	4.22									
Deviation of the individual sample [%]	-5.5	+5.5	-1.1	-3.7	+2.4	+3.1	+3.8	-2.0	+3.6	-6.2

Table 4. *Design matrix and response data of FSIF and FSR experiments*

Sample	Factors			Response	
	Processing depth, a [mm]	Feed rate, f [mm/min]	Spindle speed, n [rpm]	Change of porosity [%] FSIF	Change of porosity [%] FSR
1	2	200	16	65.5	54.2
2	2	200	2000	53.2	63.4
3	2	200	4000	65.2	48.9
4	2	500	16	53.7	68.4
5	2	500	2000	59.9	67.2
6	2	500	4000	56.2	62.5
7	2	1000	16	42.8	47.3
8	2	1000	2000	59.8	54.9
9	2	1000	4000	65.9	63.9
10	4	200	16	83.5	77.2
11	4	200	2000	87.5	83.2
12	4	200	4000	8.0	86.4
13	4	500	16	66.6	71.0
14	4	500	2000	86.1	76.2
15	4	500	4000	87.2	60.3
16	4	1000	16	68.0	69.1
17	4	1000	2000	80.4	71.7
18	4	1000	4000	85.6	79.4
19	6	200	16	71.0	79.1
20	6	200	2000	90.5	83.6
22	6	200	4000	98.3	94.5
22	6	500	16	74.1	71.9
23	6	500	2000	92.4	69.8
24	6	500	4000	86.8	67.1
25	6	1000	16	74.9	78.5
26	6	1000	2000	73.6	85.8
27	6	1000	4000	82.1	82.5

calculated using Eq. (2), where $S_{p,r}$ is the surface porosity of the individual reference sample, and k is the number of reference samples.

$$S_{p,mid} = \frac{1}{k}\sum_{i=1}^{k} S_{p,r,k,i}. \quad (2)$$

Change of surface porosity for each sample was calculated according to Eq. (3).

$$\Delta S_p\,[\%] = \left(1 - \frac{S_p}{S_{p,mid}}\right)\cdot 100\,\%. \quad (3)$$

3 RESULTS AND DISCUSSION

Table 3 shows the individual surface porosity values of 10 untreated reference samples, determined according to Eq. (1), and the average reference porosity value. The standard deviation of the surface porosity and the maximum deviation of individual samples was 4.22 % and 6.2 %, respectively.

Table 4 shows the percentage change of surface porosity of the samples treated by FSIF and FSR. Results show that machining with different process parameters caused different surface porosity of the samples.

Relationships between spindle speed, feed rate, processing depth (explanatory variables) and change of surface porosity (response variable) were explored by response surface methodology. The influence of processing parameters on surface porosity is shown in the graphs below.

Fig. 4 shows the dependence of the surface porosity reduction on spindle speed and feed rate, at 2, 4 and 6 mm depth for FSIF and FSR. At the 2 mm processing depth (Fig. 4a), the change in surface porosity is relatively small (from 47 % to 68 %) and distributed randomly, which is due to the size of the aluminium foam cells. At the processing depth 4 mm (Fig. 4b) the influence of the processing parameters on the decreasing of surface porosity is already noticeable. By increasing the spindle speed and decreasing the feed rate, up to 87 % reduction of

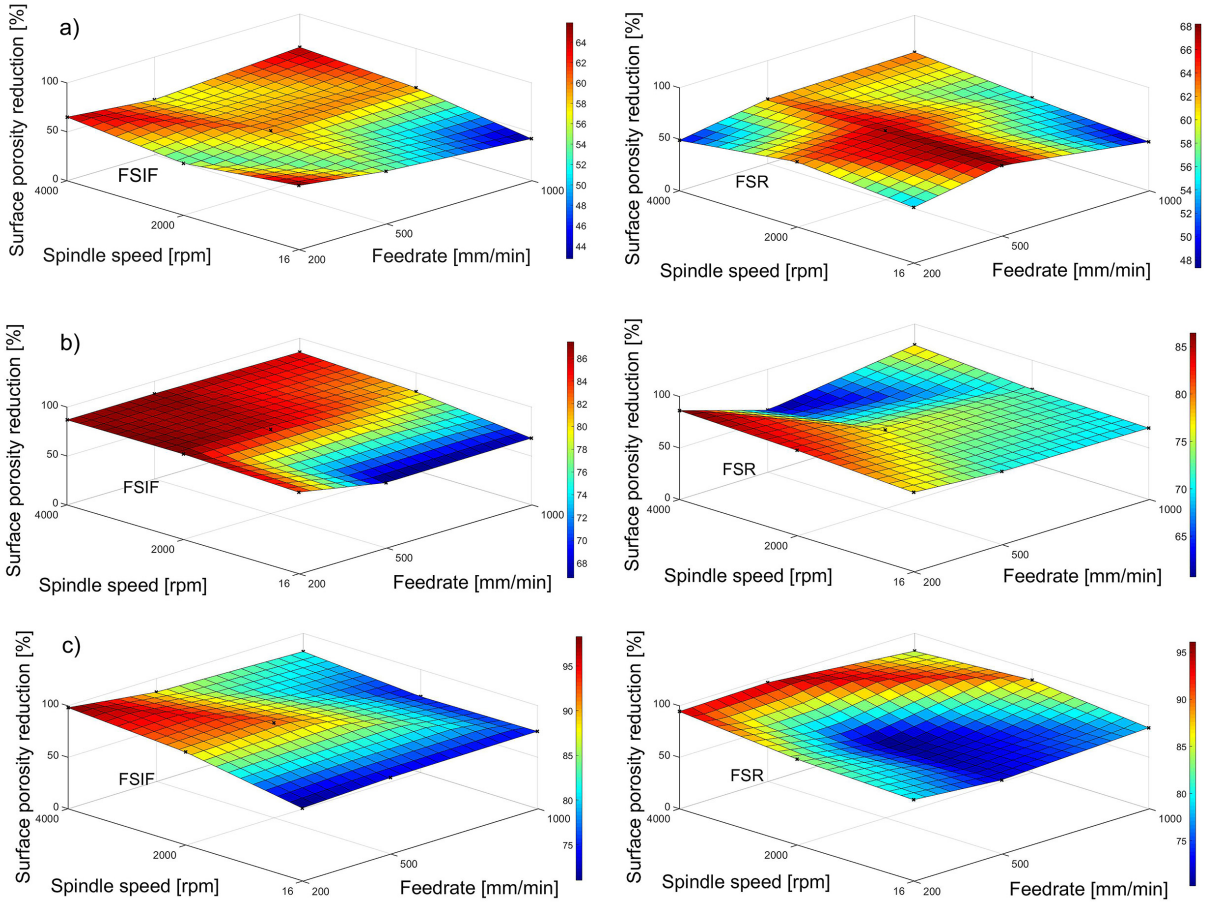

Fig. 4. *Surface porosity reduction at: a) 2 mm, b) 4 mm, and c) 6 mm depth of FSIF and FSR*

surface porosity was achieved with FSIF and FSR. Surface porosity reduction is even more pronounced at 6 mm processing depth (Fig. 4c). 98 % reduction of surface porosity was achieved with incremental forming at the maximum spindle speed and the minimum feed rate. Even with FSR, the maximum surface porosity reduction was achieved with increasing of spindle speed, while the feed rate shows no significante effect.

On the Fig. 5, surface porosity reduction at the different feed rate is shown. It is clear from the graphs that, at constant feed rate of 200 mm/min (Fig. 5a) surface porosity decreases (achieved over 90 %) with increasing spindle speed and depth of processing. This trend of surface porosity reduction applies to FSIF and FSR. At the constant feed rate 500 mm/min (Fig. 5b) and increasing processing depth and spindle speed, higher values of surface porosity reduction were achieved with FSIF than with FSR. Maximum achived reduction of surface porosity for FSIF was 87 % while surface porosity reduction with FSR did not exceed 76 %. The trend of surface porosity reduction at 1000 mm/min (Fig. 5c) is similar to the trend where a feed rate of 500 mm/min was used. The maximum reduction of porosity at feedrate 1000 mm/min did not exceed 85 % for both processes.

Fig. 6 shows the dependence of the surface porosity reduction on processing depth and the feed rate, at a different spindle speed. It can be seen from the graphs that at spindle speed 16 rpm (Fig. 6a) surface porosity reduction was achieved only with increasing of processing depth, while the feed rate did not have significant influence on the final results. The maximum reduction of surface porosity at 16 rpm was 83 % for FSIF and 78 % for FSR. At constant spindle speed of 2000 rpm (Fig. 6b) can be seen that processing depth has a greater influence on the reduction of surface porosity than feed rate. Reduction of surface porosity due to an increase of the processing depth from 2 mm to 6 mm is about 20 %, and for decreasing the feed rate from 1000 mm/min to 200 mm/min, only 10 %. The largest reduction of surface porosity was 90 % for FSIF and

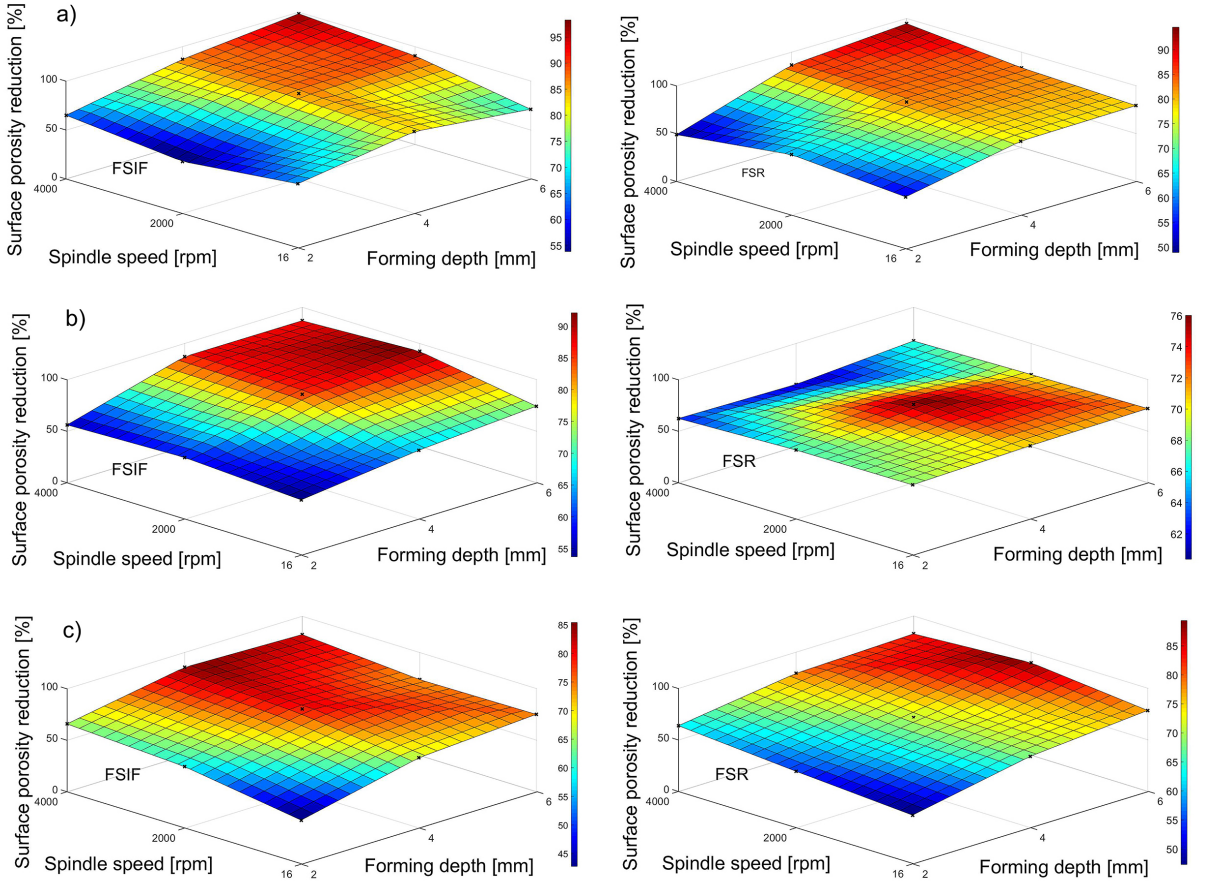

Fig. 5. *Surface porosity reduction at feed rate: a) 200 mm/min, b) 500 mm/min, and c) 1000 mm/min of FSIF and FSR*

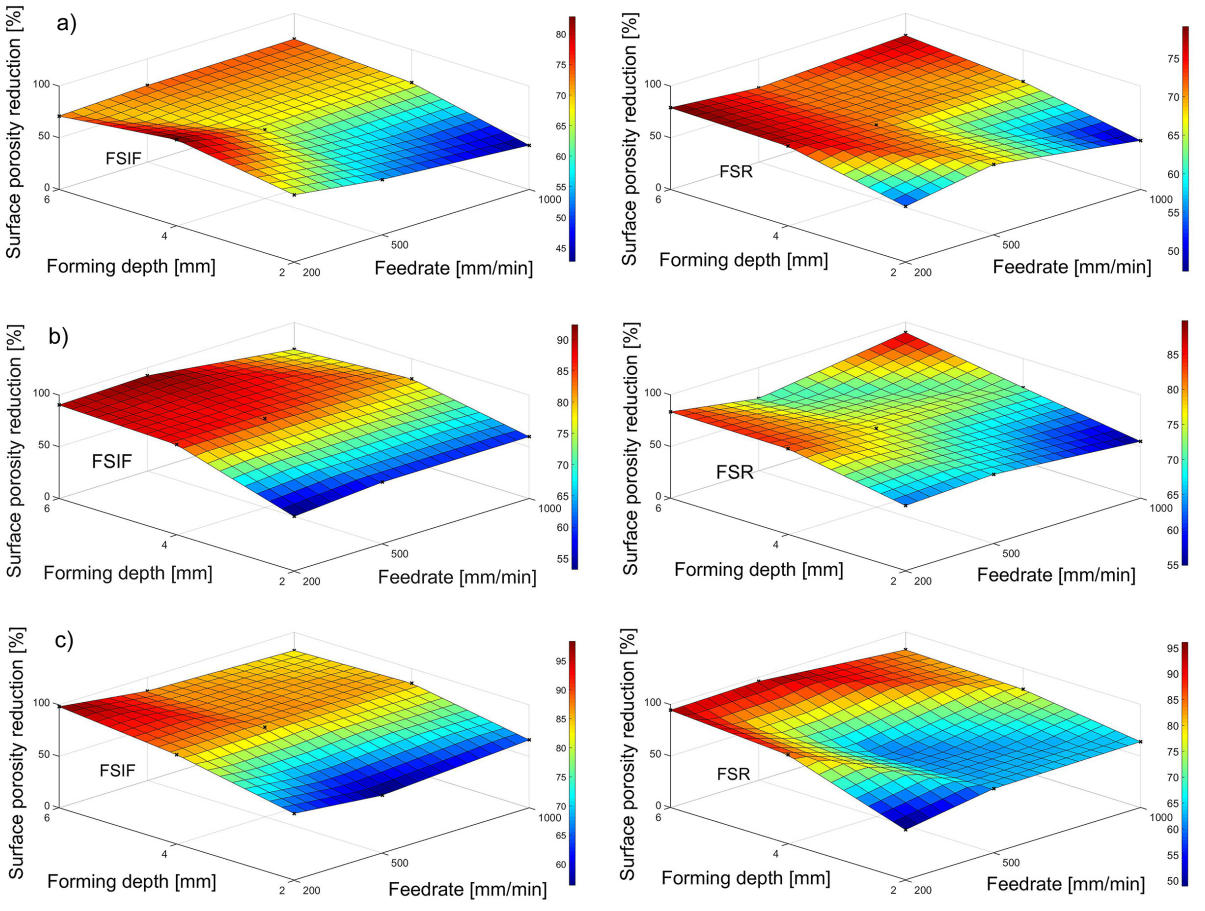

Fig. 6. *Surface porosity reduction at a) 16 rpm, b) 2000 rpm, and b) 4000 rpm (c) spindle speed of FSIF and FSR*

83 % for FSR. The trend of decreasing surface porosity at constant spindle speed 4000 rpm (Fig. 6c) was approximately the same as for processing at 2000 rpm, but the maximum achived reduction of surface porosity for FSIF was 98 % and 94 % for FSR.

From the test results obtained, we can conclude that changing the process parameters of incremental forming and friction rolling influences surface porosity significantly. Over 90 % reduction of surface porosity was achieved for both processes. The highest reduction of surface porosity, 98.3 %, was achieved by FSIF at spindle speed 4000 rpm, feed rate 200 mm/min and processing depth 6 mm. With FSR, the highest value achieved was 96.1 % at spindle speed 4000 rpm, feed rate 500 mm/min and processing depth 6 mm. Processing depth, followed by spindle speed, have the greatest impact on porosity reduction. Reducing of feed rate has a lower impact on surface porosity and also increases processing time, which is not reasonable. To reduce porosity, it is reasonable to increase spindle speed, since the increase of the processing depth is limited by the shape of the work piece and processing time. It is also evident from the results that an average 5 % to 10 % higher decrease of surface porosity was achieved in incremental forming rather than frictional rolling. Altough the FSIF and FSR processes of aluminium foam has been studied previously **[21]** and **[28]**, so far this is the first report where the influence of different machining parameters on surface porosity reduction was investigated. When compared to published papers, in this study different strategies of machining were used and surface porosity analysis were carried out, using image segmentation with multispectral threshold algorithm.

4 CONCLUSIONS

We found that forming aluminium foams with incremental forming or friction rolling enables the reduction of surface porosity of aluminium foam elements previously processed with cutting (sawing, milling, turning). A non-porous outer surface

(integral skin) that improves mechanical properties (e.g. strength) of the finished elements was formed using different machining parameters. By forming the material, the stress field (force lines) becomes smooth and continuous, which reduces the notch effect and raises compressive strength. Despite the high deformation depth, deformation of the processed elements remains in the local area, which is due to the cellular structure and good transformability of aluminium foams. Compact aluminium foam elements can be produced with combinations of cutting operations (milling, turning) and forming operations (incremental forming, friction rolling). Both operations can be carried out on the same machine, which lowers costs substantially. In comparison with small batch production of elements foamed into moulds, the incremental forming or friction rolling methods are cheaper, because there are no costs of mould making, and semi-finished products can be used, such as blocks, bars and sheets.

5 ACKNOWLEDGEMENTS

This work was supported financially by the Slovenian Research Agency (ARRS), Programme P2-0157.

6 REFERENCES

[1] Ashby, M.F., Evans, A., Fleck, N.A., Gibson, L.J., Hutchinson, J.W., Wadley, H.N.G. (2000). *Metal Foams: A Design Guide*. Butterworth-Heinemann, Oxford, **DOI:10.1016/S0261-3069(01)00049-8**.

[2] Banhart, J. (2001). Manufacture, characterisation and application of cellular metals and metal foams. *Progress in Materials Science*, vol. 46, no. 6, p. 559-632, **DOI:10.1016/S0079-6425(00)00002-5**.

[3] Lefebvre, L.P., Banhart, J., Dunand, D.C. (2008). Porous metals and metallic foams: current status and recent developments. *Advanced Engineering Materials*, vol. 10, no. 9, p. 775-787, **DOI:10.1002/adem.200800241**.

[4] Duarte, I., Vesenjak, M., Krstulović-Opara, L. (2014). Variation of quasi-static and dynamic compressive properties in a single aluminium foam block. *Materials Science and Engineering: A*, vol. 616, p. 171-182, **DOI:10.1016/j.msea.2014.08.002**.

[5] Duarte, I., Oliveir, M. (2012). Aluminium alloy foams: Production and properties. *Powder Metallurgy*, Kondoh, K. (ed.). Intechopen, London, p. 47-72, **DOI:10.5772/34433**.

[6] Mankovits, T., Varga, T. A., Manó, S., Kocsis, I. (2018). Compressive response determination of closed-cell aluminium foam and linear-elastic finite element simulation of MCT-based directly reconstructed geometrical models. *Strojniški vestnik - Journal of Mechanical Engineering*, vol. 64, no. 2, p. 105-113, **DOI:10.5545/sv-jme.2017.5048**.

[7] Nečemer, B., Vesenjak, M., Glodež, S. (2019). Fatigue of cellular structures – a review. *Strojniški vestnik – Journal of Mechanical Engineering*, vol. 65, no. 9, p. 525-536, **DOI:10.5545/sv-jme.2019.6070**.

[8] Banhart, J. (2000). *Manufacturing Routes for Very Low Specific*. *Jom* 52 (December), p. 22–27.

[9] Orbulov, I.N. (2012). Compressive properties of aluminium matrix syntactic foams. *Materials Science and Engineering: A*, vol. 555, p. 52-56, **DOI:10.1016/j.msea.2012.06.032**.

[10] Movahedi, N., Taherishargh, M., Belova, I.V., Murch, G.E., Fiedler, T. (2018). Mechanical and microstructural characterization of an AZ91-activated carbon syntactic foam. Materials, vol. 12, vol. 1, p- 3, **DOI:10.3390/ma12010003**.

[11] Zhao, Y.Y., Tao, X.F. (2009). Behaviour of metal matrix syntactic foams in compression. *Materials Science & Technology Conference and Exhibition, Proceedings*, p. 1785-1795.

[12] Taherishargh, M., Linul, E., Broxtermann, S., Fiedler, T. (2018). The mechanical properties of expanded perlite-aluminium syntactic foam at elevated temperatures. *Journal of Alloys and Compounds*, vol. 737, p. 590-596, **DOI:10.1016/j.jallcom.2017.12.083**.

[13] Linul, E., Marsavina, L., Kováčik, J. (2017). Collapse mechanisms of metal foam matrix composites under static and dynamic loading conditions. *Materials Science and Engineering: A*, vol. 690, p. 214-224, **DOI:10.1016/j.msea.2017.03.009**.

[14] Hunt, C.V. (2009). *A Method to Reduce Smearing in the Milling of Metal Foams*. PhD thesis, Iowa State University, Ames, **DOI:10.31274/etd-180810-591**.

[15] Mane, V.V. (2016). *An Effective Method to Reduce Smearing in Machining of Metallic Foams Using Ice as an Infiltrant*. PhD thesis, Iowa State University, Ames, **DOI:10.31274/etd-180810-4657**.

[16] Michailidis, N., Kombogiannis, S., Charalampous, P., Maliaris, G., Stergioudi, F. (2017). Computational-experimental investigation of milling porous aluminium. *CIRP Annals*, vol. 66, no 1, p. 121-124, **DOI:10.1016/j.cirp.2017.04.022**.

[17] De Jaeger, P., T'Joen, C., Huisseune, H., Ameel, B., De Schampheleire, S., De Paepe, M. (2012). Assessing the influence of four bonding methods on the thermal contact resistance of open-cell aluminum foam. *International Journal of Heat and Mass Transfer*, vol. 55, no. 21-22, p. 6200-6210, **DOI:10.1016/j.ijheatmasstransfer.2012.06.043**.

[18] Ghose, J., Sharma, V., Kumar, N., Krishnamurthy, A., Kumar, S., Botak, Z. (2011). Taguchi-fuzzy based mapping of EDM-machinability of aluminium foam. T*ehnički Vjesnik - Techinical Gazette*, vol. 18, no. 4, p. 595-600.

[19] Matz, A.M., Kammerer, D., Jost, N., Oßwald, K. (2016). Machining of metal foams with varying mesostructure using wire EDM. *Procedia CIRP*, vol. 42, p. 263-267, **DOI:10.1016/j.procir.2016.02.283**.

[20] Michailidis, N., Klink, A., Smyrnaios, E., Olivier, M., Baklatzoglou, N., Welschof, L., Stergioudi, F. (2018). Surface structure, pore characteristics and mechanical response of aluminum foam processed by Wire-EDM and milling. *MATEC Web of Conferences*, vol. 188, art. no. 03012, **DOI:10.1051/matecconf/201818803012**.

[21] Liu, Y., Zhou, W., Chu, X., Liu, S., Hui, K.S. (2018). Feasibility investigation of direct laser cutting process of metal foam with high pore density. *The International Journal of*

Advanced Manufacturing Technology, vol. 96, p. 2803-2814, **DOI:10.1007/s00170-018-1796-1**.

[22] Maurer, M., Zhao, L., Lugscheider, E. (2002). Surface refinement of metal foams. Advanced Engineering Materials, vol. 4, no. 10, p. 791-797, **DOI:10.1002/1527-2648(20021014)4:10<791::AID-ADEM791>3.0.CO;2-Q**.

[23] Banhart, J., Baumeister, J. (1998). Deformation characteristics of metal foams. *Journal of Materials Science*, vol. 33, p. 1431-1440, **DOI:10.1023/A:1004383222228**.

[24] Kitazono, K., Suzuki, R., Inui, Y. (2009). Novel strengthening method of closed-cell aluminum foams through surface treatment by resin. *Journal of Materials Processing Technology*, vol. 209, no. 7, p. 3550-3554, **DOI:10.1016/j.jmatprotec.2008.08.013**.

[25] Qiao, H., Murthy, T.G., Saldana, C. (2019). Structure and deformation of gradient metal foams produced by machining. *ASME Journal of Manufacturing Science and Engineering*, vol. 141, no. 7, art. 171009, **DOI:10.1115/1.4043768**.

[26] Lobos, J., Suzuki, S., Nakajima, H., Ji, Y.S., Fujii, H., Terada, D., Tsuji, N. (2009). Structural change and improvement of the mechanical properties of a lotus-type porous copper by wire-brushing. *Journal of Physics: Conference Series*, vol. 165, no. 1, art. 012070, **DOI:10.1088/1742-6596/165/1/012070**.

[27] Matsumoto, R., Tsuruoka, H., Otsu, M., Utsunomiya, H. (2015). Fabrication of skin layer on aluminum foam surface by friction stir incremental forming and its mechanical properties. *Journal of Materials Processing Technology*, vol. 218, p. 23-31, **DOI:10.1016/j.jmatprotec.2014.11.030**.

[28] Kwon, Y.-J., Shigematsu, I., Saito, N. (2009). Development of new production technology for metallic foam core sandwich panel using friction phenomena. *Materials Transactions*, vol. 50, no. 4, p. 879-884, **DOI:10.2320/matertrans.MER2008321**.

[29] Petek, A., Podgornik, B., Kuzman, K., Čekada, M., Waldhauser, W., Vižintin, J. (2008). The analysis of complex tribological system of single point incremental sheet metal forming - SPIF. *Strojniski vestnik - Journal of Mechanical Engineering*, vol. 54, no. 4, p. 266-273.

Strojniški vestnik - Journal of Mechanical Engineering 66(2020)1, 38-50
DOI:10.5545/sv-jme.2019.6228
Original Scientific Paper
Received for review: 2019-07-03
Received revised form: 2019-09-02
Accepted for publication: 2019-09-24

Design and Performance Analysis of Airbag-Soft-Manipulator According to Characteristic Parameters

Peng Liu – Yonghong Liu* – Ke Wang – Xiaoxuan Wei – Chao Xin – Xinlei Wu
China University of Petroleum (East China), College of Mechanical and Electronic Engineering, China

Manipulators are increasingly used in mechanical manufacturing due to the needs of industrial automation. The shortcomings of traditional manipulators, such as those in relation to their flexibility, interactivity, and safety, lead to certain limitations in their application for variable shapes and fragile objects. Given the above shortcomings of traditional manipulators, this research analysed a friction-enhanced multi-airbag soft manipulator and its performance. Analysis results of characteristic parameters show that the structure of the airbag soft manipulator is optimized, and the structural design and manufacture of the soft manipulator are completed. Deformation of the manipulator base material is described by the Neo-Hooke strain energy function, and the strain energy function coefficient is derived by obtaining the characteristic parameters of the material through tensile experiments. Finite element analysis of the manipulator is performed according to the determined strain energy function. The influence of the characteristic parameters on the mechanical bending of the manipulator is studied. Theoretical analysis proves the validity of the finite element analysis. The structural parameters of the manipulator are finally determined according to the simulation analysis results. The control system is designed according to the driving method and working mode of the soft manipulator to perform the soft manipulator grasp experiment. The manipulator can lift a weight of 300 g, thereby indicating that the soft manipulator designed in this paper has a good application effect and prospects.

Keywords: soft manipulator, characteristic parameters, optimized, grasp experiment

Highlights

- *The structure of the airbag soft manipulator is optimized, and the structural design and manufacture of the soft manipulator are completed.*
- *Deformation of the manipulator base material is described by the Neo-Hooke strain energy function, and the strain energy function coefficient is derived by obtaining the characteristic parameters of the material through tensile experiments.*
- *Finite element analysis of manipulator is performed according to the determined strain energy function. The influence of the characteristic parameters on the mechanical bending of the manipulator is studied.*
- *According to the driving method and working mode of the soft robot, the control system is designed to perform the soft robot gripping experiment.*

0 INTRODUCTION

Robotic manipulators have reshaped industrial processes. The traditional application of rigid manipulators in people's production and life has liberated them from heavy labour, which has greatly promoted the automation and mechanization of industrial production [1]. The traditional manipulator is mainly made of metal material, which is realized by a complicated control system for handling, etc., such as the control of a six-degree-of-freedom robotic manipulator [2]. In the process of grasping irregularly shaped and fragile objects, it is difficult to perform such work using the traditional rigid manipulator because the rigidity of the operating object is much lower than the rigidity of the manipulator. With the development of three-dimensional (3D) printing technology and materials science, some scientists began to use soft materials to design and manufacture manipulators, which caused widespread interest [3] and [4]. Soft manipulators are inspired by bionics. By utilizing and exerting the mechanical intelligence of the soft material, the material is physically close to the organism itself, and the soft manipulators that are as flexible as the object to be manipulated and more adaptable are obtained [5].

To obtain mechanical properties and flexibility of the soft manipulators, many scholars have conducted a lot of research and achieved remarkable results. Marchese and Rus [6] present an extremely soft robotic manipulator morphology that is composed entirely of low durometer elastomer, powered by pressurized air, and designed to be both modular and durable. Blanes et al. [7] developed a pneumatic robot gripper capable of sorting eggplants according to their firmness, one of the fingers adapts to and copies the shapes of eggplants when the jamming of its internal granular material changes from soft to hard. Ranzani et al. [8] present the concept design of a modular soft manipulator for minimally invasive surgery, and combined flexible fluidic actuators to obtain multidirectional bending and elongation with

*Corr. Author's Address: China University of Petroleum, Changjiang West Road 66, Qingdao, China, liuyhupc@163.com

a variable stiffness mechanism based on granular jamming. Erkaya [9] investigated the effects of joint clearance in a robotic system, which improved the accuracy of robotic manipulators for many industrial and medical applications. Galloway et al. [10] present the development of an underwater gripper that utilizes soft robotics technology to delicately manipulate and sample fragile species on the deep reef and demonstrated design principles for soft robot end effectors, bench-top characterization of their grasping performance and conclude by describing in situ testing at mesophotic depths.

In addition to structural improvements, many researchers have broken through the boundaries of tradition and studied the materials and manufacturing methods of software manipulators. Diller and Sitti [11] used a magnetic polymer to manufacture soft manipulators, controlling the soft manipulators by magnetic properties, so that the manipulators can achieve 3D space motion. Ge et al. [12] present a new 4D printing approach that can create high resolution (up to a few microns), multi-material shape memory polymer (SMP) architectures, and can create soft manipulators with pre-programmed functions. Yuk et al. [13] showed that the hydraulic actuations of hydrogels with designed structures and properties could give soft actuators and robots that are high-speed, high-force, and optically and sonically camouflaged in water. Ongaro et al. [14] used a thermosensitive gel to design soft untethered grippers that can be used in an unstructured environment. Hughes and Iida [15] studied the control of a general-purpose soft manipulator based on tactile sensing.

There are also many researchers who have studied the driving methods of soft manipulators. It is hoped that the improvement of the driving method will make the soft manipulators move more quickly and more powerfully. Jun et al. [16] proposed a weighted gradient projection method to resolve inverse kinematics problems of redundant manipulators with multiple performance criteria. Brown et al. [17] developed a "coffee bag"-shaped blocking-based software manipulator that achieves the capture of objects of different shapes by blocking between different parts. Deaconescu and Deaconescu [18] aimed to present and discuss an innovative, constructive solution for a gripper system that can be attached to an industrial robot for assembly operations. Behl et al. [19] designed a soft manipulator using a shape memory polymer that can be bi-directionally bent. The soft manipulator grasps the object by bending the shape memory polymer. Kim et al. [20] developed a soft manipulator that can capture a variety of irregular objects using shape memory alloys. Lau [21] report a three-dimensional design of dielectric elastomer fingers with higher flexural stiffness and close to 90° voltage-controllable bending for object gripping and pinching. Alam et al. [22] addressed the design and implementation of robust nonlinear control approaches to obtain the desired trajectory tracking of a flexible joint manipulator driven with a direct-current geared motor. Li [23] proposed a parallel-chain nonholonomic manipulator with a chainable kinetics model. The manipulator could move to the target configuration within the specified time was proved by two simulation experiments.

Yang et al. [24] achieved both the controllability of compliance and the acquisition of position feedback in soft robotic fingers in the novel design of a 3D-printed multi-smart material substrate. Fei et al. [25] present the design and test of a novel fabric-based versatile and stiffness-tuneable soft gripper integrating soft pneumatic fingers and a wrist. The morphology is designed into a compact tuning fork shape with two bidirectional sheet-shaped soft fingers and a biaxial bidirectional (universal) cylinder-shaped soft wrist.

In this paper, an enhanced soft manipulator is designed according to the characteristics of soft materials, and the satisfying gripping effect is verified by experiments.

1 SOFT MANIPULATOR PERFORMANCE ANALYSIS

1.1 Soft Manipulator Driving Method

The function of the soft manipulator is directly affected by its structure. Such a structure includes the configuration of the soft mechanical finger and the layout of the finger. During the design process, the fingers of the soft manipulator are simulated to determine the optimal parameters. The soft manipulator is made of a generally nonlinearly deformed soft material. Thus, the conventional driving method for use on a rigid material is no longer applicable. The driving method of the software manipulator currently includes a direct transmission of the driving force from the power source to the body or driving with a directly deformable driver. The four types of commonly used driving methods include pneumatic driving [26] and [27], cable driving [28], shape memory alloy [29], and electroactive polymer driving [30]. The software manipulator studied in this research requires a substantial output force to facilitate the grasping of the object, and the soft robot must respond and be grasped quickly. Therefore, pneumatic driving is used to drive the entire soft manipulator,

and a soft manipulator is designed according to the characteristics of the pneumatic drive.

1.2 Neo-Hooke Characteristic Model

A soft manipulator is distinguished from a traditional manipulator as the former uses a flexible material. Therefore, when simulating and analysing the soft manipulator, the material parameters must first be determined. In this work, silica gel is used as the base material of the manipulator. The strain energy function is often utilized to express the characteristics of the super-elastic materials of silicone rubber. Common characteristic models include the Neo-Hooke [31], Mooney-Rivlin [32], and Ogden models [33]. The most extensive model is the Neo-Hooke model, which is based on two assumptions: material incompressibility and material isotropy. Given the above assumptions, the strain energy function is described as a function of the three main invariants I_1, I_2 and I_3 of the Green strain tensor E, as shown in Eq. (1).

$$E = E\left(I_1, I_2, I_3\right), \tag{1}$$

where I_1, I_2 and I_3 can be calculated according to Eq. (2).

$$\begin{cases} I_1 = \lambda_1^2 + \lambda_2^2 + \lambda_3^2 \\ I_2 = \lambda_1^2 \cdot \lambda_2^2 + \lambda_1^2 \cdot \lambda_3^2 + \lambda_2^2 \cdot \lambda_3^2 \\ I_3 = \lambda_1^2 \cdot \lambda_2^2 \cdot \lambda_3^2 \\ \lambda_i = 1 + \varepsilon_i \end{cases}. \tag{2}$$

Given that the material is incompressible, Eq. (3) can be obtained as:

$$I_3 = \lambda_1^2 \cdot \lambda_2^2 \cdot \lambda_3^2 = 1. \tag{3}$$

Bringing Eq. (3) into Eq. (2) gives:

$$\begin{cases} I_1 = \lambda_1^2 + \lambda_2^2 + \lambda_3^2 \\ I_2 = \dfrac{1}{\lambda_1^2} + \dfrac{1}{\lambda_2^2} + \dfrac{1}{\lambda_3^2} \end{cases}. \tag{4}$$

Therefore, the strain energy function W is expressed as a function of I_1 and I_2. When the material is not deformed, $\lambda_1 = \lambda_2 = \lambda_3 = 1$. In this condition, the strain energy function can be approximated as an exponential form, as shown in Eq. (5):

$$W = \sum_{i+j+k=1}^{\infty} C_{ij} \left(I_1 - 3\right)^i \left(I_2 - 3\right)^j \left(I_3 - 1\right)^k. \tag{5}$$

Given that $I_3 = 1$, the simplification of Eq. (5) is:

$$W = \sum_{i+j=1}^{\infty} C_{ij} \left(I_1 - 3\right)^i \left(I_2 - 3\right)^j. \tag{6}$$

As the limits of I_1 and I_2 are both 3, a large exponential in Eq. (6) reduces the value of W; thus, W can be ignored in subsequent calculations. Taking the first term of Eq. (6) yields a strain energy expression in the form of a silica gel Neo-Hooke model:

$$W = C_{10}\left(I_1 - 3\right). \tag{7}$$

Accurately describing the strain energy function of silica gel requires adding the corresponding isosceles function part to Eq. (7), and the strain energy function is obtained as follows:

$$W = C_{10}\left(I_1 - 3\right) + D_1\left(J - 1\right)^2. \tag{8}$$

Simulation describes the strain of silica gel according to the strain energy function, and the coefficients therein have the following relationship:

$$C_{10} = \frac{G}{2}, \tag{9}$$

$$D_1 = \frac{2}{\kappa}. \tag{10}$$

Assuming that the volume of the silica material is incompressible, its bulk modulus is infinite, $D_1 = 0$, and the shear modulus of the material can be experimentally determined.

1.3 Soft Material Characteristic Parameters

To determine the material characteristic parameters, the tensile test is carried out, and the specimen is prepared according to the corresponding standard-GB/T 528-2009. Fig. 1a illustrates the shape of the specimen, and Fig. 1b demonstrates the tensile test specimen. The dimensions of the specimen are as follows: A (100 mm), B (25 mm), C (20 mm), D (5 mm), E (11 mm), and F (25 mm).

A tensile test is performed. As shown in Fig. 2, the model of the tensile testing machine is the JJ-TEST-UTM. The specimen is symmetrically clamped on the upper and lower holders of the tensile testing machine, thereby enabling an even distribution of the tensile force on the cross-section. Fig. 2a presents the testing machine. Fig. 2b illustrates the specimen clamping diagram. During the test, the tensile machine stretched the specimen at a speed of 5 mm/min until it broke. The maximum stress is generated at the fracture of the specimen. The displacement of the chuck is automatically recorded by a tensile machine during the stretching process. The change in the length ΔL and the load generated by the stretching F is obtained; then, the strain ε and the stress σ are calculated as in Eqs. (11) and (12), respectively.

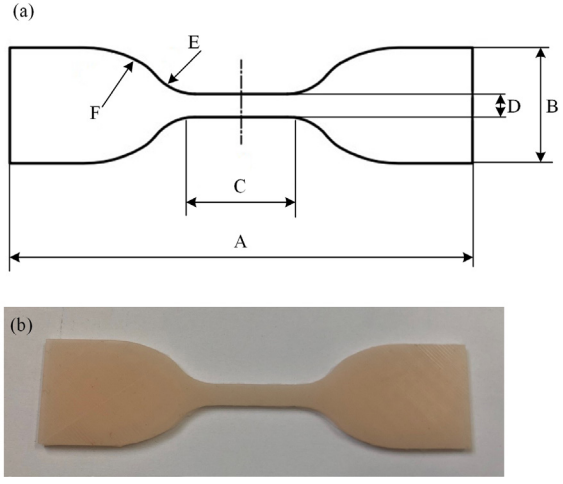

Fig. 1. *Specimen; a) diagram of dumbbell specimen; and b) tensile test specimen*

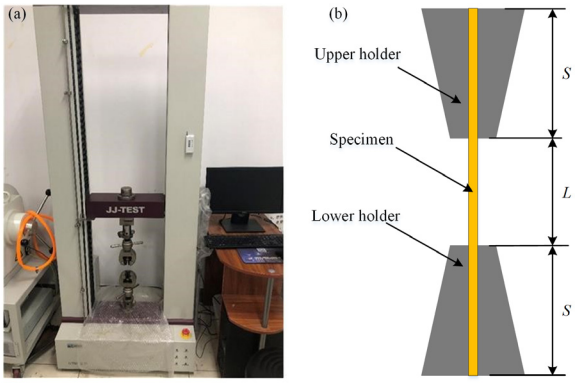

Fig. 2. *Universal testing machine and its holder; a) tensile testing machine; and b) clamping diagram*

$$\varepsilon = \frac{\Delta L}{L}, \tag{11}$$

$$\sigma = \frac{F}{S_b}, \tag{12}$$

where L represents the length of the specimen before deformation, and S_b is the cross-sectional area at the fracture. The stress-strain curve of the specimen is obtained. As shown in Fig. 3, Young's modulus of the silica material can be obtained:

$$E = \frac{\sigma}{\varepsilon}. \tag{13}$$

Eq. (13) indicates that Young's modulus is the slope of the relationship curve in Fig. 3. Young's modulus of the silica gel material is obtained, namely, $E=0.67441$ MPa. The following relationship exists between the shear modulus and Young's modulus:

$$G = \frac{E}{2(1+\mu)}, \tag{14}$$

where G is the shear modulus of the material in MPa; and μ is 0.48.

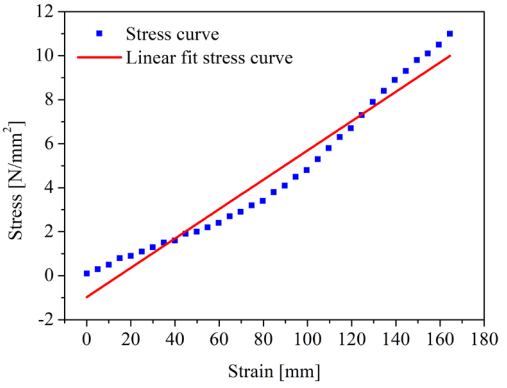

Fig. 3. *Stress-strain curve of silica gel*

The shear modulus of the material can be calculated through Eq. (14). According to Eq. (9), the parameters $C_{10}=0.11392$ and $D_1=0$ of the material under the Neo-Hooke strain energy function can be obtained.

2 SIMULATION ANALYSIS OF THE SOFT MANIPULATOR

2.1 Finite Element Simulation Analysis

After selecting gas power as the driving method of the soft manipulator, we design a multi-airbag soft manipulator. Fig. 4 shows the structure.

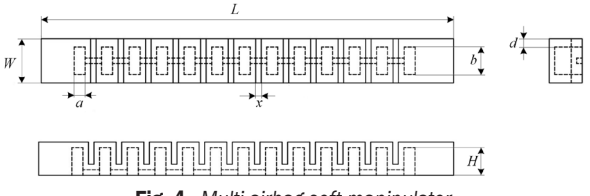

Fig. 4. *Multi-airbag soft manipulator*

Multi-airbag soft manipulator is affected by body characteristic parameters when subjected to force deformation, including: width W, length L, airbag width a, airbag length b, airbag depth H, airbag number n, airbag wall thickness d and airbag spacing x. The simulation analysis initialization parameters are set to 150 mm (length), 16 mm (width), 12 mm (height), and the number of airbags (13). The size of a single airbag is 10 mm (length), 3 mm (width), and 10 mm (height). The spacing of the airbag is 10 mm, with 2 mm in width for the back gap, 8 mm in height, and

the spacing runs through the front and back. During the analysis, the pressure applied inside the soft manipulator is 0.07 MPa.

(1) Effect of width W

Under the condition that the airbag length is constant b, a relationship exists between the width of the soft manipulator and the thickness of the sidewall, as shown in Eq. (15):

$$W = b + 2d. \tag{15}$$

According to Eq. (15), the case wherein the airbag length is determined, the influence of the thickness of the soft body sidewall, and the soft body manipulator width on the mechanical bending of the soft body are essentially similar. When studying the influence of the width using SIMULIA Abaqus [34], the width of the soft manipulator is set to 14 mm, 16 mm, 18 mm, 20 mm, and 22 mm, and Fig. 5 shows the angles of the mechanical arm of different widths.

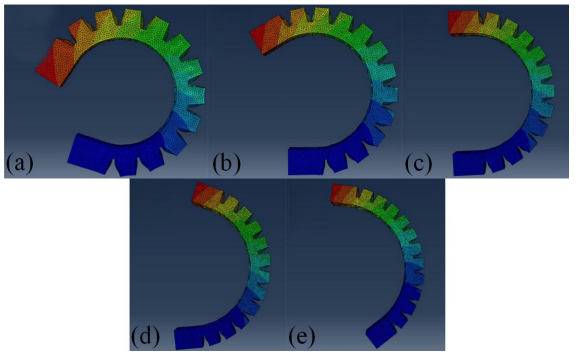

Fig. 5. *Bending angle of soft manipulator with different width; a) 14 mm; b) 16 mm; c) 18 mm; d) 20 mm; and e) 22 mm*

The relationship between the width and the bending angle is ascertained, as shown in Table 1.

Table 1. *Bending angle of soft manipulator under different widths*

W [mm]	14	16	18	20	22
Bending angle [°]	258.5	210.3	175.8	155.3	138.5

As the width of the soft manipulator increases, the angle of the mechanical manipulator's force bending becomes smaller slowly, thereby indicating that the increase in the width of the soft manipulator negatively affects the bending of the manipulator.

(2) Effect of the airbag length b

When studying the effect of the width of the soft airbag on the bending of the soft manipulator, the airbag lengths are set to 8 mm, 10 mm, 12 mm, 14 mm, and 16 mm. Fig. 6 illustrates the angles of the mechanical manipulators under different airbag lengths.

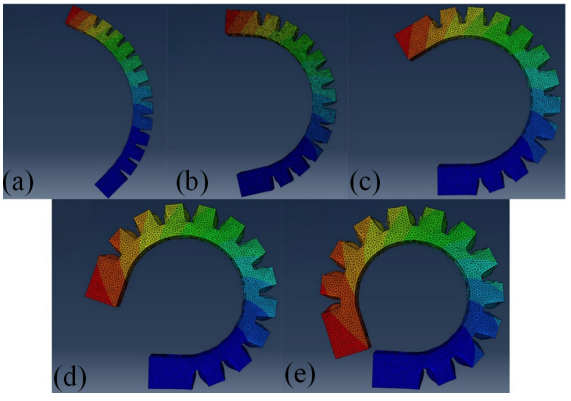

Fig. 6. *Bending angle of soft manipulator under different airbag length; a) 8 mm; b) 10 mm; c) 12 mm; d) 14 mm; and e) 16 mm*

The relationship between airbag length and the bending angle is ascertained and shown in Table 2.

Table 2. *Bending angle of soft manipulator under different widths*

b [mm]	6	8	10	12	14
Bending angle [°]	110.1	165.3	210.3	252.5	289.6

As the length of the airbag increases, the force bending angle of the soft manipulator increases. Thus, airbag length positively influences the mechanical bending of the soft manipulator.

(3) Effect of airbag width a

When the airbag width a is applied to the soft manipulator, the airbag widths are set to 2 mm, 2.5 mm, 3 mm, 3.5 mm, and 4 mm; moreover, Fig. 7 illustrates the bending under different airbag width conditions.

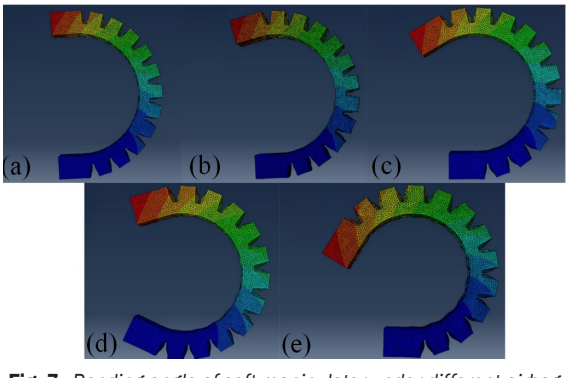

Fig. 7. *Bending angle of soft manipulator under different airbag widths; a) 2 mm; b) 2.5 mm; c) 3 mm; d) 3.5 mm; and e) 4 mm*

Table 3 shows the relationship between the airbag width and the bending angle.

Table 3. Bending angle of soft manipulator under different airbag widths

a [mm]	2	2.5	3	3.5	4
Bending angle [°]	178.2	193.4	210.3	222.4	238.4

As the width of the airbag increases, the angle at which the soft body is forced to bend increases, thereby indicating that the increase in the width of the airbag positively affects the bending of the soft manipulator.

(4) Effect of the number of airbags n

When the lengths of both ends of the soft manipulator are unchanged, the relationship between the length of the soft manipulator and the number of the airbags n is expressed by Eq. (16), and the airbag pitch at this time is 10 mm.

$$L = d_1 + d_2 + xn. \tag{16}$$

When the length of both ends and the distance between the airbags are constant, the length of the soft manipulator is essentially the same as the number of airbags. The number of airbags in the simulation are 11 to 15. Fig. 8 shows the bending angle of the soft manipulator.

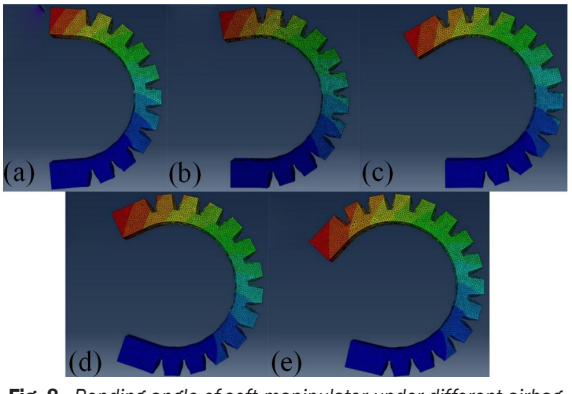

Fig. 8. *Bending angle of soft manipulator under different airbag numbers; a) 11; b) 12; c) 13; d) 14; and e) 15*

Table 4 shows the relationship between the number of airbags and the bending angle.

Table 4. *Bending angle of soft manipulator under different airbag widths*

n	11	12	13	14	15
Bending angle [°]	171.4	190.0	210.3	223.6	240.1

As the number of airbags increases, the angle at which the soft manipulator is forced to bend increases. Thus, an increase in the number of airbags positively affects the mechanical bending of the soft manipulator.

(5) Effect of airbag depth H

The depths of the soft body manipulator airbag are 6 mm to 10 mm in the study of the effect of the airbag depth H. Fig. 9 illustrates the bending under different airbag depth conditions.

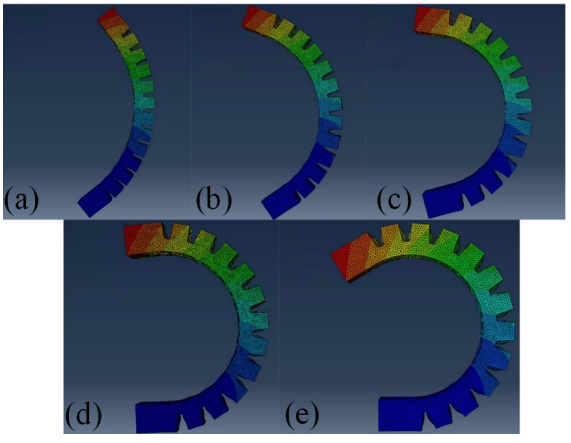

Fig. 9. *Bending angle of soft manipulator under different airbag depths; a) 6 mm; b) 7 mm; c) 8 mm; d) 9 mm; and e) 10 mm*

Table 5 demonstrates the relationship between the airbag width and the bending angle.

Table 5. *Bending angle of soft manipulator under different airbag depths*

H [mm]	6	7	8	9	10
Bending angle [°]	87.7	124.8	161.9	184.9	210.3

As the depth of the airbag increases, the angle at which the soft body manipulator bends is also increased. Thus, an increase in the depth of the airbag positively affects the mechanical bending of the soft body manipulator.

(6) Effect of airbag spacing x

According to Eq. (16), the influence of the airbag spacing and of the length of the soft manipulator on the mechanical bending of the soft body are essentially the same when the length of the two ends of the soft manipulator and the number of airbags are constant. The spacing of airbags are 9 mm, 10 mm, 11 mm, 12 mm, and 13 mm in the study of the influence of the spacing of the airbag on the soft manipulator, and Fig. 10 presents the bending diagram of the soft manipulator.

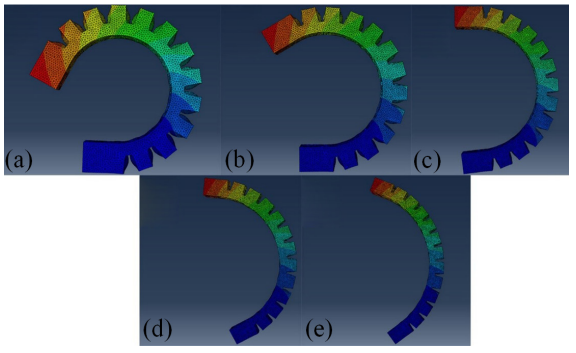

Fig. 10. *Bending angle of soft manipulator under different airbag spacings; a) 9 mm; b) 10 mm; c) 11 mm; d) 12 mm; and e) 13 mm*

Table 6 establishes the relationship between the airbag spacing and the bending angle.

Table 6. *Bending angle of soft manipulator under different airbag spacings*

x [mm]	9	10	11	12	13
Bending angle [°]	245.1	210.3	175.7	146.7	120.6

As the distance between the airbags increases, the angle at which the soft manipulator is forced to bend is reduced. Thus, an increase in the depth of the airbag negatively affects the mechanical bending of the soft manipulator.

2.2 Theoretical Analysis of Software Manipulator Bending

Fig. 11 illustrates the force received inside the soft manipulator. For convenience, the force analysis inside the soft manipulator is simplified because the soft manipulator is only bent inside the illustrated interface, and the force acting on the sidewall of the soft manipulator can be ignored. Fig. 12 presents a simplified schematic of the force analysis.

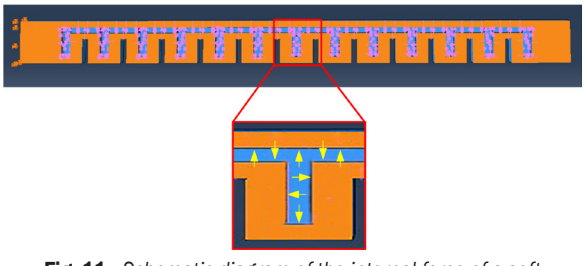

Fig. 11. *Schematic diagram of the internal force of a soft manipulator*

The inner wall of the soft manipulator is divided into a curved inner side and a curved outer side (Fig. 13). The inner sidewall of the curved inner side has no airbag and is a flat surface. Conversely, the inner wall

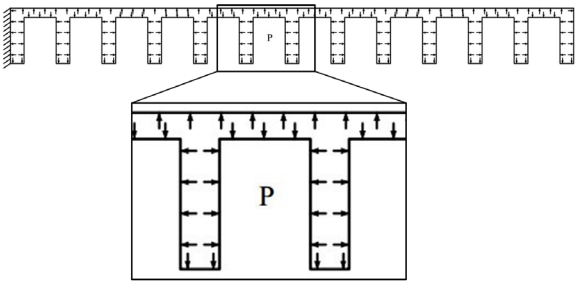

Fig. 12. *Schematic diagram of force analysis for soft manipulator*

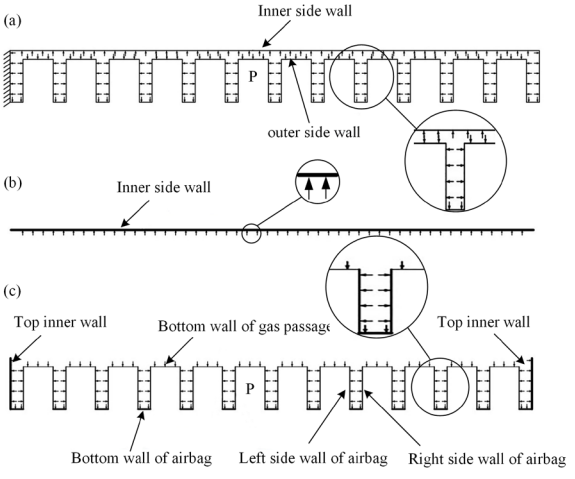

Fig. 13. *Inner and outer sides of bending soft manipulators and their stress analysis; a) inner and outer sides; b) stress analysis of inner side; c) stress analysis of outer side*

of the outer side of the curved side is provided with an airbag. Thus, the inner wall of the force-receiving inner wall includes the inner wall of the end portion and the left side of the airbag, apart from the portion which is balanced with the inner wall of the curved inner and right side walls of the airbag. After being subjected to the same amount of gas pressure, the inner wall of the curved outer side is subjected to a pressure substantially stronger than that applied to the inner side of the curved portion, such that the force deformation generated outside the curved portion is larger than the bending deformation generated by the inner side of the curved portion, and the soft body mechanical force is bent by the force. The deformation predisposes the airbag on the outside of the curved body to expand. After being subjected to the internal pressure of the soft manipulator, the length of the curved outer side perpendicular to the fixed end is greater than the length of the curved inner side perpendicular to the fixed end owing to the curved inner side and the curved outer side. The ends of the soft manipulator are connected to each other; thus, the

soft manipulator can only eliminate the difference in length between the inner and outer sides of the bend by bending.

The soft manipulator forms a concentric fan-shaped area after bending, and the curved inner and outer sides are respectively two arcs of a fan shape. The difference between the lengths of the curved inner and outer sides can be expressed by the difference in the arc length of the fan shape (Fig. 14). The difference in the curvature of the inner and outer sides of the curved body of the soft body is obtained, as shown in Eq. (17).

$$L_r = \pi\alpha(r_a + h) - \pi\alpha r_a = \pi\alpha h. \tag{17}$$

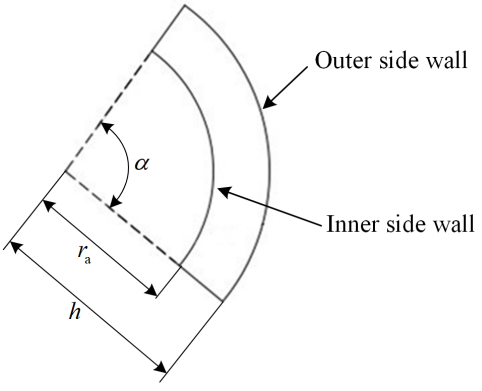

Fig. 14. *A sector formed by the bending of a manipulator*

The difference between its inner and outer sides is related to the height and bending curvature of the soft manipulator. After the structure of the soft manipulator is determined, the difference between the inner and outer lengths is ascertained only in relation to the arc corresponding to the curved arc. The greater the arc of the inner and outer sides, the greater the difference in arc length. The difference between the inner and outer lengths is related to the pressure difference between the inner and outer sides of the soft manipulator. The force inside the soft manipulator can be obtained by Eq. (18):

$$F_s = P_s \cdot S_s. \tag{18}$$

When the gas pressure applied to the inner wall of the soft manipulator is constant, the pressure applied to the inside of the soft manipulator changes with the change in the force-receiving area. The pressure difference can be obtained by Eq. (19):

$$F_\Delta = P_s \cdot S_\Delta, \tag{19}$$

where F_Δ denotes the force difference between the inner and outer inner walls of the bend; S_Δ is the difference between the inner and outer inner wall areas of the soft manipulator.

The difference between the inner and outer inner wall areas of the soft manipulator can be calculated by Eq. (20):

$$S_\Delta = S_L + S_R + S_{LT} + S_{RT}. \tag{20}$$

Fig. 15 shows the force-receiving surfaces on the left and right sides of the airbag and the left and right ends of the robot.

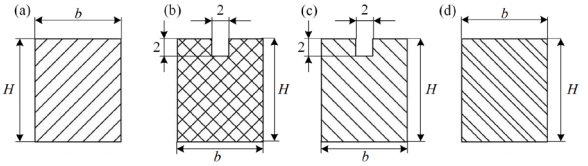

Fig. 15. *Four cross-sections causing pressure difference*

The four pressure differences can be calculated by Eq. (21):

$$\begin{cases} S_L = S_R = b \cdot H - 4 \\ S_{LT} = S_{RT} = b \cdot H \end{cases}, \tag{21}$$

where b and H respectively represent the length and depth of the soft manipulator airbag.

Eq. (21) shows that the length and depth of the airbag are strongly affected by the force of the soft manipulator. This observation can also be proven via simulation results. Under the influence of two factors, the change angles of the bending angle of the soft manipulator are 122.6° and 179.5°, respectively. The large length influence is caused by the change amount in length, which is relatively large. The remaining influencing factors include the width W and the airbag spacing x. The thickness of the silica gel is affected by the impedance change when the deformation is changed. The bending forces of the soft body are −120.0° and −124.5°, respectively. The increase in the width of the soft manipulator and the distance between the airbags cause an increase in the bending resistance, and such modification reduces the bending angle. The width of the airbag and the number of airbags also have a certain influence on the bending of the soft manipulator. The changes in the angle are 60.2° and 68.7°. The change in these two parameters alters the length of the soft manipulator, the width of the airbag, and the number of airbags. The increase in those parameters will increase the length of the soft manipulator; moreover, the force and deformation resistance will not change, thereby changing the bending angle of the soft manipulator. The theoretical analysis proves that the influence of the above

parameters on the bending of the soft manipulator is consistent with the simulation analysis results, which can be used as a reference for design.

2.3 Characteristic Parameters of the Soft Manipulator

(1) The template size used in this research is 20 mm × 20 mm. For the nanofibre film and the soft manipulator to fit well, the width of the soft manipulator is set as 20 mm.
(2) The sidewalls of the soft manipulator must have a certain thickness. When the wall thickness is under 1 mm, the simulation results do not converge. To ensure the safety of the soft manipulator, the wall thickness must be greater than or equal to 2 mm.
(3) According to the width and wall thickness requirements, the length of the soft manipulator airbag is 14 mm, and the sidewall is 3 mm, dimensions which meet the design requirements.
(4) The width of the airbag has less influence on the soft manipulator. To facilitate the draft, the width of the airbag is set to 3 mm.
(5) The depth of the airbag is 10 mm, where the airflow passage is distributed at 2 mm on the top.
(6) After the depth of the airbag is determined, the height is also ascertained to be 14 mm, and the thickness of the upper and lower end faces is 2 mm.
(7) To facilitate the drafting operation, the depth and width of the groove are set to 8 mm and 3 mm, respectively; moreover, the thickness of the sidewall of the airbag sandwiched between the groove and the airbag is 3 mm. These dimensions satisfy the requirements of safety design.
(8) The chosen number of airbags is eight.
(9) According to Eqs. (4) and (7) and the wall thickness of the airbag, the distance between the airbags is determined to be 12 mm.
(10) The total length of the soft manipulator is set to 115 mm.
(11) The two ends of the soft manipulator are symmetrical. According to Eqs. (4), (8), (9), and (10), the length of both ends is 14 mm.

3 GRASP EXPERIMENT OF AIRBAG SOFT MANIPULATOR

Since the soft manipulator contains airbags inside, it cannot be integrally cast during the manufacturing process, so the moulds are separately designed and cast, and the manufactured samples are combined. The manipulator is divided into upper and lower parts, and the moulds are printed by 3D printing technology, as shown in Fig. 16.

The airbag soft manipulator is manufactured, as shown in Fig. 17. The driving mode of the soft manipulator is a pneumatic drive. By controlling the gas pressure inside the soft manipulator, the bending degree of the soft manipulator is directly affected; thus, the corresponding gripping force is obtained. According to the requirements of the pneumatic drive control method, the control process of the entire control system is obtained (Fig. 18).

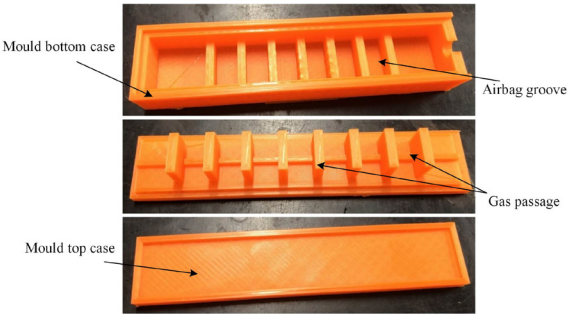

Fig. 16. *Mould of soft manipulator*

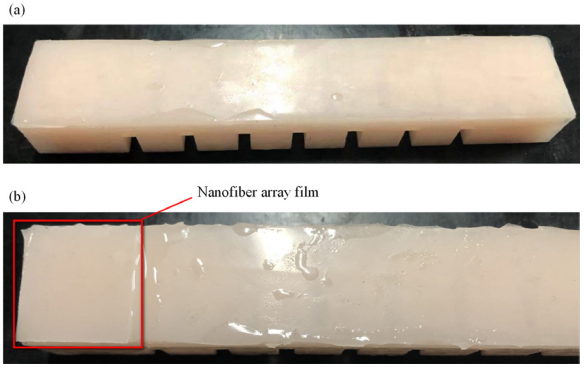

Fig. 17. *Soft manipulator; a) manipulator with no nanofibre array film attached; and b) manipulator with nanofibre array film attached*

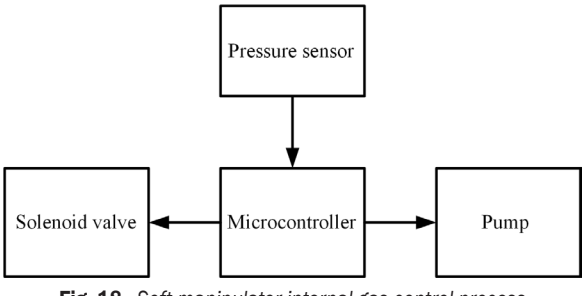

Fig. 18. *Soft manipulator internal gas control process*

In current robotics applications, the urgent need for productivity and precision highlights the crucial need to replace traditional control strategies

with modern ones. Therefore, closed-loop feedback control is necessary [35] to [37]. In this paper, the control system is divided into four main parts: a microcontroller that plays a major control role (Arduino Mega 2560), a pump (DC miniature diaphragm pump) that supplies gas pressure, a valve that controls the internal communication between the pump (SMC-VQ110U-5M model solenoid valve) and the soft manipulator, and a pressure sensor that measures the gas pressure inside the manipulator in real-time. The microcontroller is the core control component that reads the pressure value transmitted by the pressure sensor and controls the opening and closing of the pump switches and valves to control the flow of air to the soft manipulator. According to the control requirements, the control strategies are set as shown in Fig. 19.

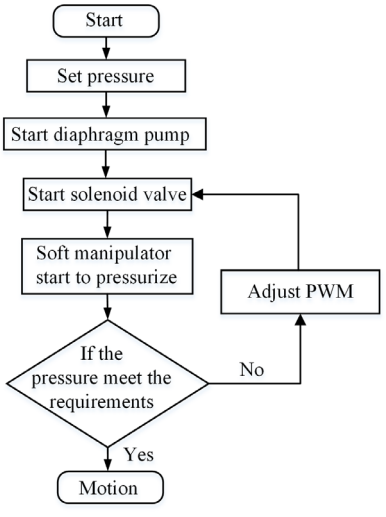

Fig. 19. *Control strategy of soft manipulator*

Experimental steps:

(1) Adjust the potentiometer and set the solenoid valve gas pressure.
(2) Open the diaphragm pump so that it begins to provide pressure to the system.
(3) Open the solenoid valve to allow gas to pass inside the software robot.
(4) The pressure sensor that is electrically connected to the soft manipulator measures the gas pressure inside in real-time and transmits the measured pressure data to the microcontroller.
(5) If the pressure meets the requirements, then, no adjustment is made; if the pressure fails to meet the expected value, then, the potentiometer is adjusted to modify the duty cycle of the pulse width modulation (PWM) signal, thereby controlling the frequency of the opening and closing of the solenoid valve and the gas inside the soft manipulator.

Fig. 20 shows the grasp experiment system of the soft manipulator. The pressure test is performed on each pressure channel, and the pressure value of the sensor is obtained, as shown in Fig. 21.

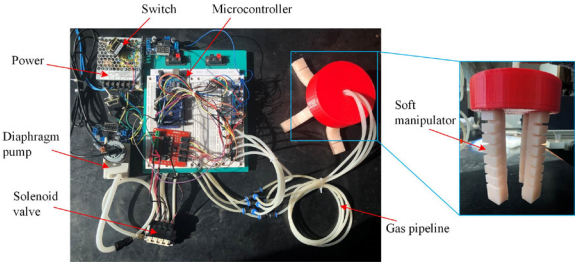

Fig. 20. *Grasp experiment system of soft manipulator*

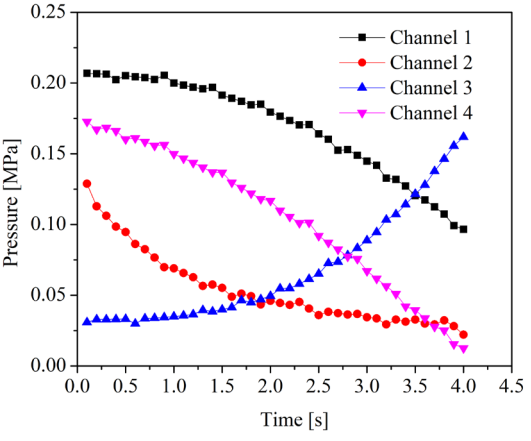

Fig. 21. *Variation of pressure in each channel during testing*

The pressure changes can be seen in Fig. 21. The pressure of the four channels partially changes when the potentiometer is adjusted, thereby indicating that the system can work normally. Moreover, the pressure of the four-channel system exceeds0.1 MPa. According to the simulation results, this pressure can fully meet the requirements of the soft manipulator bending.

The stress test of a single manipulator are performed, and its bending angles under different pressures are tested. Subsequently, the test and simulation results are compared (Fig. 22). The testing pressures are set as 0.1 MPa, 0.2 MPa, 0.3 MPa, 0.4 MPa, and 0.5 MPa.

The bending angles under the finite element analysis and under the pressure test fit well (Fig. 22), thereby proving that the simulation results of the soft manipulator are reliable and can be used as the basis for the design of the soft manipulator structure.

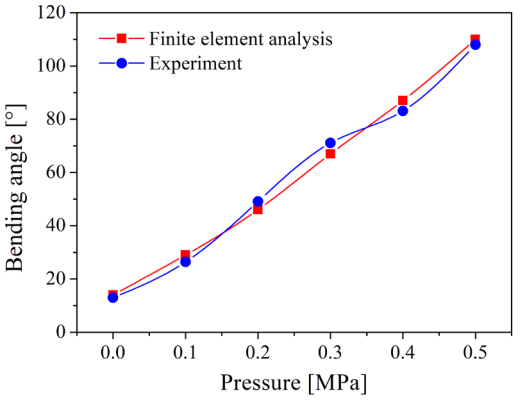

Fig. 22. *Bending angle of soft manipulator under finite element analysis and experimental analysis*

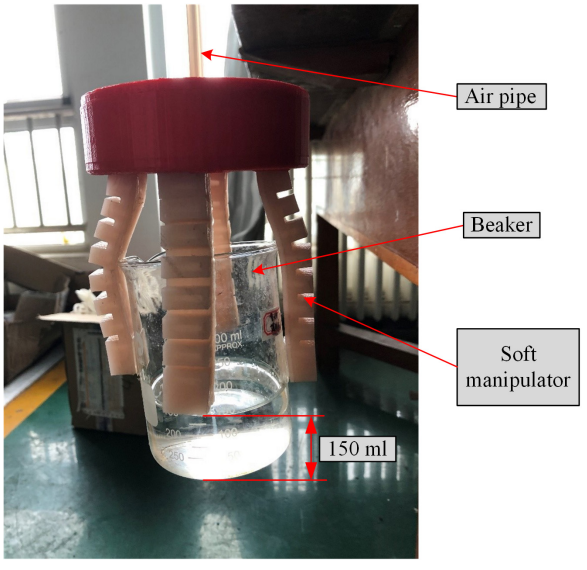

Fig. 23. *Grasp experiment of soft manipulator*

The grasp experiment is carried out using the built-up soft manipulator measurement and control system. The object to be grabbed is a beaker. The original weight of the beaker is 147.7 g. Water is added to the beaker to increase the weight of the grabbed object, and Fig. 23 illustrates the grasping process. In the experiment, the final water addition is approximately 150 ml; that is, the final grab weight of the soft manipulator is 300 g and indicates that the soft manipulator optimization has good application effect.

4 CONCLUSION

A friction-enhanced multi-airbag soft manipulator is developed in the paper, and the pneumatic drive is selected as the driving method of the software robot. Firstly, finite element analysis of the manipulator is performed. Under the influence of the length and depth, the change angles of the bending angle of the soft manipulator are 122.6° and 179.5°, respectively. The remaining influencing factors include the width W and the airbag spacing x. The thickness of the silica gel is affected by the impedance change when the deformation is changed. The bending forces of the soft body are −120.0° and −124.5°, respectively. The width of the airbag and the number of airbags also have a certain influence on the bending of the soft manipulator. The changes in the angle are 60.2° and 68.7°. The change in these two parameters alters the length of the soft manipulator, the width of the airbag, and the number of airbags. The increase in those parameters will increase the length of the soft manipulator; moreover, the force and deformation resistance will not change, thereby changing the bending angle of the soft manipulator. Secondly, the expression of the Neo-Hooke strain energy function is obtained, according to the mechanical tensile test. According to the strain energy function, the finite element analysis method is utilized to examine the influence of the change in soft manipulator size parameters on the force bending. The theoretical analysis results confirm that the finite element analysis outcomes are correct. Finally, the software manipulator is manufactured and the pressure channel tests, bending angle tests, and grasp experiment are carried out. The weight of 300 g can be lifted by the manipulator, thereby indicating that the soft manipulator designed in this research has good application effect and prospect.

5 ACKNOWLEDGEMENTS

The authors wish to acknowledge the National Natural Science Foundation of China (No. 51779267), financial support of Open Fund of Key Pre-Research Foundation of Military Equipment of China (No.6140923030702), Doctoral Innovation Engineering Project (No. YCX2019056).

6 NOMENCLATURES

α	Arc corresponding to the bending, [°]
λ_i	Main elongation ratio
ε_i	Main direction strain, [MPa]
κ	Bulk modulus of the material
μ	Poisson's ratio of the material
r_a	The radius of the arc, [mm]
h	Soft manipulator height, [mm]
G	Shear modulus of the material, [MPa]
F_Δ	Inner and outer wall force difference, [N]
F_s	Force on the inner wall, [N]

L_T Inner and outer arc length difference, [mm]
P_s Gas pressure received by the inner wall, [MPa]
S_Δ Inner and outer wall area difference, [mm²]
S_L Left side of the airbag, [mm²]
S_{LT} Left end area of the manipulator, [mm²]
S_R Right side of the airbag, [mm²]
S_{RT} Right end area of the manipulator, [mm²]
S_s Area of force inside the soft manipulator, [mm²]
W Strain energy function

7 REFERENCES

[1] Iqbal, J., Ullah, M.I., Khan, A.A., Irfan, M. (2015). Towards sophisticated control of robotic manipulators: An experimental study on a pseudo-industrial arm. *Strojniški vestnik - Journal of Mechanical Engineering*, vol. 61, no. 7-8, p. 465-470, **DOI:10.5545/sv-jme.2015.2511**.

[2] Ajwad, S.A., Iqbal, J., Islam, R.U., Alsheikhy, A., Almeshal, A., Mehmood, A. (2018). Optimal and robust control of multi DOF robotic manipulator: Design and hardware realization. *Cybernetics and Systems*, vol. 49, no.1, p. 77-93, **DOI:10.1080/01969722.2017.1412905**.

[3] Rus, D., Tolley, M.T. (2015). Design, fabrication and control of soft robots. *Nature*, vol. 521, no. 7553, p. 467-475, **DOI:10.1038/nature14543**.

[4] Elango, N., Faudzi, A.A.M. (2015). A review article: investigations on soft materials for soft robot manipulations. *The International Journal of Advanced Manufacturing Technology*, vol. 80, no. 5-8, p. 1027-1037, **DOI:10.1007/s00170-015-7085-3**.

[5] Dupac, M., Noroozi, S. (2014). Dynamic modeling and simulation of a rotating single link flexible robotic manipulator subject to quick stops. *Strojniški vestnik - Journal of Mechanical Engineering*, vol. 60, no. 7-8, p. 475-482, **DOI:10.5545/sv-jme.2013.1544**.

[6] Marchese, A.D., Rus, D. (2016). Design, kinematics, and control of a soft spatial fluidic elastomer manipulator. *The International Journal of Robotics Research*, vol. 35, no. 7, p. 840-869, **DOI:10.1177/0278364915587925**.

[7] Blanes, C., Ortiz, C., Mellado, M., Beltrán, P. (2015). Assessment of eggplant firmness with accelerometers on a pneumatic robot gripper. *Computers and Electronics in Agriculture*, vol. 113, p. 44-50, **DOI:10.1016/j.compag.2015.01.013**.

[8] Ranzani, T., Cianchetti, M., Gerboni, G., De Falco, I., Menciassi, A. (2016). A soft modular manipulator for minimally invasive surgery: design and characterization of a single module. *IEEE Transactions on Robotics*, vol. 32, no. 1, p. 187-200, **DOI:10.1109/TRO.2015.2507160**.

[9] Erkaya, S. (2018). Effects of joint clearance on the motion accuracy of robotic manipulators. *Strojniški vestnik - Journal of Mechanical Engineering*, vol. 64, no. 2. p. 82-94, **DOI:10.5545/sv-jme.2017.4534**.

[10] Galloway, K.C., Becker, K.P., Phillips, B., Kirby, J., Licht, S., Tchernov, D., Wood, R.J., Gruber, D.F. (2016). Soft robotic grippers for biological sampling on deep reefs. *Soft Robotics*, vol. 3, no. 1, p. 23-33, **DOI:10.1089/soro.2015.0019**.

[11] Diller, E., Sitti, M. (2014). Three-dimensional programmable assembly by untethered magnetic robotic micro-grippers. *Advanced Functional Materials*, vol. 24, no. 28, p. 4397-4404, **DOI:10.1002/adfm.201400275**.

[12] Ge, Q., Sakhaei, A.H., Lee, H., Dunn, C.K., Fang, N.X., Dunn, M.L. (2016). Multimaterial 4D printing with tailorable shape memory polymers. *Scientific Reports*, vol. 6, p. 31110, **DOI:10.1038/srep31110**.

[13] Yuk, H., Lin, S., Ma, C., Takaffoli, M., Fang, N.X., Zhao, X. (2017). Hydraulic hydrogel actuators and robots optically and sonically camouflaged in water. *Nature Communications*, vol. 8, p. 14230, **DOI:10.1038/ncomms14230**.

[14] Ongaro, F., Scheggi, S., Yoon, C., van den Brink, F., Oh, S.H., Gracias, D.H., Misra, S. (2017). Autonomous planning and control of soft untethered grippers in unstructured environments. *Journal of Micro-Bio Robotics*, vol. 12, no. 1-4, p. 45-52, **DOI:10.1007/s12213-016-0091-1**.

[15] Hughes, J., Iida, F. (2018). Tactile sensing applied to the universal gripper using conductive thermoplastic elastomer. *Soft Robotics*, vol. 5, no. 5, p. 512-526, **DOI:10.1089/soro.2017.0089**.

[16] Wan, J., Yao, J., Zhang, L., Wu, H. (2018). A weighted gradient projection method for inverse kinematics of redundant manipulators considering multiple performance criteria. *Strojniški vestnik - Journal of Mechanical Engineering*, vol. 64, no. 7-8. p. 475-487, **DOI:10.5545/sv-jme.2017.5182**.

[17] Brown, E., Rodenberg, N., Amend, J., Mozeika, A., Steltz, E., Zakin, M.R., Lipson, H., Jaeger, H.M. (2010). Universal robotic gripper based on the jamming of granular material. *Proceedings of the National Academy of Sciences*, vol. 107, no. 44, p. 18809-18814, **DOI:10.1073/pnas.1003250107**.

[18] Deaconescu, T., Deaconescu, A. (2017). Pneumatic muscle-actuated adjustable compliant gripper system for assembly operations. *Strojniški vestnik - Journal of Mechanical Engineering*, vol. 63, no. 4, p. 225-235, **DOI:10.5545/sv-jme.2016.4239**.

[19] Behl, M., Kratz, K., Zotzmann, J., Nöchel, U., Lendlein, A. (2013). Reversible bidirectional shape-memory polymers. *Advanced Materials*, vol. 25, no. 32, p. 4466-4469, **DOI:10.1002/adma.201300880**.

[20] Kim, H.-I., Han, M.-W., Wang, W., Song, S.-H., Rodrigue, H., Ahn, S.-H. (2015). Design and development of bio-mimetic soft robotic hand with shape memory alloy. *2015 IEEE International Conference on Robotics and Biomimetics*, p. 2330-2334, **DOI:10.1109/ROBIO.2015.7419122**.

[21] Lau, G.-K., Heng, K.-R., Ahmed, A.S., Shrestha, M. (2017). Dielectric elastomer fingers for versatile grasping and nimble pinching. *Applied Physics Letters*, vol. 110, no. 18, p. 182906, **DOI:10.1063/1.4983036**.

[22] Alam, W., Mehmood, A., Ali, K., Javaid, U., Alharbi, S., Iqbal, J. (2018). Nonlinear control of a flexible joint robotic manipulator with experimental validation. *Strojniški vestnik - Journal of Mechanical Engineering*, vol. 64, no. 1, p. 47-55, **DOI:10.5545/sv-jme.2017.4786**.

[23] Li, L. (2018). Mechanism design and motion planning of parallel-chain nonholonomic manipulator. *International Journal of Simulation Modelling*, vol. 17, no. 2, p. 327-336, **DOI:10.2507/IJSIMM17(2)C07**.

[24] Yang, Y., Chen, Y., Li, Y., Wang, Z., Li, Y. (2017). Novel variable-stiffness robotic fingers with built-in position feedback. *Soft Robotics*, vol. 4, no. 4, p. 338-352, **DOI:10.1089/soro.2016.0060**.

[25] Fei, Y., Wang, J., Pang, W. (2019). A novel fabric-based versatile and stiffness-tunable soft gripper integrating soft pneumatic fingers and wrist. *Soft Robotics*, vol. 6, no. 1, p. 1-20, **DOI:10.1089/soro.2018.0015**.

[26] Connolly, F., Polygerinos, P., Walsh, C.J., Bertoldi, K. (2015). Mechanical programming of soft actuators by varying fiber angle. *Soft Robotics*, vol. 2, no. 1, p. 26-32, **DOI:10.1089/soro.2015.0001**.

[27] Jang, J.-S. (2005). Simultaneous trajectory tracking control of position and force with pneumatic cylinder driving apparatus. *Journal of Mechanical Science and Technology*, vol. 19, no. 5, p. 1107-1115, **DOI:10.1007/BF02984032**.

[28] Dong, H., Asadi, E., Qiu, C., Dai, J., Chen, I.-M. (2018). Geometric design optimization of an under-actuated tendon-driven robotic gripper. *Robotics and Computer-Integrated Manufacturing*, vol. 50, p. 80-89, **DOI:10.1016/j.rcim.2017.09.012**.

[29] Rodrigue, H., Bhandari, B., Han, M.-W., Ahn, S.-H. (2015). A shape memory alloy–based soft morphing actuator capable of pure twisting motion. *Journal of Intelligent Material Systems and Structures*, vol. 26, no. 9, p. 1071-1078, **DOI:10.1177/1045389X14536008**.

[30] O'Halloran, A., O'Malley, F., McHugh, P. (2008). A review on dielectric elastomer actuators, technology, applications, and challenges. *Journal of Applied Physics*, vol. 104, no. 7, p. 9, **DOI:10.1063/1.2981642**.

[31] Treloar, L.R.G. (1944). Stress-strain data for vulcanized rubber under various types of deformation. *Rubber Chemistry and Technology*, vol. 17, no. 4, p. 813-825, **DOI:10.5254/1.3546701**.

[32] Mooney, M.A. (1940). A theory of large elastic deformation. *Journal of Applied Physics*, vol. 11, no. 9, p. 582-592, **DOI:10.1063/1.1712836**.

[33] Ogden, R.W. (1982). Elastic deformations of rubberlike solids. *Mechanics of Solids*, p. 499-537, **DOI:10.1016/B978-0-08-025443-2.50021-5**.

[34] Ramadani, R., Belsak, A., Kegl, M., Predan, J., Pehan, S. (2018). Topology optimization based design of lightweight and low vibration gear bodies. *International Journal of Simulation Modelling*, vol. 17, no. 1, p. 92-104, **DOI:10.2507/ijsimm17(1)419**.

[35] Li, Y., Liu, L., Feng, G. (2018). Robust adaptive output feedback control to a class of non-triangular stochastic nonlinear systems. *Automatica*, vol. 89, p. 325-332, **DOI:10.1016/j.automatica.2017.12.020**.

[36] Ajwad, S.A., Iqbal, J., Ullah, M.I., Mehmood, A. (2015). A systematic review of current and emergent manipulator control approaches. *Frontiers of Mechanical Engineering*, vol. 10, no. 2, p. 198-210, **DOI:10.1007/s11465-015-0335-0**.

[37] Vidaković, J., Kvrgić, V., Lazarević, M. (2018). Control system design for a centrifuge motion simulator based on a dynamic model. *Strojniški vestnik - Journal of Mechanical Engineering*, vol. 64, no. 7-8, p. 465-474, **DOI:10.5545/sv-jme.2018.5272**.

Strojniški vestnik - Journal of Mechanical Engineering 66(2020)1, 51-60
DOI:10.5545/sv-jme.2019.6157
Original Scientific Paper
Received for review: 2019-05-27
Received revised form: 2019-08-13
Accepted for publication: 2019-09-27

Stress Analysis of a Pipeline as a Hydropower Plant Structural Element

Stefan Ćulafić[1,*] – Taško Maneski[2] – Darko Bajić[1]
[1]University of Montenegro, Faculty of Mechanical Engineering, Montenegro
[2]University of Belgrade, Faculty of Mechanical Engineering, Serbia

This paper describes pipeline stress analysis, primarilybranch junctions, as a structural element in hydro-power plants. Pipelines are exposed to internal pressure,which is present under working conditions. Analysis of stresses in the pipeline of the hydropower plant is based on analytical, numerical, and experimental methods. In this paper, we will define the critical elements of the pipeline. After that, we will determine critical areas in the branch junction, under experimental conditions, where strain gauges should be installed. The obtained resultsshow that a boiler formula can be efficiently applied in the stress analysis. Also, a correlation between the internal pressure and the maximum circumferential stresses in the elastic zone is given. In the final sections of the paper, the limit value of the internal pressure as a load for which stress in the zone of plasticity appears and the safety factor of the branch junction in the exploitation conditions are determined. The contribution of this work is the unification and deepening of the topic related to the problem of the testing ofhydro-power structural elements.
Keywords:pipeline, branch junction, hydropower plant, strength analysis, shell intersection

Highlights
- *A boiler formula can be efficiently applied in the stress analysis.*
- *Correlation between the internal pressure and the maximum circumferential stresses in the elastic zone is given.*
- *The limit value of the internal pressure as load for which stress in the zone of plasticity appears.*
- *The safety factor of the branch junction in the exploitation conditions is determined.*

0 INTRODUCTION

When studying hydropower plants, special attention should be paid to the analysis of the strength of certain parts of the hydropower plant. With a high-quality analysis of the stress of individual parts of the plant, it is possible, with sufficient accuracy in real conditions, to anticipate the critical areas for remediation, evaluation and reduction of the maintenance costs, which should ultimately extend the lifetime of the powerplant.

The interesting shell problem has not yet been investigated sufficiently. The practical importance of this problem requires further investigation, including that of the elastic stress analysis of the intersecting shells of the various shapes subjected to different loadings and the elastic-plastic analysis **[1]**.

The geometry of hydropower plants' structural elements is very complex with large number of discontinuities; therefore, stress and strain analysis on these elements is also complex. Analytical analysis is possible only in a small number of very simple cases. Numerical analysis based on the finite element method is usedwhen analysing stresses of structural elements in pipelines, primarily pipeline branch junctions. It is a very real problem of defining locationsand areas of pipeline in which reinforcements should be made **[2]** and also a problem of the estimation of limitin which yield stresses are observed **[3]**, defining stress concentration factor, limit load **[4]** and **[5]**, and burst pressure **[6]**. The use of experimental methods is very difficult under real, working conditions, because it is not possible to vary internal pressure in real conditions in some structural elements, such as branch junctions, until plastic strainsare observedunder working conditions. Because of this, it is more convenient to perform experiments on the model of the structural element under laboratory conditions and, on the basis ofthese results, make conclusions about what is happening in the real elements.

By combining numerical and experimental methods, it has been shown thatthe most accurate results are obtained when determining critical stresses, which (in some places) can lead to problems in the exploitation and functioning.The subject of this paper is the analysis of stress distribution in structural elements of a pipeline:
- applying analytical procedures,
- finite element method (FEM) application on the real element with real dimensions,
- FEM application on the element model,
- applying experimental analysis on the model under laboratory conditions.

*Corr. Author's Address: University of Montenegro,Faculty of Mechanical Engineering , Blvd. G. Wash., 81000, Podgorica, Montenegro, sculafic@ucg.ac.me

1 METHODS

Analytical, numerical, and experimental procedures were applied in the analysis of the stress of structural elements. One specific feature is in the fact that the experiment was realized not on a real structural element but on its model. Numerical analysis was also carried out on a real structural element and on a structural element model.

2 ANALYTICAL AND NUMERICAL STRESS ANALYSIS OF PIPELINE

The main characteristic of pipes in the pipeline is that their radius is much larger than the thickness ($R>>t$), so it can be adopted that these pipes are actually shell pipeline.

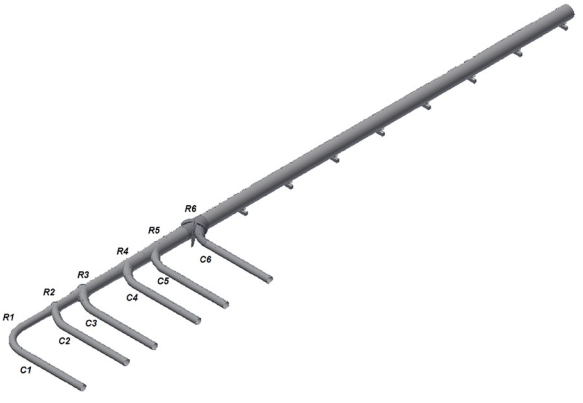

Fig. 1. *FEM pipeline model*

Static linear finite element analysisin the elasticity area was performed for the pipeline, i.e., its straight main tube parts and the knee part using Autodesk INVENTOR 2016 software. Due to a highly complex geometry,which has been analysed, the finite element (FE) analysis was used with caution, and also was confirmed with the KOMIPSstand-alone software package. FEM mesh was generated using 3D iso-parametric solid elements. A 3D model of the pipeline is shown in Fig. 1.The pipeline length is approximately 200 m, and itis exposed to 51 bar of internal pressure under exploitation conditions. It can be remarked that the basic elements of the pipeline are branch junctions: R1,R2,R3,R4,R5,R6 (where branch junctions are actually knee pipes which direct the water)and pipes: C1,C2,C3,C4,C5,C6.

An analytical solution for the parts of the pipeline that is made of straight tubes with no junctions or nozzles is given. An analytical solution is also given for the pipeline knee (Fig. 2).

Analytical equations for the determination of stresses in the torus shell pipeline (Fig. 2)are known as follows:

$$\sigma^{O} = \frac{p \cdot R\left(2a \pm R\right)}{2t\left(a - R\right)}, \tag{1}$$

$$\sigma^{p} = \frac{p \cdot R}{2t}, \tag{2}$$

where p is internal pressure, R radius of a circular cross-section, a radius of a torus, σ^{O} circumferential stress, and σ^{p} longitudinal stress.

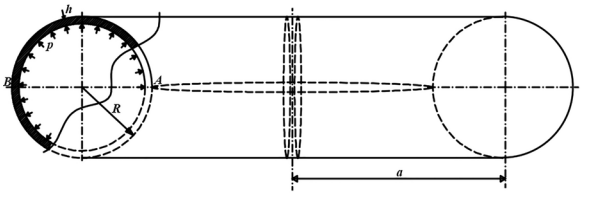

Fig. 2. *Torus shell part of the pipeline*

Especially, if $a=\infty$ it is a cylindrical shell, and if $a=0$ it is a spherical shell. On the basis of Eq. (1), the stresses can be calculated on all parts of the pipeline, except for branch junctions. It is thus possible to calculate the stresses on the kneepart R1 and the straight pipes of the pipeline (C1, …, C6).

Therefore, for points A and B of the knee R1 pipe ($a=4650$ mm, $R=600$ mm, $t=18$ mm, $p=51$ bar): $\sigma_A^O=182.6$ MPa, $\sigma_B^O=160.3$ MPa, $\sigma^p=85$ MPa, and for the pipes C1 and C6: C1: σ^O = 170 MPa, $\sigma^p=85$ MPa, C6: $\sigma^O=212.5$ MPa, $\sigma^p=106.25$ MPa.

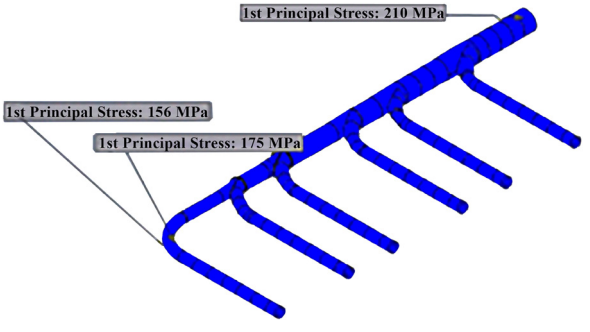

Fig. 3. *FEM pipeline model*

Since there wasone plane of symmetry, boundary conditions were the following: all translations normal to the plane of symmetry and all rotations in the plane of symmetry are constrained.

The material used in the FEM analysis was the most similar to thecharacteristics of NIOVAL 47, which are material properties of the pipeline under real working conditions. This is also important

because of the correlation with the analytical results for whichYoung's elasticity modulus for steel has been used. A constant internal pressure of 51 bar was the implied load used in the finite element analysis.

Based on the numerical analysis,the stress values of which are given in Fig. 3, and analytical analysis, it can be seen that the pipeline branch junctions, especially branch junction number C6, are the most affected elements of the whole pipeline, so only branch junction number C6 will be the subject of further analysis.

2.1 FEM Analysis of the Pipeline Branch Junction (Real Dimensions)

Pipeline branch junctions (cylinder-to-cylinder intersections) are very often used in industrial engineering. Reduction of the base material due to penetration of the intersecting cylinder is the cause for stress concentration.

Authors [6] indicate that cylinder-to-cylinder intersections are a widespread occurrence in many industrial applications. Difficulties in obtaining analytical evaluations of the stress distributions in the disturbed regions near the intersection of comparably sized shells originally stemmed from the complicated geometrical shape of the intersection line. The intersection curve of the middle surfaces of the cylinders is neither rotationally symmetric, nor on a plane curve, but rather is a spatial curve. Moreover, the sharp discontinuities of curvatures across the intersection curve increase the stress.

Therefore, the presence of the stress concentration is inevitable and, as a consequence, constitutes a significant consideration in the design.

In paper [7] online monitoring proposition was given, and in papers [8] and [9] analysis of the pipeline branch junction in real dimensions wasperformed using FEM. The primary pipe diameter on the branch junction entrance is 2.5 m, while pipe diameter at the exit is 2.35 m. FEM was performed using AUTODESK Inventor 2016 software, in which we created the geometric model and performed the stress-strain analysis.

In Figs. 4 to 7, yield stresses are given when a pipeline branch junction in real dimensions is exposed to 20 bar, 50 bar and 84 bar, and 51 bar pressure.

Results of the FEM analysis shows that yield stress appears in the area next to the anchor of the pipeline branch junction. This particular area was specified (and referred to in Table 1 as MP1) as area of highest stress values. In Table 1, values of maximal circumferential stresses are given as a function of internal pressure values. Generally speaking, it can be said that thedependence of the value of stresses on pressure is very satisfactorylinear in the field of elastic strains, which further means that the branch junction, which is essentially a shell, is not loaded on bending.

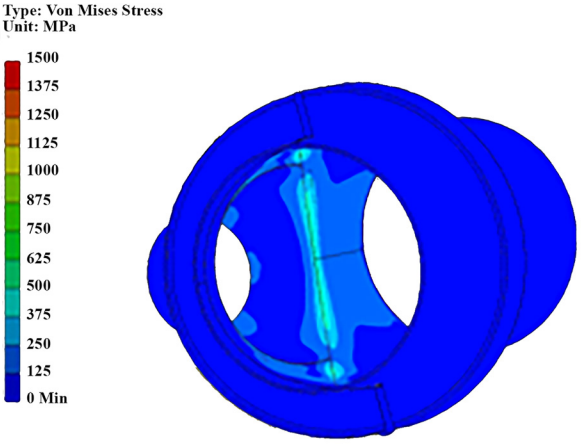

Fig. 4. *FEM branch junction under 20 bar pressure*

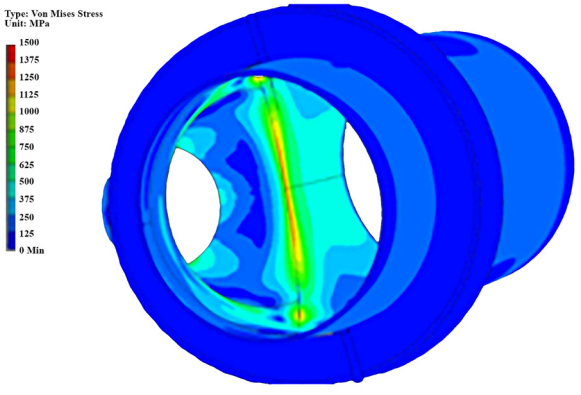

Fig. 5. *FEM branch junction under 50 bar pressure*

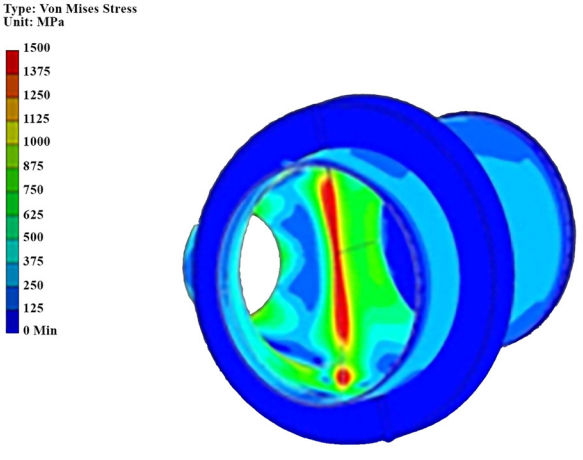

Fig. 6. *FEM branch junction under 84 bar pressure*

Table 1. *Stress values for MP1*

Pressure values [bar]	Stress values for MP1 [MPa]
20	111
50	284
84	458

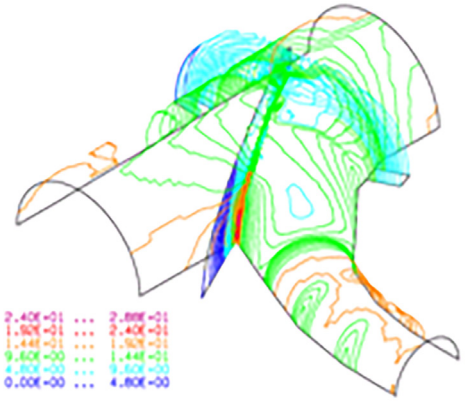

Fig. 7. *Equivalent stress under 51 bar pressure*

3 EXPERIMENTAL

3.1 Branch Junction Model Manufacture

The material used for the construction of pipe elements of the real object is NIOVAL 47, manufacturer SIJ – Slovenian Steel Group. The mechanical properties of this material are given in Table 2. In the absence of NIOVAL 47, which, due to exploitation problems, ceased to be produced during the 1970s, we analysed the steel of the same class with the most similar mechanical properties. That is steel S355J2 + AR. It was used to produce the branch junction model. The mechanical properties of this material are given in Table 3.

Table 2. *Mechanical properties of the material NIOVAL 47*

Tensile strength, Rm [MPa]	Yield strength, Re [MPa]	Elongation, A [%]
650	470	24

Table 3. *Mechanical properties of the material S355J2+AR*

Tensile strength, Rm [MPa]	Yield strength, Re [MPa]	Elongation, A [%]
554	360	28.2

Branch junction model (partitions Ø2500/Ø2350/Ø1200mm) was made **[10]** of steel S355J2+AR, based on boiler formula. Branch model was created with the following characteristics:

- model dimensions are five times smaller than the real object,
- thickness is 10 times smaller.

Calculus per taining to stresses in the branch junction construction is analytically possible only in cylindrical parts of the junction, except for stiffeners, ribs and holes. The formula in which the stresses calculus is obtained is called the “boiler formula”.

Boiler formula for stresses calculuson the cylinder (pipe, vessel) exposed to internal pressure without ribs and holes is Eq. (2) for the longitudinal direction of a cylinder and for:

- circumferential direction of a cylinder:

$$\sigma^{o} = \frac{p \cdot R}{t}, \tag{3}$$

where p is fluid internal pressure [bar], R cylinder radius [mm] and t cylinder thickness [mm].

From Eqs. (2) and (3), an observation can be made that values of the stresses in the circumferential direction are twice the value along the longitudinal direction.

A branch junction model should give the same stress as the real object has. This is secured by the application of similarity method in the following manner:

$$\sigma^{o} = \frac{p \cdot R}{t} \left(= \frac{\frac{p}{2} \cdot \frac{R}{5}}{\frac{t}{10}} \right) = \frac{p_{model} \cdot R_{model}}{t_{model}}. \tag{4}$$

Derivation of the same stress value is as follows: $p_{model}=p/2$, $R_{model}=R/5$, $t_{model}=t/10$.

Real branch junction: $p=50$ bar, $R=1250$ mm, $t=36$ mm, $\sigma^{o}=174$ MPa, ($R=34.77\times t$).

Branch junction model: $p=25$ bar, $R=250$ mm, $t=4$ mm, $\sigma^{o}=156$ MPa.

This means that the branch junction model for thesame value of thepressure has twice the value of circumferential stresses. This also meansthe branch junction model has to be subjected to two times lower pressure so it could be correlated to the real branch.

In terms of manufacturing, we have adopted the previous relations. Since there was no 3.6 mm sheet, a 4 mm sheet was adopted. In this way, around 10 % smaller values of stresses are obtained. Anchor stresses are the same, since thicknesses are 8 mm forthe model and 80 mm forthe real branch.

Similarity method is applied on this branch junction model, because in its construction there is a negligible presence of bending stresses, as we concluded in the real branch analysis, which depends on a square (t^2) of the thickness of the material.

3.2 FEM Analysis of Branch Junction Model

A three-dimensional model of the branch junction of the basic dimensions and thicknesses is showninFig.8. It was made for the requirements of the strength analysis using FEM. Branch geometry was modelled using surfaces.

In numerical modelling, the branch is subjected to 10 bar of internal pressure on the walls. Due to linear static nature of the analysis of the construction (obtained stress has linear character compared to the given pressure), it is possible to use scaling to obtain results for different values of internal pressure. Taking into consideration the symmetry of the branch in longitudinal direction, one-half of the branch was analysed.

Mesh was more detailed in the areas of calotte penetration, where higher values of stress were expected. To control and confirm experimental analysis using strain gauges, FEM model was madeas well as necessary calculus.

Fig. 10 shows the positions of strain gauges on the branch. These exact locations will be usedfor the comparison of results between experimental tests and numerical results.

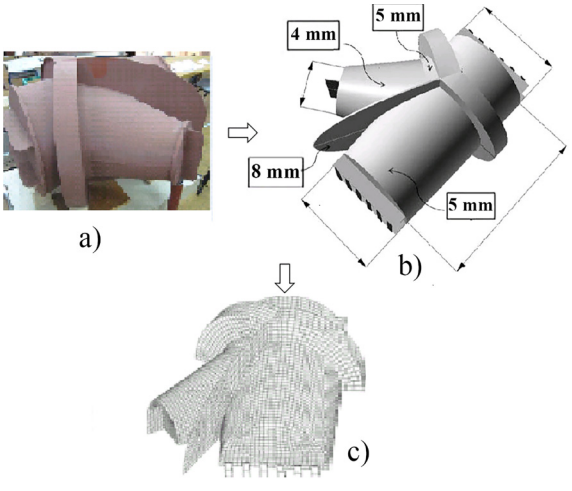

Fig. 8. *Branch junction model; a) model in laboratory, b) FEM model, and c) mesh view*

Boundary conditions are given as two constraints: translation and rotation, and since one plane of symmetry exists, the boundary conditions that were used were that all the nodes on the symmetric section were constrained against deformation in the perpendicular direction.

Fig. 9 shows the resultsof the FEM analysis as Von Mises yield stress and alsoas stresses in circumferential (vertical) direction. All results are related to the pressure of 10 bar. Also, Table 4 shows the exact values of circumferential stresses readings within the FEM model. These values are referred to as measuring positions MP1, MP2, and MP3.

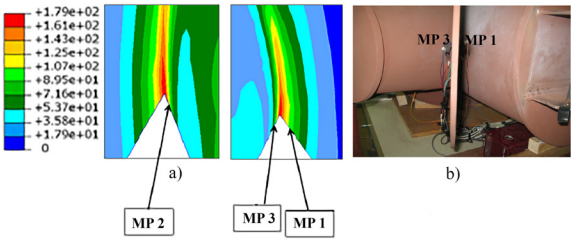

Fig. 9. *Measuring positions of strain gauges; a) FEM view, and b) model view*

Table 4. *Values of stresses at measuring positions*

	MP1	MP2	MP3
Stress incircumferential direction [MPa]	115	89	58
Von Mises stress [MPa]	107	84	63

The following conclusionscan be made based on the FEM analysis of the real branch junction and branch junction model:

1. The boiler formula gives, with very satisfactory accuracy, the correlation between the results on the real branch and branch model. This lies in the fact that the circumferential stresses on the MP1 are about the same, and amount to 111 MPa on the real branch junction and 115 MPa on the branch junction model. As the branch junction model is made on the basis of the boiler formula, we come to the previously stated conclusion. Furthermore, laboratory investigations have shown, based on the results obtained, what will happen with the branch junction under working conditions.
2. Yield stresses are visible in the area of the junctions of the main pipe (Ø2500 mm) and anchor and branch pipe (Ø1200 mm) and anchor, though it should be expected that measurements will show that the critical gauge position is position one.

3.3 Experimental Analysis of Branch Junction Model

Based on the results obtained using the FEM, it is possible to define areas at which strain gauges should be placed and, based on the similarity theory,it is possible to determinethe internal pressure in the real branch junction precisely before plastic strain occurs.

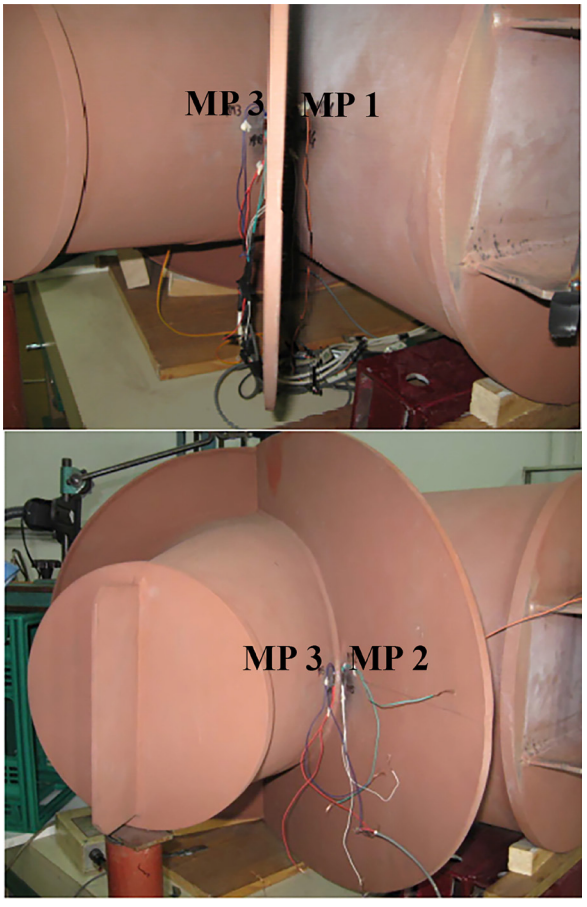

Fig. 10. *Measuring positions: MP1, MP2, MP3*

Measuring places are designated as follows: MP1, MP2, ..., MP8. Due to the complexity of the material, andobserved values of stresses in some measuring spots, focus of our attention will be onthe measuring positions MP1, MP2, MP3 (Fig. 10) where MP1 is acircumferential direction of bigger cylinder, MP2 a vertical direction of anchor, and MP3 a circumferential direction of the conical part of the model.

Numerical analysis of the branch junction in real conditions and the branch junction model have shown that biggest stresses are in MP1 (Tables 3 and 4).

Twenty-three experiments were conducted for each measuring position.

Values of the stress for any value of the pressure are obtained when scaling these values by a given factor.

In the following Figs. 11 and 12 graphical representation of measured stresses in all measuring positions and experiments conducted are givenas the function of pressure and time.

It can be seen from Figs. 11 and 12 how the stresses change at all measuring positions with the change of internal pressure. At the pressure of 20 bar, the value of the stress on MP1 is slightly higher than 200 MPa. It is also noted that the MP1 stress is dominant in relation to the stresses at other measuring positions. After that, the highest stress value is on MP2. Also, it should be noted that after unloading, the internal pressure returns to the initial, i.e.,zero, and that this release is accompanied by the stresses that also return to zero. This further means that, as far as the stress condition is concerned, the process is related to elasticity, i.e., stresses do not reach the value that belongs to plastic strain beyond the yield point.

Table 5 shows mean values based on all experiments at MP1,MP2,MP3, when pressure is reduced to 10 bar.

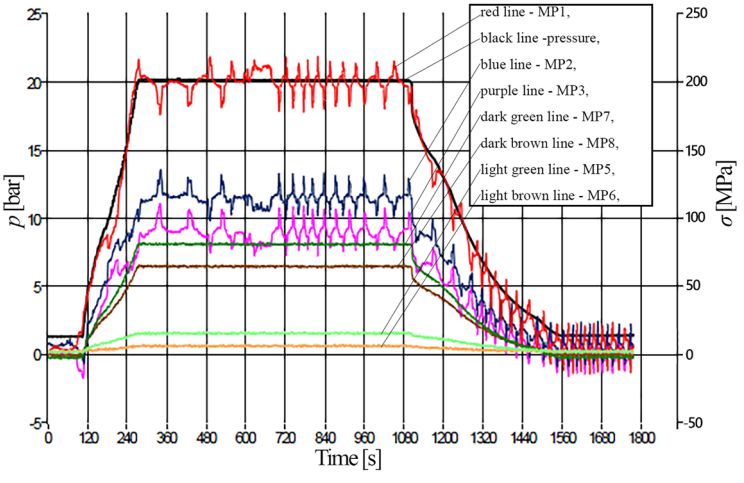

Fig. 11. *Internal pressure and stress as the function of time (elastic strain)*

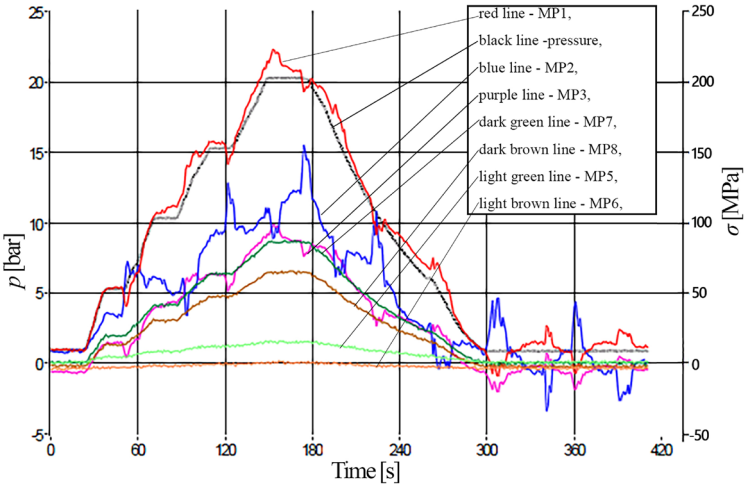

Fig. 12. *Internal pressure and stress as the function of time (elastic strain)*

Table 5. *Mean values of stress on measuring positions (MP)*

MP	Pressure value [MPa] under 10 bar
MP1	110
MP2	75
MP3	50

This scaling only applies until yield point and enables the acquisition of any value of pressure stresses.

4 RESULTS

4.1 Comparison of the Measurements and the FEM Calculation

Table 6 gives values of stress intensities for the positions MP1, MP2, MP3 at the branch junction model obtained when the FEM calculation is applied and when measuring values (for 10 bar) were obtained [11]. The general conclusion is that these values are very close, which puts these two methods in equal position and simultaneously confirms each other.

Table 6. *Mean values of stresses at MP1, MP2, MP3*

MP	Stress [MPa]	
	FEM	Measured
MP1	115	110
MP2	89	75
MP3	58	50

4.2 Determination of Limit Internal Pressure

When the pressure is increased to 30 bar, the stress on MP1 reaches a value of about 370 MPa (Fig. 13). It is also important to note that after unloading, i.e. bringing the internal pressure to zero, the stress value on MP1 does not return to zero, but has a value of 50 MPa. This means that there is a permanent deformation corresponding to this stress. When, after the permanent deformation, the branch junction model is again submitted to the pressure of 30 bar, the stresses at MP1, after unloading return to the new starting level of 50 MPa.

From Fig. 14, it can be seen that when the pressure is increased to 32 bar to 33 bar, additional permanent deformation of the branch model at MP1 is made, for additional 50 MPa. When the branch model is unloaded, the stress at MP1 is 100 MPa. Fig. 15 shows the behaviour of the stress on the MP1 model of the branch when the internal pressure reaches the value of 40 bar to 45 bar. It can be seen that the stress value at MP1 reaches 850 MPa.

The pressure of 45 bar on the branch junction model corresponds to 90 bar on the real branch junction. From the diagram shown in Fig. 15, it can be seen that the stress value is about 850 MPa. If we deduct from this value the value of the stress due to the plastic strain of about 350 MPa, we obtain the value of about 500 MPa, which corresponds to the internal pressure of 90 bar on the real branch or 45 bar on the branch model. This further means that the result given in Table 1 is logical (pressure of 42 bar on the branch model or 84 bar on the real branch) and corresponds

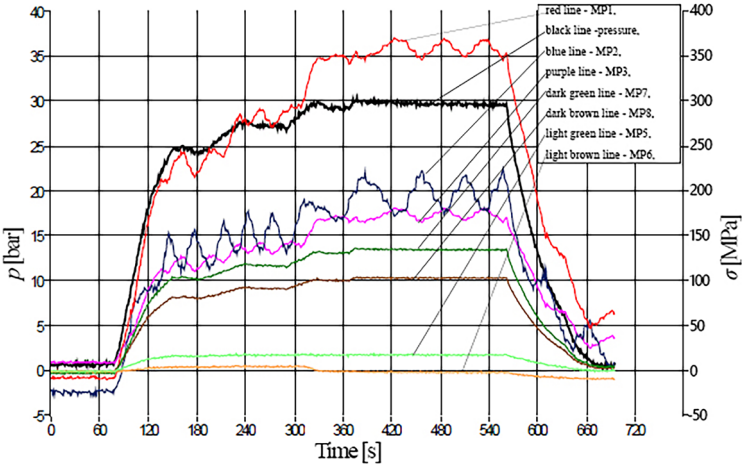

Fig. 13. *Internal pressure and stress as the function of time (plastic strain)*

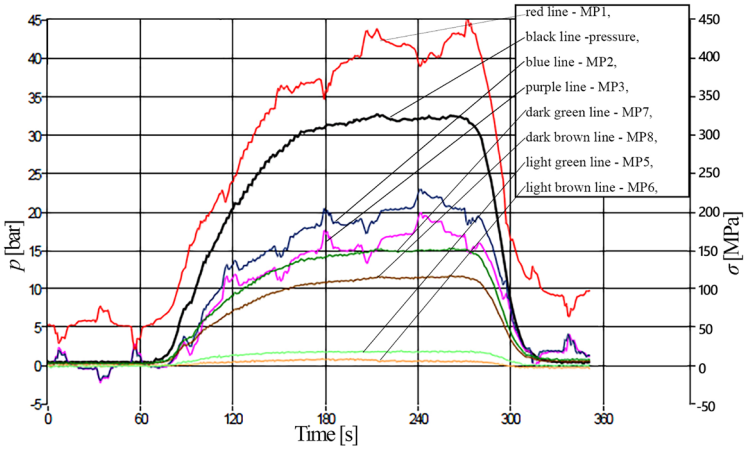

Fig. 14. *Internal pressure and stress as the function of time (plastic strain)*

to the maximum stress value of 458 MPa at MP1.The explanation lies in the fact that the results given in Table 1 are related to the assumption that all analyses based on the finite element method are related to the field of elasticity.

4.3 Determination of Safety Factor

In the paper [12] a procedure for the determination of the stress concentration factorwas given. As the continuation of this paper, we will determine the safety factor.

Initial plastic strains of the branch junction model appear on MP1 under the pressure of 30 bar.

Calculation of necessary pressure for the occurrence of the initial plastic strains on the real branch junction on the measuring position MP1 (position of maximum stress) is as follows:

$$P = 30 \text{ bar} \times 0.9 \times (47/36) \times 2 = 70.5 \text{ bar}. \quad (5)$$

Factor 0.9 represents the relation of the thickness of the real branch junction and branch junction model on the position MP1 36/(4×10) = 0.9. Relation 47/36 represents the relation of yield point of the material of the branch (NIOVAL 47) and of the branch model (St355J/AR). Factor 2 is model factor, which refers to the pressure.

The safety factor in the branch junction exploitation in relation to the plastic strains is 70.5/51 = 1.38.

From Fig. 15 (blue line, MP2), it can be seen that the first plastic strains on MP2 appear when the pressure reaches 45 barcorresponding to the stress of 70 MPa to 80 MPa. If the pressure of 45 bar is reduced by 5 bar, we conclude that at the pressure is about 40 bar, the first plastic strains appear.

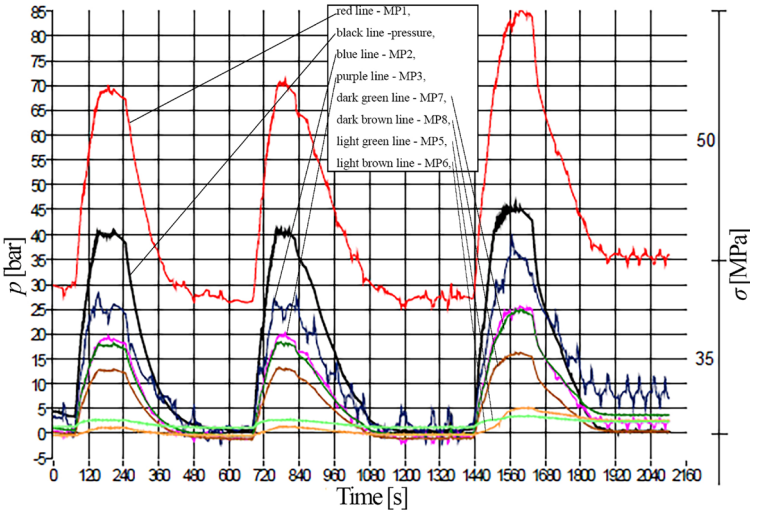

Fig. 15. *Internal pressure and stress as the function of time (plastic strain)*

Calculation of necessary pressure for the appearance of initial plastic strain on the real object of the pipeline branch junction on MP2 is:

$$p = 40 \text{ bar} \times (47/36) \times 2 = 104.44 \text{ bar}. \quad (6)$$

Stress values on other measuring positions are even lower.

5 CONCLUSION

This paper attempts to use analytical, numerical, and experimental methods to describe the problem of the stress analysis inthe pipeline. It is shown that thecritical structural element of the pipeline is the pipeline branch junction. The following analyses have been carried out:

- Analytical and numerical analysis for the pipes of the pipeline and thekneesection of the pipeline;
- Numerical analysis of the branch junction in real dimensions;
- Numerical analysis of the branch junction model;
- Experimental analysis of the branch junction model.

Based on Eqs. (2) and (3), we defined the measuring places where the strain gauges should be placed. Also, it is shown that the boiler formula is correct for loads in which the plastic strain zone is not reached. Our paper also shows the linear correlation betweeninternal pressure andmaximum circumferential stress, which means thatbending stressescan be neglected, i.e. the branch junction can be treated and observed as a membraneshell. In case of appearance of the trapped air pockets, pressure will become unsteady [13] and [14]. This paper analysis only steady pressure.

Based on the experimental analysis of the branch junction model, it can be concluded how a real-dimension branch junction will behave under internal pressure,under real working conditions. It was shown that the results pertaining to obtaining stresses with numerical method on the real branch junction, results pertaining to obtaining stresses with numerical method on the branch model junction and results pertaining to the experimental determination of stress values are such that satisfactory accuracy has been reached, as it can be seen from Tables 4 and 6. Also, based on the experimental analysis, the limit pressure value was defined based on the point at which the first plastic strain is noted, which enabled us to define the maximum value of pressure under working conditions on the real branch junction necessary to achieve plastic strain (70.5 MPa). Thisenabled us to define the safety factor (1.38) in the branch junction exploitation as well as for the whole pipeline.

6 REFERENCES

[1] Skopinsky, V.N. (1993). Numerical stress analysis of intersecting cylindrical shells. *Journal of Pressure Vessel Technology*, vol. 115, no. 3, p. 275-282, **DOI:10.1115/1.2929528**.

[2] Barry, R.M., Venter, G. (2019). Analysis of reinforcement designs for specials in steel pipelines. *International Journal of Pressure Vessels and Piping*, vol. 169, p. 204-214, **DOI:10.1016/j.ijpvp.2018.12.005**.

[3] Kim, S.-H., Gim, J.-M., Wang, M., Kim, Y.J. (2016) .Simplified limit load estimation using mα-tangent method for branch pipe junctions under internal pressure and in-plane

bending. *Procedia Structural Integrity*, vol. 2, p. 2583-2590, **DOI:10.1016/j.prostr.2016.06.323**.

[4] Plancq, D., Berton, M.N. (1998). Limit analysis based on elastic compensation method of branch pipe tee connection under internal pressure and out-of-plane moment loading. *International Journal of Pressure Vessels and Piping*, vol. 75, no. 11, p. 819-825, **DOI:10.1016/S0308-0161(98)00085-4**.

[5] Kim, Y.-J., Lee, K.-H., Park, C.-Y. (2008). Limit loads for piping branch junctions under internal pressure and in-plane bending- extended solutions. *International Journal of Pressure Vessels and Piping*, vol. 85, no. 6, p. 360-367, **DOI:10.1016/j.ijpvp.2007.11.007**.

[6] Sang, Z.F., Xue, L.P., Lin, Y.J., Widera, G.E.O. (2002). Limit and burst pressures for a cylindrical shell intersection with intermediate diameter ratio. *International Journal of Pressure Vessels and Piping*, vol. 79, no. 5, p. 341-349, **DOI:10.1016/S0308-0161(02)00028-5**.

[7] Sedmak, A. (2011). *Program for an On-Line Monitoring of Metal State in Pipeline no. 3 at HPP Perucica*. Faculty of Mechanical Engineering, Podgorica.

[8] Culafic, S. (2015). *Numerical and experimental analysis of stress state in pipeline branch in HP Perucica*. MSc. thesis, Faculty of Mechanical Engineering faculty, Podgorica.

[9] Ćulafić, S., Bajić, D., Maneski, T. (2015). Numerical model of pipeline branch in HP Perucica. *Proceedings of the 2ND International Conference onNew Technologies*, p. 27-32.

[10] Bajic, D., Maneski, T. (2011). *Investigation of Branch Junction A6 Pipeline no. 3. at HPP Perucica*. Faculty of Mechanical Engineering, Podgorica.

[11] Bajić, D., Ćulafić, S. (2017). Comparison of Numerical and Experimental Results of Stress-Deformation State in a Pipeline Branch. *Scientific Proceedings XIV International Congress on Machines,Technologies, Materials*, p. 29-32.

[12] Bajić, D., Momčilović, N., Maneski, T., Balać, M.,Kozak, D., Ćulafić, S. (2017). Numerical and experimental determination of stress concentration factor for a pipe branch model. *Tehnički vjesnik – Technical Gazette*, vol. 24, no. 3, p. 687-692, **DOI:10.17559/TV-20151126222916**.

[13] Bergant, A., Tijsseling, A., Kim, Y.I., Karadžić, U., Zhou, L., Lambert, M., Simpson, A. (2018). Unsteady pressures influenced by trapped air pockets in water-filled pipelines. *Strojniški vestnik - Journal of Mechanical Engineering*, vol. 64, no. 9, p. 501-512, **DOI:10.5545/sv-jme.2018.5238**.

[14] Bergant, A., Karadžić, U., Tijsseling, A.S. (2016). Dynamic water behavior due to one trapped air pocket in a laboratory pipeline apparatus. *IOP Conference Series: Earth and Environmental Science*, vol. 49, p. 967-976, **DOI:10.1088/1755-1315/49/5/052007**.

Strojniški vestnik - Journal of Mechanical Engineering 66(2020)1, 61-70

DOI:10.5545/sv-jme.2019.6156 Original Scientific Paper
Received for review: 2019-05-27
Received revised form: 2019-08-13
Accepted for publication: 2019-09-27

A Cyber-Physical Approach to the Management and Control of Manufacturing Systems

Elvis Hozdić*[1] – Dominik Kozjek[1] – Peter Butala[1, 2]
1 University of Ljubljana, Faculty of Mechanical Engineering, Slovenia
2 Tshwane University of Technology, Department of Industrial Engineering, South Africa

Cyber-physical systems (CPSs) open up new perspectives for the design, development, implementation, and operation of manufacturing systems and will enable a paradigm shift in manufacturing. The objective of this research is to develop a new concept of cyber-physical production systems (CPPSs) and, on this basis, to address the issue of management and control, which is crucial for the effective and efficient operation of manufacturing systems. A new model of CPPS is proposed. The model integrates digitalized production planning, scheduling, and control functions with a physical part of manufacturing system and enables the self-organization of the elements in production. A case study demonstrates feasibility of the approach through the use of simulation experiments, which are based on real industrial data collected from a company that produces industrial and energy equipment.
Keywords: cyber-physical production system, production planning and control, self-organization

Highlights
- *A conceptual model of cyber-physical production systems (CPPSs) is developed.*
- *A cyber-physical approach to the production planning and control (PPC) of manufacturing systems is presented.*
- *The presented approach to the production planning, scheduling and the self-organization in the CPPS is demonstrated through the use of simulation experiments.*

0 INTRODUCTION

A new production philosophy that has recently emerged under the name of Industry 4.0 opens up a space for novel approaches to industrial production. Industry 4.0 is a new way of organizing and controlling complete value-adding systems **[1]**. Industry 4.0 (I4.0) is driven by new scientific discoveries, enriched knowledge, new and better materials, and new technologies, especially in the field of information and communication technologies (ICT). In addition, novel organizational forms and the innovative managerial principles of emergence, self-organization, learning, open innovation, collaboration, and the networking of humans and organizations will become the key elements of the next generation of manufacturing systems.

Modern manufacturing enterprises must be focused on agile, networked, service-oriented, green, and social manufacturing practices, among others **[2]**. However, in order to develop and implement these practices, a transformation of manufacturing systems from the traditionally isolated, hierarchical structures into open and distributed networked structures is needed. The foundations of this transformation are the three key enablers of I4.0: connectivity, digitalization and cybernation. One of the novel concepts arising from I4.0 is the so-called cyber-physical systems (CPSs).

The CPS integrates computational and physical processes. In a CPS, embedded computers and networks monitor and control the physical processes, usually with feedback loops in which physical processes affect the computations and vice versa **[3]**. On this basis, cyber-physical production systems (CPPS) are also defined **[4]** to **[11]**.

In a CPPS the horizontal integration is accomplished through value networks, and the vertical integration is achieved through networked manufacturing systems **[6]**.

The emergence of CPSs and cross-linked CPPSs will lead to a fundamental restructuring of manufacturing work and logistic systems, and will require new forms of human-machine interaction **[12]**. Furthermore, innovative methods for the management and control of CPPSs based on logistics models will improve the processing of customers' orders **[13]**.

An important part of the management and control of manufacturing systems, which allows them to cope with this challenge, are the functions of production planning and control (PPC) **[14]**. Several emerging approaches to the management and control of traditional manufacturing systems are presented in **[15]** to **[18]**.

Unlike with traditional approaches, a CPPS will enable the decomposition of a user's request into several tasks and assign them to distributed heterogeneous features in a parallel- computing

*Corr. Author's Address: University of Ljubljana, Faculty of Mechanical Engineering, Aškerčeva 6, 1000 Ljubljana, Slovenia, ehozdic@yahoo.com

environment [19]. In this context, self-organization could be a viable alternative for solving the dynamic scheduling problem [20].

Several emerging approaches to the management and control of CPPS are presented in [12], [13] and [21] to [25].

The current research in the field of the management and control of CPPSs offers innovative approaches, but they are not yet implemented in industrial environments. An appropriate methodology that would integrate different levels of decision making in a manufacturing enterprise and which would enable the responsive and adaptive management and control of manufacturing systems in real time is still absent.

This research addresses the question of how the CPPS concept can contribute to the improved management, planning, scheduling, control and monitoring of manufacturing systems. It is expected that within CPPSs these functions will be reinforced through connectivity, digitalization and cybernation at different levels of the decision-making in an enterprise. This will enable the management and control of manufacturing systems in real-time.

The paper proposes a novel CPPS model and introduces a new method for the management and control of CPPSs in real time. Furthermore, generic cybernetic, and functional models for deploying PPC functions within CPPSs are presented.

The remainder of the paper is organized as follows. In Section 1, the new conceptual model of CPPS is introduced. In Section 2, the cyber-physical approach to the management and control of CPPSs is proposed. In Section 3, the use of the approach is illustrated with a case study based on industrial data. Section 4 summarizes the work carried out and provides suggestions for future research.

1 MODEL OF CYBER-PHYSICAL PRODUCTION SYSTEMS (CPPSs)

The objective of this research is to develop a new concept of CPPSs and, on this basis, to address the issue of management and control, which is crucial for the effective and efficient operations of the manufacturing systems. The development originates from previous work on basic manufacturing structures such as elementary work systems (EWS) [26], autonomous work systems (AWS) [27], complex adaptive manufacturing systems (CAMS) [26], and adaptive distributed manufacturing systems (ADMSs) [27]. These structures symbolized in terms of cybernetic models, represent a sound basis for their upgrading into appropriate CPPS models.

The question here is how to implement the mentioned three key I4.0 enablers, i.e., connectivity, digitalization and cybernation in the existing EWS, AWS, CAMS and ADMS models of manufacturing systems in order to realize the concept of cyber-physical production systems at all levels and thus to enable the seamless connectivity among all the elements and systems, and the transmission of information and decision making in real time. In the next section the transformation of EWS, AWS, CAMS and ADMS into appropriate CPS models is elaborated.

1.1 CPPS Conceptual Model

The generic conceptual model of a CPPS is shown in Fig. 1.

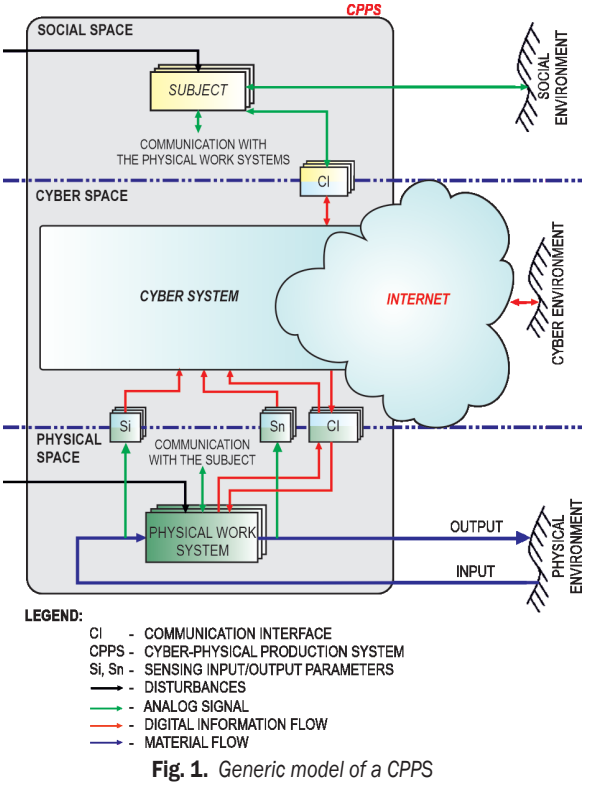

Fig. 1. *Generic model of a CPPS*

The model consists of three elements: (1) the human *Subject* as a social element, (2) the cyber system (CS) as a cyber element, and (3) the physical work system (PWS) as a physical element. Each of the elements exists in its own space: the *Subject* in the social space, the CS in the cyber space and the PWS in the physical space. The connectivity between these elements and thus between the different spaces is enabled via the corresponding communication interfaces, which also bridge the different spaces.

Each element has the corresponding relations with its specific environment: the *Subject* with the business and social environment, the CS with the cyber environment and the PWS with the physical environment. The PWS structure is based on the EWS structure [26].

The important distinction between the EWS and the PWS is that in the latter the *Subject* is moved from the physical space to the social space of the CPPS. The new element of the model is the cyber system (CS), which is incorporated into the cyber space, Fig. 1. The CS of the CPPS can be structured into three hierarchical levels: 1) operational level, 2) coordination & collaboration level, and 3) business level, Fig. 2. Thus, it represents a CPS version of the CAMS (factory).

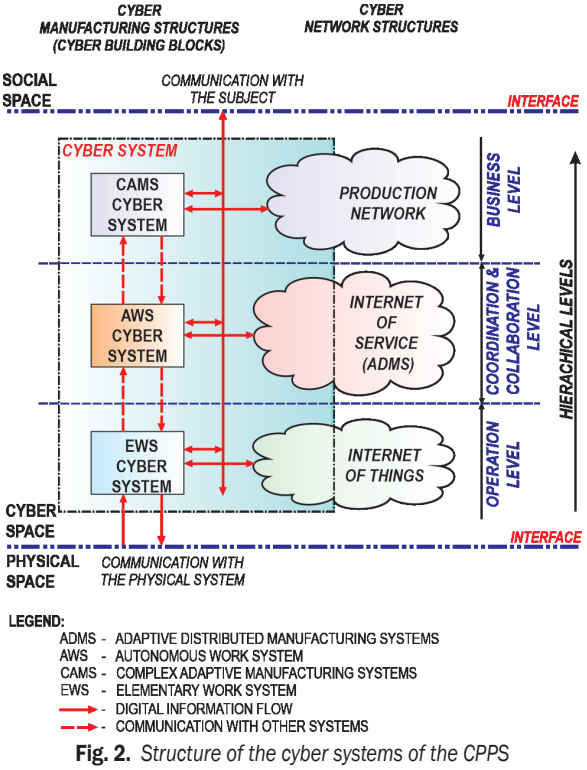

Fig. 2. *Structure of the cyber systems of the CPPS*

The infrastructure of the CS enables vertical connectivity between the cyber manufacturing structures (EWS cyber system, AWS cyber system and CAMS cyber system) and the horizontal connectivity of the cyber manufacturing structures in the network structures (Internet of Things, Internet of Services (ADMS), and the production network).

The EWS cyber system enables 1) connecting the physical and social spaces in the EWS, 2) digitalization of the functions (e.g., monitoring and control) and the cybernation and work processes in the EWS, 3) development and implementation of new digitalized functions in the EWS (e.g., self-organization, self-adaption, self-diagnostic, self-learning, etc.), 4) vertical connection of the EWS in the integrated work structure (AWS, CAMS, ADMS, production networks), and 5) horizontal connection of the EWS in a network within the Internet of Things, Fig. 2. The EWS cyber system structure is shown in Fig. 3.

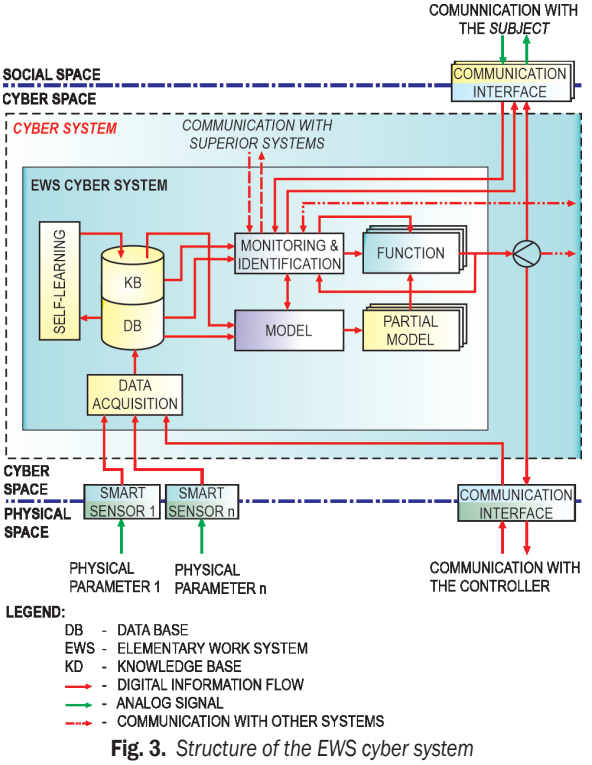

Fig. 3. *Structure of the EWS cyber system*

The new function of self-organization in the EWS cyber system is presented in more detail in Section 2, through a description of the cyber-physical approach to the management and control of the CPPS.

The AWS cyber system enables 1) vertical connection with subordinated EWS cyber systems, as well as with superior cyber systems, 2) implementation of the digitalized autonomous function in the AWS (management of resources, scheduling, quality control, performance measurements, prognostics, self-learning, etc.), and 3) horizontal connection of the AWS and ADMS within the Internet of Services.

The AWS cyber system is connected with the superior system (the CAMS cyber system) through the coordination function, while it is connected to the subordinate systems (the EWS cyber systems) through the monitoring and control functions, as shown in Fig. 2. The AWS cyber system structure is shown in Fig. 4.

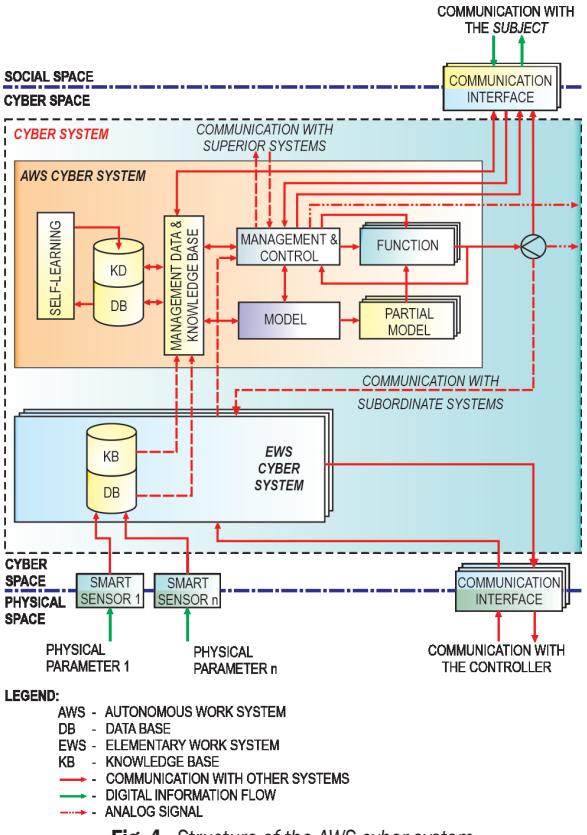

Fig. 4. *Structure of the AWS cyber system*

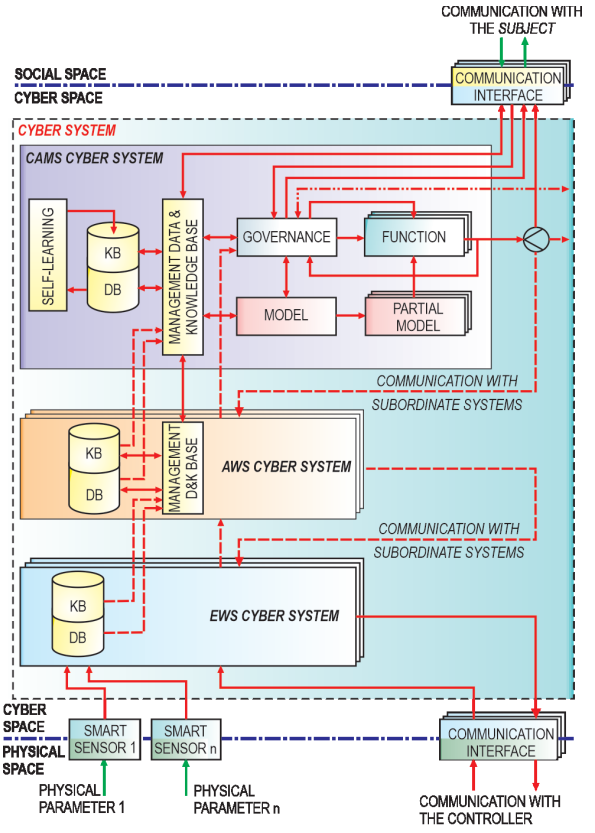

Fig. 5. *Structure of the CAMS cyber system*

The digitalized function of scheduling in the AWS cyber system is presented in Section 2 and validated in Section 3 through a simulation experiment.

The CAMS cyber system, as show in Fig. 2, enables 1) horizontal connection of the CPPS in a production network or other networked forms, 2) vertical connection with subordinated AWS cyber systems and EWS cyber system, and 3) implementation of functions such as sales, marketing, purchasing, project management, design, production planning, quality assurance, etc. The CAMS cyber system structure is shown in Fig. 5.

In Section 2 the management and control of CPPSs with particular emphasis on the production planning and control is described in more detail.

2 MANAGEMENT AND CONTROL OF CPPSs

The managing of manufacturing systems such as factories is, due to their ever-increasing complexity, a very demanding function. It affects all the actors in the system and decisively influences the system's performance. For this reason, the digitalization and cybernation of the function could have various beneficial aspects.

An important part of the management function in a manufacturing system is related to PPC. The major issue with PPC is how to achieve the on-time delivery of products and services in accordance with customers' orders using the available resources and within the anticipated costs.

The PPC function is performed at all three levels of the manufacturing system. Hence, it is a comprehensive domain for researching cyber-physical concepts in manufacturing systems.

2.1 Production Planning and Control in CPPSs

The application of the CPPS concept in the PPC domain is outlined next. The overall concept of PPC in the CPPS is illustrated in Fig. 6.

Fig. 6 shows a functional diagram of the activities related to PPC. These activities are spread over all three levels of the manufacturing system: from the business level down to the execution level. This gives

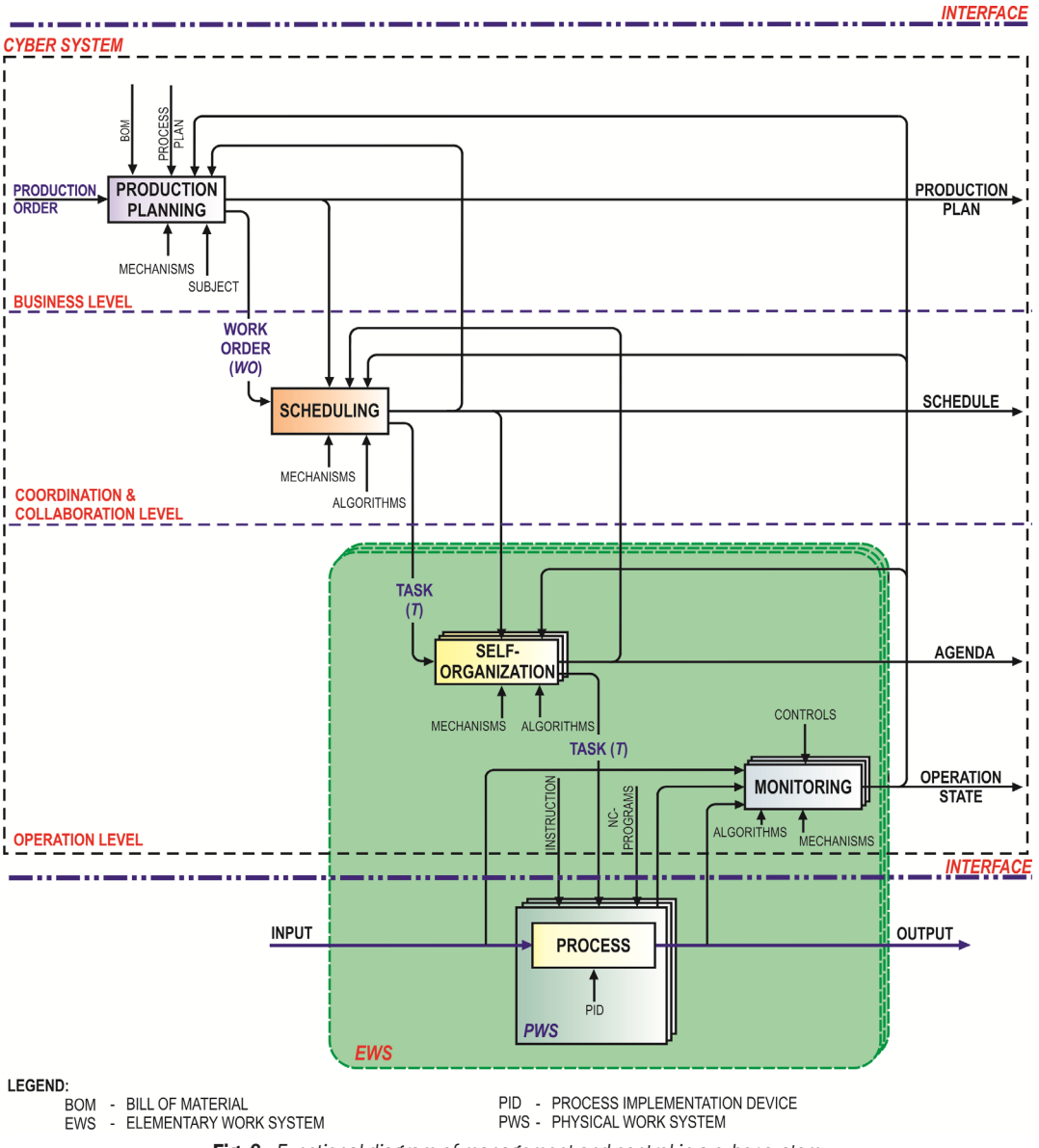

Fig. 6. *Functional diagram of management and control in a cyber system*

us the opportunity to elaborate how the CPPS concept can be implemented by connecting the cybernated functions from different levels of the manufacturing system in series and/or in parallel within the cyber system, as well as how to connect them with the physical system.

As can be seen in Fig. 6, the core of the PPC system is located in the cyber system. This implies the digitalization and cybernation of the PPC functions.

Besides the traditional PPC functions, i.e., production planning, scheduling and monitoring, an enhanced control function is introduced at the operation level; it is called self-organization. The role of this function is to allow the EWSs to arrange their own agendas for tasks by themselves. This function is introduced in the next.

The *Self-organization* activity is a part of the EWS cyber system. It enables the EWS to make autonomous decisions about its work planning and organization. The self-organization function is activated for each new event (delay in performing tasks, arrival of a new task, system fault, etc.).

The output of the self-organization is the list of the tasks in the form of an agenda. The agenda is the set of the self-organized tasks for the individual EWS.

The agenda of the EWS is a sequence of allocated tasks.

The time of the new event, t_{NE}, is defined with the new events, a new look into the state, and similar. The new events are the completion of a task, the arrival of a new task, the delay of the tasks, etc.

The task schedule in a single agenda defines the various heuristic scheduling algorithms such as first-in-first-out (FIFO), earliest-due-date (EDD), weighted-shortest-processing-time (WSPT), shortest processing time (SPT), largest number of successors (LNS), and similar.

The dynamic production environment in which the PWS exists is continually influenced by the EWS's individual agenda and requires it to be constantly refreshed in real time. The CPPS concept enables the adaptation of the agenda in different real-time conditions by defining various alternative agendas for a particular EWS.

Which agenda, i.e., which variants of the heuristic scheduling algorithms will be used, depends on the evaluation function of the agenda. The agenda-evaluation function is based on the performance measures of an assessment. The basic performance measures of an assessment an agenda include the parameters of the tasks depending on the execution times and the deadlines (start times, finish times, completion duration time, delay, tardiness, earliness, due date, etc.).

The implementation of a cybernated PPC can be realized using different mechanisms, such as for example multi-agent system (MAS).

The presented approach of the production planning, scheduling and the self-organization in the CPPS is demonstrated in the following case study.

3 CASE STUDY

The case-study experiments are based on real manufacturing data sourced from a typical engineer-to-order (ETO) company that produces industrial and energy equipment, such as turbines, pumps, valves and gates, cranes, and other products and solutions.

ETO manufacturing is typically a project-oriented type of manufacturing. For the development, a project is structured according to the principle of work breakdown into smaller components, i.e., parts, modules, sub-assemblies, or higher-level tasks. For each of these components there is one or more work orders, and each work order defines a set of tasks, or in the case of production, a sequence of tasks that must be executed on different work stations.

In the observed company it is typical for several dozen projects and approximately one thousand work orders to be in the process at any given moment. The proposed CPS approach will be used to manage both the large-scale and dimensionality of the problem related to the management of work orders and the tasks on the shop floor.

A production-scenario simulation tool, presented in [28], is used during the experiments. The simulation tool is based on pre-processed Manufacturing Execution System (MES) data (Table 1). Source MES data is a backup of the observed ETO company′s MES database for a period of 18 months.

The aforementioned tool simulates how work orders pass across the shop floor by knowing the work orders' sequences of tasks, the work orders' start times, the processing times of the tasks, the corresponding EWS of each task, etc. A start time for a work order is determined as the actual start time of

Table 1. *Structure of the pre-processed MES data*

Entity	Symbol	Attributes	Symbol	No. of records
Task	***T***	Task-identification number	T_{ID}	58865
		Elementary work system-identification number	EWS_{ID}	
		Planned start time	t_{TSPL}	
		Actual processing time	t_{TPAC}	
		Corresponding work order-identification number	$(W0_{ID})$	
		Corresponding WBS code	WBS_{code}	
Work order	***W0***	Work order-identification number	$W0_{ID}$	14421
		Actual start time (date and time)	t_{W0AC}	
		Planned start time (date)	t_{W0SPL}	
		Planned completion time (due date)	tF_{W0DD}	
		Sequence of tasks (ordered list of tasks)	TL	
Elementary work system	***EWS***	Elementary work system-identification number	EWS_{ID}	352
		List of similar work systems	EWS_L	

the first corresponding task, and the sequence of tasks for an individual work order is determined by the sequence of the tasks' actual start times.

The simulation tool makes it possible to test different heuristic algorithms for the scheduling tasks. In the following experiments this functionality will be used to demonstrate the usability and the effects of the proposed approach.

The three different heuristic algorithms for the scheduling tasks are tested in the experiments: 1) FIFO, 2) EPT, and 3) EPT&WSO.

FIFO: when several tasks are waiting to be processed in some work system, the selected task that will be the first to be processed in that work system is the task with the longest waiting time.

EPT: the selected task that will be the first processed is the task with the earliest planned start time.

EPT&WSO: the earliest-planned-time and the current occupancy of the work systems for which the current work orders will be processed after they pass the observed work system are integrated. Among all the tasks in the observed work system, the task that has the largest value of the indicate function (G), Eq. (1), is selected to be the first processed at that work system, where α is the normalized delay of the observed task and β is the normalized average number of tasks in the following EWSs of the work order to which corresponds the observed task $\boldsymbol{T}$, and w_α and w_β are the weights.

$$G = \frac{\left(w_\alpha \cdot \alpha + w_\beta \cdot \beta\right)}{\left(w_\alpha + w_\beta\right)}. \tag{1}$$

A normalized delay α for the observed task is defined in Eq. (2), where $d(\boldsymbol{T})$ is the start delay of the task in the agenda; d^*_{min} and d^*_{max} are the minimum and maximum values of $d(\boldsymbol{T})$ among all the tasks in the observed EWS from the past. In the implementation of the EPT&WSO algorithm used for the experiments of this study, when searching for the d^*_{min} and d^*_{max} values, the most extreme values are ignored.

$$\alpha = \frac{d\left(\boldsymbol{T}\right) - d^*_{min}}{\left(d^*_{max} - d^*_{min}\right)}. \tag{2}$$

A weight w_α Eq. (3) is defined with the maximum value of d_{max}, which is the maximum value of $d(\boldsymbol{T})$ among all the current tasks in the observed EWS, where L_α is the limit value of the delay and it is determined on the basis of the experience and characteristics of the observed production system. The practical purpose of this weight is the following: if there is a task with a shorter time reserve in the set of tasks, then the start delays of the task should be taken into account with increased weight when generating the agenda. For the experiments of this study, δ was set to 0.1 and L_α was set to –30 days.

$$w_\alpha = \begin{cases} 1; & d_{max} \geq L_\alpha \\ \delta; & d_{max} < L_\alpha \end{cases}. \tag{3}$$

The normalized average number of tasks in the following EWS of the observed work order β is defined in Eq. (4), where m_j is the number of waiting tasks in the EWS of the j^{th} task after the observed task in the work order′s sequence to which corresponds the observed task; m_{max} is the maximum number of waiting tasks among all the EWSs from the past; and $\mathcal{M}$ is the number of subsequent tasks that follow the currently observed task in the corresponding work order′s sequence of tasks.

$$\beta = \frac{-\sum_{j=1}^{\mathcal{M}} \frac{m_j}{m_{max}}}{\mathcal{M}}. \tag{4}$$

A weight w_β is defined in Eq. (5), where L_β is the limit that defines the critical delay of tasks (a delay with a value that is greater than L_β is a critical delay), t_{NE} is the time of the new event, and t_β is the time from which further EWSs' occupation is taken into account when generating the agendas (after the start of the simulation, it will take some time to include EWSs' occupation method of selecting the operation). For the experiments of this study, L_β was set to 0 days and t_β was set to approximately 3 months after the simulation start time.

$$w_\beta = \begin{cases} 0; & t_{NE} < t_\beta \\ 1; & d_{max} \leq L_\beta \wedge t_{NE} \geq t_\beta \\ \delta; & d_{max} > L_\beta \wedge t_{NE} \geq t_\beta \end{cases}. \tag{5}$$

To demonstrate the effects of using different scheduling algorithms in different scenarios, the elementary work system EWS_{351} was analyzed in the simulation process. The simulation time (the time of the event, t_{NE}) was chosen on 2010-03-29 at 13:39:06 (until this time the FIFO algorithm was used). At that moment, the EWS_{351} had just finished a task, and in EWS_{351} three other tasks were waiting to be processed. The simulation result for the case of using the FIFO algorithm is shown in Table 2.

The scenario presented in Table 2 is based on the waiting time of the task t_{TW}. This makes it possible to first accomplish task $\boldsymbol{T_1}$, which has the longest waiting time t_{T_1W} = 0:58:29 in the list of tasks for EWS_{351}.

In Table 3 the result for the case of using the EPT algorithm is presented. The EPT alternative agenda

makes possible the first task $\boldsymbol{T_3}$ with the earliest planned start time t_{T_3SPL} = 2010–04–02, followed by the $\boldsymbol{T_1}$ and $\boldsymbol{T_2}$, which has a later planned start time t_{T_1SPL} = 2010–04–06.

Table 2. *FIFO alternative agenda for* EWS_{351}

INPUT DATA			OUTPUT DATA	
SET OF TASKS			FIFO AGENDA	
$\boldsymbol{T}$	Waiting time t_{TW} [h:mm:ss]		$\boldsymbol{T}$	Waiting time t_{TW} [h:mm:ss]
$\boldsymbol{T_1}$	0:58:29		$\boldsymbol{T_1}$	0:58:29
$\boldsymbol{T_2}$	0:58:10	→	$\boldsymbol{T_2}$	0:58:10
$\boldsymbol{T_3}$	0:57:47		$\boldsymbol{T_3}$	0:57:47

Table 3. *EPT alternative agenda for* EWS_{351}

INPUT DATA			OUTPUT DATA	
SET OF TASKS			EPT AGENDA	
$\boldsymbol{T}$	Planned start time t_{TSPL} [yyyy-mm-dd]		$\boldsymbol{T}$	Planned start time t_{TSPL} [yyyy-mm-dd]
$\boldsymbol{T_1}$	2010-04-06		$\boldsymbol{T_3}$	2010-04-02
$\boldsymbol{T_2}$	2010-04-06	→	$\boldsymbol{T_1}$	2010-04-06
$\boldsymbol{T_3}$	2010-04-02		$\boldsymbol{T_2}$	2010-04-06

The simulation result for the case of using the EPT&WSO algorithm is presented in Table 4. The task $\boldsymbol{T_1}$ has the highest value of the indicated function G = 0.453, meaning that this task would, in this case, be the first processed in the EWS_{351}.

Table 4. *EPT & WSO alternative agenda for* EWS_{351}

INPUT DATA			OUTPUT DATA	
SET OF TASKS			EPT AGENDA	
$\boldsymbol{T}$	Planned start time & G		$\boldsymbol{T}$	Planned start time & G
$\boldsymbol{T_1}$	2010-04-06 0.453		$\boldsymbol{T_1}$	2010-04-06 0.453
$\boldsymbol{T_2}$	2010-04-06 0.362	→	$\boldsymbol{T_3}$	2010-04-02 0.409
$\boldsymbol{T_3}$	2010-04-02 0.409		$\boldsymbol{T_2}$	2010-04-06 0.362

The results of the agent deployment in the CPPS concept refer only to the observed EWS_{351}. Thus, the possibility of self-organization within EWS_{351} is demonstrated under the influence of various factors affecting the EWS observed and coming from the realization of the task in the previous EWS or the EWS to further realize the work order that the observed task belongs to.

In the second part of the experiments, each scheduling algorithm is tested in a separate simulation run, for which the output is a resulting production scenario. On this basis, three scenarios are established.

Scenario S1: The self-organization function updates the agenda of a corresponding EWS on the basis of FIFO heuristic algorithm.

Scenario S2: The self-organization function updates the agenda of a corresponding EWS on the basis of EPT heuristic algorithm.

Scenario S3: The self-organization function updates the agenda of a corresponding EWS on the basis of EPT&WSO algorithm.

For the performance analysis of the whole production system from the point of view of applying different scheduling algorithms, the following simulation settings are used in the experiments: the simulation start time is set to 2010–01–04 and the simulation end time to 2011–07–01, meaning that the production is simulated for a period of approximately 18 months.

To measure the effect on the production performance, four performance measures are selected: 1) the distribution of work- order delay times. Generally, the objective is that a work order does not end too late, nor very early; 2) the average work-order delay times influences the average work-order lead times.

The objective is that the work-order lead times are short; 3) the average waiting time for a work order before it is processed at the EWS. The objective is that this time is as short as possible, and 4) the average number of waiting work orders (or tasks) in the EWS. The results of the simulation are presented in Table 5 and Fig. 7.

Table 5. *Results of the simulation for the set time from 2010–01–04 to 2011–07–01*

Heuristic	Average **W0** delay time [day]	**W0** number with a positive delay value	**W0** number with a negative delay value	Average waiting time at **EWS** [s]	Average number of waiting **W0**
Scenario S1	–36.61	7056	7283	551379	11.01
Scenario S2	–33.66	6609	7730	586916	4.56
Scenario S3	–34.66	6716	7623	564221	4.39

Fig. 7 shows the resulting distributions of the work-order delay times for scenarios S1, S2 and S3.

Fig. 7 shows how the manufacturing system performance is significantly better in the scenarios S2 and S3 in comparison to scenario S1, with respect to the distribution of the work-order delay times.

Comparing S3 to S2, the distributions of the work-order delay times are very similar, the number of work orders that are late is increased by 1.6 %, but in the case of the S3 scenario, the average work-order delay time is reduced by more than one day, the average waiting time of the work orders (before they are processed at work systems) is reduced by 6 hours, the work systems are more evenly loaded, and the average number of waiting work orders is decreased by 3.9 %.

The results indicate how the proposed cyber-physical approach to the management and control of a manufacturing system can facilitate the decision making at the level of management and control, and improve the manufacturing system′s performance.

While the realization of the management and control system in the scenarios S1 and S2 is possible just by simple look-ups of the operators into the MES, the realization of the management and control system in the S3 scenario, due to the large-scale and dimensionality of the management and control problem, requires a more advanced approach that can be realized in the form of the proposed cyber-physical approach to the management and control of manufacturing systems. Nevertheless, the realization of the proposed approach would significantly facilitate the management and control process also for the cases of the scenarios S1 and S2.

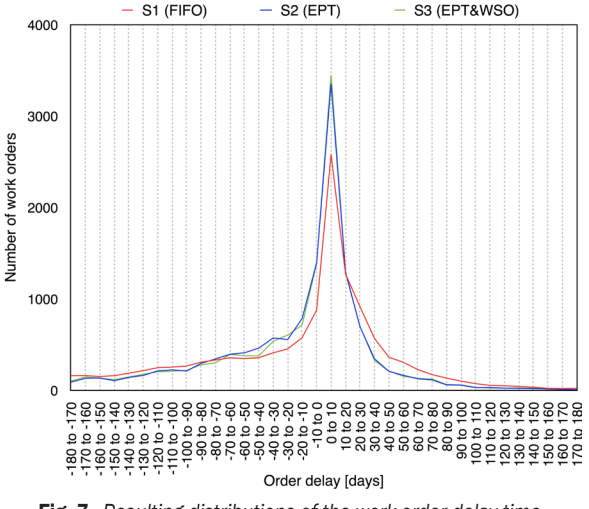

Fig. 7. *Resulting distributions of the work-order delay time, adapted according to* **[28]**

Focused on the proposed approach, a comparison of the simulation results indicates that introducing additional communications between the functions in the cyber system of the CPPS enables a better production performance with respect to the selected performance measures.

The case study was focused on the realization of the cybernated function of the scheduling and the new smart function of the self-organization in the concepts of the CPPS.

4 CONCLUSION

Cyber-physical systems and an advanced manufacturing technology open up new possibilities and potentials in the design, development, management and control of manufacturing systems. Today, manufacturing industry is faced with the technologies of a new industrial revolution – Industry 4.0 and new models for CPPSs. Accordingly, in this paper, a cyber-physical approach to the management and control of manufacturing systems is presented.

First, we structured a new CPPS model based on restructuring the traditional manufacturing structures in the spirit of CPS. Then, the cyber system of the CPPS was introduced and defined. The manufacturing structures in the cyber system enabled the development of a new method for the management and control of manufacturing systems.

The main advantage of a new model CPPS is that the elements of the cyber system of the CPPS enable the management and control of manufacturing systems in real time, through the realization of the digitalized and cybernated functions of the CPPS. The paper presents the approach of digitalization and cybernation of the PPC functions.

The presented approach is demonstrated on a case study based on real industrial data collected from an engineering-to-order company. The case study shows the feasibility and potential of the proposed approach.

Further research will be aimed at the implementation of the presented approach in a real industrial environment.

5 ACKNOWLEDGEMENTS

This work was partially supported by the Slovenian Research Agency, Grant No. P2-0270, by the Public Scholarship, Development, Disability and Maintenance Fund of the Republic of Slovenia, Grant No. 11011-79/2013, and by the Ministry of Higher Education, Science and Technology of the Republic of Slovenia, grant no. 1000-15-0510.

6 REFERENCES

[1] Bauernhansl T. (2013). Industry 4.0: Challenges and Opportunities for the Automation Industry. *7th EFAC Assembly Technology Conference 2013*, Davos.

[2] Tao, F., Cheng, Y., Zhang, L., Nee, Y.C.A. (2017). Advanced manufacturing systems: socialization characteristics and trends. *Journal of Intelligent Manufacturing*, vol. 28, no. 5, p. 1079-1094, **DOI:10.1007/s10845-015-1042-8**.

[3] Lee, E.A. (2008). Cyber Physical Systems: Design Challenges. *11th IEEE International Symposium on Object and Component-Oriented Real-Time Distributed Computing*, Orlando, p. 363-369, **DOI:10.1109/ ISORC.2008.25**.

[4] Monostori, L. (2014). Cyber-physical production systems: Roots, expectations and R&D challenges. *Procedia CIRP*, vol. 17, p. 9-13, **DOI:10.1016/j.procir.2014.03.115**.

[5] Wang, L., Törngren, M., Onori, M. (2015). Current status and advancement of cyber-physical systems in manufacturing. *Journal of Manufacturing Systems*, vol. 37, no. 2, p. 517-527, **DOI:10.1016/j.jmsy. 2015.04.008**.

[6] Liu, Q., Chen, J., Liao, Y., Mueller, E., Jentsch, D., Boerner, F., She, M. (2015). An application of horizontal and vertical integration in cyber-physical production systems. *International Conference on Cyber-Enabled Distributed Computing and Knowledge Discovery*, p. 110-113, **DOI:10.1109/ CyberC.2015.22**.

[7] Monostori, L., Kádár, B., Bauernhansl, T., Kondoh, S., Kumara, S., Reinhart, G., Sauer, O., Schuh, G., Sihn, W., Ueda, K. (2016). Cyber-physical systems in manufacturing. *CIRP Annals*, vol. 65, no. 2, p. 621-641, **DOI:10.1016/j.cirp.2016.06.005**.

[8] Uhlemann, T.H.J., Lehmann, C., Steinhilper, R. (2017). The digital twin: Realizing the cyber-physical production system for industry 4.0. *Procedia CIRP*, vol. 61, p. 335-340, **DOI:10.1016/j.procir.2016. 11.152**.

[9] Cardin, O. (2019). Classification of cyber-physical production systems applications: Proposition of an analysis framework. *Computer in Industry*, vol. 104, p. 11-21, **DOI:10.1016/j. compind.2018.10.002**.

[10] Alcácer, V., Cruz-Machado, V. (2019). Scanning the industry 4.0: A literature review on technologies for manufacturing systems. *Engineering Science and Technology, an International Journal*, vol. 22, no. 3, p. 899-919, **DOI:10.1016/j.jestch.2019.01.006**.

[11] Leitão, P., Rodrigues, N., Barbosa, J., Turrin, C., Pagani, A. (2015). Intelligent products: The grace experience. *Control Engineering Practice*, vol. 42, p. 95-105, **DOI:10.1016/ j.conengprac.2015.05.001**.

[12] Schuhmacher, J., Hummel, V. (2016). Decentralized control of logistic processes in cyber-physical production systems at the example of ESB Logistics Learning Factory. *Procedia CIRP*, vol. 54, p. 19-24, **DOI:10.1016/j.procir.2016.04.095**.

[13] Seitz, K.F., Nyhuis, P. (2015). Cyber-physical production systems combined with logistic models – a learning factory concept for an improved production planning and control. *Procedia CIRP*, vol. 32, p. 92-97, **DOI:10.1016/j. procir.2015.02.220**.

[14] Li, X., Gao, L., Zhang, C., Shao,. X., (2010). A review on integrated process planning and scheduling. *International Journal of Manufacturing Research*, vol. 5, no. 2, p. 161-180, **DOI:10.1504/IJMR.2010.031630**.

[15] Ouelhadj, D., Petrovic, S. (2009). A survey of dynamic scheduling in manufacturing systems. *Journal of Scheduling*, vol. 12, no. 417, **DOI:10.1007/s10951-008-0090-8**.

[16] Pfeiffer, A., Kádár, B., Monostori, L. (2007). Stability-oriented evaluation of rescheduling strategies, by using simulation. *Computers in Industry*, vol. 58, no. 7, p. 630-643, **DOI:10.1016/j.compind.2007.05.009**.

[17] Cauvin, A.C.A., Ferrarini, A.F.A., Tranvouez, E.T.E. (2009). Disruption management in distributed enterprises: A multi-agent modelling and simulation of cooperative recovery behaviours. *International Journal of Production Economics*, vol. 122, no. 1, p. 429-439, **DOI:10.1016/j.ijpe.2009.06.014**.

[18] Zhao, F., Wang, J., Wang, J., Jonrinaldi, J. (2012). A Dynamic Rescheduling Model with Multi-Agent System and Its Solution Method. *Strojniški vestnik – Journal of Mechanical Engineering*, vol. 58, no. 2, p. 81-92, **DOI:10.5545/sv-jme.2011.029**.

[19] Wang, X.L., Huang, H.B., Deng, S. (2012). List scheduling algorithm for static task with precedence constraints for cyber-physical systems. *Acta Automatica Sinica*, vol. 38, no. 11, p. 1870-1879, **DOI:10.3724/SP.J.1004.2012.01870**.

[20] Sluga, A., Butala, P., Peklenik, J. (2001). Self-organization in a distributed manufacturing system based on constraint logic programming. *CIRP Annals*, vol. 50, no. 1, p. 323-326, **DOI:10.1016/S0007-8506(07) 62131-3**.

[21] Schuh, G., Potente, T., Hauptvogel, A. (2014). Methodology for the evaluation of forecast reliability of production planning systems. *Procedia CIRP*, vol. 17, p. 469-474, **DOI:10.1016/j. procir.2014.01.069**.

[22] Zhang, Y., Qian, C., Lv, J., Liu, Y. (2017). Agent and cyber-physical system based self-organizing and self-adaptive intelligent shopfloor. *IEEE Transactions on Industrial Informatics*, vol. 13, no. 2, p. 737-747, **DOI:10.1109/ TII.2016.261889**.

[23] Jiang, Z., Jin, Y., E, M., Li, Q. (2018). Distributed dynamic scheduling for cyber-physical production systems based on a multi-agent system. *IEEE Access*, vol. 6, p. 1855-1869, **DOI:10.1109/ACCESS.2017.2780321**.

[24] Barenji, A.V., Barenji, R.V., Roudi, D., Hashemipour, M. (2017). A dynamic multi-agent-based scheduling approach for SMEs. *The International Journal of Advanced Manufacturing Technology*, vol. 89, no. 9-12, p. 3123-3137, **DOI:10.1007/ s00170-016-9299-4**.

[25] Meissner, H., Aurich, J.C. (2019). Implications of cyber-physical production systems on integrated process planning and scheduling. *Procedia Manufacturing*, vol. 28, p. 167-173, **DOI:10.1016/j.promfg.2018.12.027**.

[26] Peklenik, J. (1995). Complexity in Manufacturing Systems. *CIRP Journal of Manufacturing Systems*, vol. 24, no. 1, p. 17-25.

[27] Butala, P., Sluga, A. (2006). Autonomous work systems in manufacturing networks. *CIRP Annals*, vol. 55, no. 1, p. 521-524, **DOI:10.1016/S0007-8506(07)60473-9**.

[28] Kozjek, D., Vrabič, R., Rihtaršič, B., Butala, P. (2018). Big data analytics for operations management in engineer-to-order manufacturing. *Procedia CIRP*, vol. 72, p. 209-214, **DOI:10.1016/j.procir.2018.03.098**.

List of reviewers who reviewed manuscripts in 2019

Miklós Ákos, Hungary
Nidal H. Abu-Hamdeh, Saudi Arabia
Adam Tadeusz Adamkowski, Poland
Timothy O. Adekunle, USA
Abdulrahaman Shuaibu Ahmad, China
Mohamed M.Z. Ahmed, Egypt
Reza Alayi, Iran
M.T. Albdiry, Iraq
Wael G. Al-Kouz, Jordan
Lutfi Al-Sharif, Jordan
Dario Antonelli, Italy
Andreas Archenti, Sweden
Gianmario Arnulfi, Italy
Kamil Arslan, Turkey
Yunus Ziya Arslan, Turkey
Viktor P. Astakhov, USA
Maja Atanasijević-Kunc, Slovenia
Kean C. Aw, New Zealand
Dhinesh Balasubramanian, India
Mohammad Baraheni, Iran
Mustapha Barakat, France
Paweł Baranowski, Poland
Ioannis Barboutis, Greece
Derzija Begic-Hajdarevic, Bosna & Herzegovina
Ales Belsak, Slovenia
Károly Beneda, Hungary
Juraj Beniak, Slovakia
Josep M. Bergada, Spain
Anton Bergant, Slovenia
Tomaž Berlec, Slovenia
Cristina Maria Biris, Romania
Benjamin Bizjan, Slovenia
Miha Bobic, Slovenia
John Boland, Australia
Miha Boltežar, Slovenia
Gorazd Bombek, Slovenia
Éd Claudio Bordinassi, Brazil
Tomaž Brajlih, Slovenia
Hubert Branger, France
Miha Brojan, Slovenia
Vincenc Butala, Slovenia
Michele Cali, Italy
Caterina Capponi, Italy
Arnaldo Casalotti, Italy
Paolo Casoli, Italy
Onur Çavuşoglu, Turkey
H. Kursat Celik, Turkey
Piotr Cheluszka, Poland
Yikai Chen, China
Peng Cheng, USA
Hyoung Jin Choi, South Korea
Filippo Cianetti, Italy
Snezana Ciric-Kostic, Serbia
Leon Cizelj, Slovenia
Franco Concli, Italy
Eduardo Corral, Spain
Martin Česnik, Slovenia
Matjaž Četina, Slovenia
Danko Ćorić, Croatia
José Gilberto Dalfré Filho, Brazil
J. Paulo Davim, Portugal
Luis Norberto López de Lacalle Marcaide, Spain
Mihael Debevec, Slovenia
Pierre Dehombreux, Belgium
Ivan Demšar, Slovenia
Zlate Dimkovski, Sweden
Anselmo Eduardo Diniz, Brazil
Oana Dodun, Romania
Mateja Dovjak, Slovenia
Jérémie Dumas, USA
Cengiz Erdönmez, Turkey
Patrice Estellé, France
Imre Felde, Hungary
Cuneyt Fetvaci, Turkey
David P. Field, USA
Tomasz Figlus, Poland
Rastko Fišer, Slovenia
Annalisa Fortini, Italy
Livan Fratini, Italy
Alessandro Freddi, Italy
Leonardo Frizziero, Italy
Roman Gabl, UK
Tomislav Galeta, Croatia
Rishi Ganeriwala, USA
Angel Garcia-Beltran, Spain
Siavash Ghanbari, USA
Mehran Ghasempour-Mouziraji, Iran
Mir Hamid Reza Ghoreishy, Iran
Venanzio Giannella, Italy
Gilbert-Rainer Gillich, Romania
Adam Glowacz, Poland

The Editorial would like to thank all the reviewers in participating in reviewing process.
We appreciate the time and effort and greatly value the assistance as a manuscript reviewer for Strojniški vestnik – Journal of Mechanical Engineering.

Vsebina

Strojniški vestnik - Journal of Mechanical Engineering
letnik 66, (2020), številka 1
Ljubljana, januar 2020
ISSN 0039-2480

Izhaja mesečno

Razširjeni povzetki (extended abstracts)

Strojniški vestnik - Journal of Mechanical Engineering 66(2020)1, SI 3

Prejeto v recenzijo: 2019-07-12
Prejeto popravljeno: 2019-10-01
Odobreno za objavo: 2019-10-10

Reševanje pregrevanja v stavbah lahke skeletne gradnje z uporabo fazno spremenljivih materialov

Eva Zavrl[1] – Gašper Zupanc[2] – Uroš Stritih[1] – Mateja Dovjak[2,*]
[1] Univerza v Ljubljani, Fakulteta za strojništvo, Slovenija
[2] Univerza v Ljubljani, Fakulteta za gradbeništvo in geodezijo, Slovenija

Trend lahke skeletne gradnje je vedno bolj popularen, saj so čas in stroški izgradnje običajno manjši. Skeletna gradnja ima slabšo toplotno akumulacijsko sposobnost in je posledično toplotno manj stabilna. S tem je tak tip stavb v poletnem času bolj nagnjen k pregrevanju. Za hlajenje pa se uporabljajo mehanski sistemi, ki rabijo veliko električne energije.

Namen raziskave je reševanje pregrevanja v sezoni hlajenja ter ugotavljanje učinkovitosti zmanjševanja rabe energije s pasivnimi rešitvami, ki za svoje delovanje ne potrebujejo električne energije (pasivni sistem). Tak tip pasivnega sistema so fazno spremenljivi materiali (PCM), ki pri sobni temperaturi spreminjajo fazo in s tem akumulirajo toploto. Z ID Design Builderjem™ je bil izdelan model enodružinske stavbe, ki se nahaja v zmernem podnebju (Ljubljana, Slovenija). Tip zidane nosilne konstrukcije iz opeke je primerjan z lahko gradnjo s PCM. Preizkušeni sta bili dve strategiji PCM (mikroenkapsulirane mavčne plošče in plast z makroenkapsulacijo), tališča (23 °C, 24 °C, 25 °C, 26 °C in 27 °C), različni tipi toplotne kapacitete (kapacitete, M182, M91 M51, M27) in debeline (preiskali in primerjali smo 125 mm in 250 mm) PCM.

Najboljša pasivna rešitev je bila ocenjena na podlagi izbranih parametrov toplotnega ugodja: povprečna občutena temperatura (T_o) v sezoni hlajenja. Dodatna energija, potrebna za hlajenje pri vsaki od raziskanih kombinacij, je bila primerjana z največjim dovoljenim letnim hladom potrebnim za hlajenje določenem v pravilniku PURES. Ugotovljeno je bilo, da je bil najvplivnejši parameter delovanja temperatura tališča plošč PCM.

Na podlagi izbranih meril smo pregrevanje bistveno zmanjšali z uporabo makroenkapsuliranega sloja s tališčem 24 °C in najmanjšo toplotno kapaciteto M51 (največ do 26,3 °C). Težka konstrukcija stavbe je v stavbi omogočala nižjo T_o (27,1 °C) kot kombinacija z mikroenkapsuliranimi mavčnimi ploščami s tališčem pri 23 °C in debelino 250 mm (28,8 °C). Pravilno zasnovana pasivna rešitev se lahko uporabi za izboljšanje načrtovane strategije. Omejitve te raziskave so pomanjkanje simulacij na mikro-skali (CFD), pomanjkanje eksperimentalnih meritev in to, da model ne upošteva toplotnih valov. V tej fazi raziskave smo se osredotočili le na en tip stavbe in nanjo aplicirali različne vrste stavbnih ovojev, pri kateri so bile spremenjene lastnosti materiala (strategija, toplotna kapaciteta in tališče) in ne na več različnih stavb.

Za preprečevanje pregrevanja je potreben celostni pristop, ki temelji na načelih bioklimatskega oblikovanja, kjer je stavba prilagojena podnebnim in lokacijskim značilnostim. Na podlagi raziskave je mogoče ugotoviti, da predstavljeni sistem lahko poveča toplotno ugodje stavbe in zmanjša potrebe po hlajenju. Makroenkapsulirana plast s tališčem 24 °C in toplotno kapaciteto M51 doseže najbolj optimalne rezultate (za najmanjšo količino materiala dobimo najboljši efekt). Potrebe po hlajenju se zmanjšajo z 1,5 kWh/m^2 na 1,25 kWh/m^2 in tako najvišja občutena temperatura znaša 26,3 °C. Z natančnim izborom vplivnih parametrov (tališče, toplotna kapaciteta/debelina) se občutene temperature in raba energije lahke nosilne konstrukcije zmanjšajo (tudi bolj kot pri zidani konstrukciji). Za največjo učinkovitost je potrebno izbrati PCM z optimalno temperaturo tališča, saj napačnega določanja tališča ni mogoče popraviti z dodajanjem toplotne kapacitete (tališče pri 23 °C skoraj nima vpliva na zmogljivost lahke konstrukcije in pri obeh preizkušenih debelinah ne bi mogli zmanjšati pregrevanja). Za pokrivanje različnih temperaturnih območij se lahko uporabijo tudi kombinacije PCM z večplastnimi različnimi tališči. Makroenkapsulirana strategija ima večjo toplotno kapaciteto in je zato bolj praktična za uporabo. Sistem je uporaben za obnovo obstoječih lahkih stavb ali geometrijsko kompleksnih konstrukcij v ovoju stavbe, saj ne izgubi občutljive površine tal v stavbi. Nadaljnje raziskave se bodo osredotočile na kombinacijo numeričnega modela na mikro-in makro skali, na nočno praznjenje materiala in modeliranje najučinkovitejše kombinacije dveh slojev PCM z različnimi tališči. Predvsem pa je potrebno sistem raziskati v realnem okolju enodružinske stavbe.

Ključne besede: reševanje pregrevanja, lahka gradnja, fazno spremenljivi materiali, toplotno ugodje, raba energije, hlajenje

*Naslov avtorja za dopisovanje: Univerza v Ljubljani, Fakulteta za gradbeništvo in geodezijo,
Katedra za stavbe in konstrukcijske elemente, Jamova c. 2, 1000 Ljubljana, Slovenija, mdovjak@fgg.uni-lj.si

Strojniški vestnik - Journal of Mechanical Engineering 66(2020)1, SI 4

Prejeto v recenzijo: 2019-01-15
Prejeto popravljeno: 2019-05-07
Odobreno za objavo: 2019-07-11

Disipacija toplote na zavornih kolutih mirujočih avtomobilov

Stergios Topouris[1] – Dragan Stamenković[2,*] – Michel Olphe-Galliard[1] – Vladimir Popović[2] - Marko Tirovic[1]

[1] Univerza v Cranfieldu, Šola za letalsko in vesoljsko tehniko, transport in proizvodnjo, Združeno kraljestvo
[2] Univerza v Beogradu, Fakulteta za strojništvo, Srbija

Praktično vse objavljene raziskave obravnavajo disipacijo toplote na vrtečih se zavornih kolutih, bodisi v mirujočem zraku bodisi v prečnem toku zraka. Za varnost v prometu pa je zelo pomembna tudi disipacija toplote v stacionarnih razmerah oz. na kolutih, ki se ne vrtijo.

Ko voznik parkira vozilo z ogretimi zavorami, se začnejo zavorni koluti in obloge hladiti in njihova debelina se zmanjšuje, istočasno pa se toplota prenaša tako v okolje kakor tudi v zavorno sedlo, ki se zato širi. Zaradi kombiniranega vpliva teh pojavov se lahko znatno zmanjša pritezna sila, s tem pa tudi torne sile in zavorni moment. Tak scenarij je pogost in potencialno zelo nevaren, saj lahko vozilo, ki je parkirano na klancu, pobegne. Klasične parkirne zavore imajo določen raztezek v poteznem sistemu za vklapljanje, ki do določene mere blaži vpliv zmanjšanja pritezne sile. Z uvedbo električne parkirne zavore (EPB) je treba tovrstnim scenarijem posvetiti veliko pozornosti, saj je sistem zelo tog. Pri vseh sistemih EPB se zato zaradi prej opisanih vzrokov po parkiranju vozila aktivirajo izvršni motorji.

V članku je predstavljena eksperimentalna raziskava disipacije toplote na stacionarnih zavornih kolutih, ki je bila osredotočena na štiri zasnove kolutov: prezračevan kolut z radialnimi krilci, dve vrsti prezračevanih kolutov z ukrivljenimi krilci – brez lukenj in prečno prevrtan, in poln kolut. Eksperimenti so bili opravljeni na namenskem preizkuševališču z električnim ogrevanjem kolutov. Temperatura kolutov med ogrevanjem in ohlajevanjem je bila izmerjena z več termočleni in s termokamero. Preizkusi so dali ponovljive in točne meritve temperature in zanesljive napovedi koeficientov skupnega, konvektivnega in sevalnega prenosa toplote (HTC).

Pridobljene vrednosti HTC so primerljive z rezultati računalniške dinamike fluidov (CFD) za prezračevane kolute z radialnimi krilci in polne kolute, pri čemer so razlike bolj izražene pri prezračevanem kolutu. Meritve temperature kolutov so zanesljive pri kontaktnih (drsnih) termočlenih v fazi ohlajevanja, medtem ko so meritve temperature zraka v izbranih točkah nad kolutom (z žičnimi termočleni) obremenjene z variabilnostjo in izjemno občutljive tudi na najmanjša zračna gibanja v laboratoriju.

Hlajenje kolutov je povsem odvisno od sevanja in od naravne konvekcije, disipacija toplote pa se zmanjšuje s padanjem temperature, zlasti v sevalnem načinu prenosa toplote. Za razliko od disipacije toplote na vrtečih se kolutih, kjer je običajno glavni način disipacije toplote prisilna konvekcija in se konvektivni HTC zmanjšuje s povišanjem temperature, se konvektivni HTC pri stacionarnih kolutih povečuje s porastom temperature. Te vrednosti pa so zelo majhne, običajno med 3 in 5 W/(m^{2}K) za analizirane vrste kolutov in temperaturno območje. Med štirimi analiziranimi zasnovami kolutov ima največjo vrednost koeficienta konvektivnega prenosa toplote kolut z radialnimi krilci, najmanjšo pa polni disk (približno za 30 %). Toplotna prestopnost kolutov z ukrivljenimi krilci je bil za približno 20 % manjši kot pri kolutih z radialnimi krilci, pri čemer je imel prečno preluknjan kolut pri povišanih temperaturah le minimalno prednost.

Ugotovljene so bile tudi razlike med rezultati eksperimentov in CFD za prezračevane kolute. Hitrosti vročega zraka, ki se dviga nad kolutom, so bile manjše od 1 m/s in tako prenizke za eksperimentalno potrditev. Z uporabo generatorja dima in ustrezne merilne naprave pa je bilo mogoče kvalitativno validirati tokovne vzorce za vse štiri zasnove kolutov.

Predmet raziskave je novost, članek pa podrobno obvešča bralce o vseh uporabljenih postopkih in rezultatih. Ti bodo lahko koristni za nadaljnje študije in jih bo mogoče neposredno uporabiti za napovedovanje temperature pri različnih zasnovah kolutov v pogojih stacionarnega hlajenja. V prihodnjih raziskavah bodo uveljavljene višje temperature kolutov s pomočjo indukcijskih grelnikov, kakor tudi naprednejše analize CFD.

Ključne besede: zavorni kolut, disipacija toplote, sevalno hlajenje, konvektivno hlajenje, računalniška dinamika fluidov, naravna konvekcija

*Naslov avtorja za dopisovanje: Univerza v Beogradu, Fakulteta za strojništvo, Kraljice Marije 16, Beograd, Srbija, dstamenkovic@mas.bg.ac.rs

Strojniški vestnik - Journal of Mechanical Engineering 66(2020)1, SI 5

Prejeto v recenzijo: 2019-08-22
Prejeto popravljeno: 2019-11-04
Odobreno za objavo: 2019-12-03

Vpliv parametrov mehanske obdelave na površinsko poroznost zaprto-celične aluminijaste pene

Boštjan Razboršek* – Janez Gotlih – Timi Karner – Mirko Ficko
Univerza v Mariboru, Fakulteta za strojništvo, Slovenija

Aluminijaste pene so eden izmed materialov, ki se šele uveljavlja na področju modernega inženirstva. Njihova uporaba je prisotna na področjih, kjer se zahtevajo lahke konstrukcije, ki morajo prenašati mehanske in termične obremenitve ali morajo imeti sposobnost absorpcije udarne energije. Elementi iz aluminijastih pen, izdelani s penjenjem v kokile, imajo običajno porozno jedro, ki ga obdaja tanka plast neporozne zunanje površine. Ta plast bistveno vpliva na homogenost in mehanske lastnosti elementa, ima pa tudi funkcijo zaščite pred notranjo korozijo. Mehanska obdelava takšnih elementov z odrezovanjem deformira strukturo ter povzroča zarezni učinek, kar ima za posledico zmanjšanje trdnostnih lastnosti. Da bi ohranili trdnostne lastnosti, je potrebno po obdelavi z odrezovanjem izvesti postopek preoblikovanja površine do te mere, da postane obdelana površina neporozna.

Prispevek opisuje eksperimentalni pristop za določanje vpliva parametrov mehanske obdelave aluminijaste pene na površinsko poroznosti. Čeprav so bili postopki inkrementalnega preoblikovanja in tornega valjanja poroznih materialov v preteklosti že preučevani, je to prva študija, kjer je podrobneje raziskan vpliv različnih obdelovalnih parametrov na zmanjšanje poroznosti površine. Za preizkušanje smo uporabili vzorce zaprto-celične aluminijaste pene znanih karakteristik s komercialnim imenom Foamtech®. Vzorce smo pripravili s pomočjo tračne žage z minimalno deformacijo žagane površine. Na CNC obdelovalnem centru smo izvedli obdelavo z inkrementalnim preoblikovanjem ter tornim valjanjem, s čelnim in bočnim delom preoblikovalnega pestiča iz karbidne trdine. Eksperiment je bil zasnovan s polno 3^3 faktorsko analizo tako, da je bil vsak vzorec obdelan z natančno določenimi vhodnimi parametri obdelave (globina preoblikovanja, podajalna hitrost, število vrtljajev). Izdelali smo digitalne fotografije obdelane površine z visoko resolucijo ter jih s pomočjo programske opreme in pragovnega algoritma analizirali. Analizirali smo tudi površino desetih neobdelanih referenčnih vzorcev, katerih srednja vrednost je predstavljala referenčno vrednost poroznosti. Za vsak obdelan vzorec smo, glede na referenčno vrednost, izračunali spremembo površinske poroznosti ter s pomočjo metode odzivnih površin, določili vpliv parametrov obdelave na poroznost obdelane površine.

Iz dobljenih rezultatov preizkušanja smo lahko določili, da spreminjanje parametrov obdelave bistveno vpliva na zmanjšanje površinske poroznosti. Preko 90 % zmanjšanje površinske poroznosti je bilo doseženo z inkrementalnim preoblikovanjem, kot tudi s tornim valjanjem. Maksimalno zmanjšanje je bilo doseženo pri številu vrtljajev 4000 min^{-1}, podajalni hitrosti 200 mm/min ter globini obdelave 6 mm. Iz analiz grafov je bilo mogoče razbrati, da ima globina obdelave največji vpliv na zmanjšanje površinske poroznosti. Sledi ji število vrtljajev, medtem ko ima zmanjšanje podajalne hitrosti manjši vpliv. Zmanjševanje podajalne hitrosti podaljša tudi čas obdelave, kar ni smotrno. Za zmanjšanje površinske poroznosti je tako smiselno povečati število vrtljajev, saj smo pri povečevanju globine obdelave omejeni z obliko elementa.

Zaključimo lahko, da obdelava aluminijastih pen s postopkom inkrementalnega preoblikovanja in tornega valjanja omogoča zmanjšanje površinske poroznosti elementov predhodno obdelanih z odrezovalnimi postopki. Po obdelavi je formirana tanka neporozna površina (ang. *integral skin*), ki pripomore k izboljšanju mehanskih lastnosti končnih elementov. S preoblikovanjem površine se napetostne silnice prerazporedijo, kar zmanjša zarezni učinek. Kljub veliki globini deformacije, le ta zaradi celične zgradbe in dobrih preoblikovalnih lastnosti materiala ostane na lokalni ravni. Kompaktne elemente se tako lahko izdela s kombinacijo odrezovalnih in preoblikovalnih postopkov, ki se izvedejo na istem stroju, kar zmanjša stroške. V primerjavi z maloserijsko proizvodnjo elementov penjenih v kokile, je takšna proizvodnja cenejša, saj odpade izdelava kokil, kot polizdelki pa se lahko uporabijo palice, pločevine ali bloki iz penjenega aluminija. Prihodnje raziskave bodo osredotočene v izdelavo modela za napovedovanje površinske poroznosti ob znanih vhodnih vplivnih veličinah. Poleg globine obdelave, vrtilne hitrosti ter podajalne hitrosti, bomo v model poskusili vključiti tudi karakteristike aluminijaste pene, in sicer gostoto ter velikost celic. S takšnim modelom bo mogoče določiti velikost dodatka po obdelavi z odrezovanjem, da bo z inkrementalnim preoblikovanjem in tornim valjanjem mogoče doseči predvideno površinsko poroznost.

Ključne besede: porozni materiali, aluminijasta pena, mehanska obdelava, inkrementalno preoblikovanje, torno valjanje, površinska poroznost

*Naslov avtorja za dopisovanje: Univerza v Mariboru, Fakulteta za strojništvo, Smetanova ulica 17, 2000 Maribor, Slovenija, bostjan.razborsek@um.si

Strojniški vestnik - Journal of Mechanical Engineering 66(2020)1, SI 6

Prejeto v recenzijo: 2019-07-03
Prejeto popravljeno: 2019-09-02
Odobreno za objavo: 2019-09-24

Konstruiranje mehkega manipulatorja z več zračnimi blazinami z značilnimi parametri in analiza delovanja

Peng Liu – Yonghong Liu* – Ke Wang – Xiaoxuan Wei – Chao Xin – Xinlei Wu
Kitajska univerza za nafto, Kolidž za strojništvo in elektrotehniko, Kitajska

Robotski manipulatorji so preoblikovali industrijske procese. Uporaba klasičnih togih manipulatorjev v tovarnah in v vsakodnevnem življenju je v veliki meri odpravila težka dela ter spodbudila avtomatizacijo in mehanizacijo industrijske proizvodnje. Manipulatorji se vse bolj uveljavljajo v proizvodnji kot odgovor na potrebe po industrijski avtomatizaciji. Klasični manipulatorji so narejeni predvsem iz kovinskih materialov in vključujejo tudi kompleksne nadzorne sisteme za strego ipd. Primer takih sistemov so robotski manipulatorji s šestimi prostostnimi stopnjami. Klasični manipulatorji so zaradi omejitev na področju prilagodljivosti, interaktivnosti in varnosti le omejeno uporabni za delo s predmeti, ki so krhki oz. nepravilnih oblik. Opravljenih je bilo že veliko raziskav na področju pogonov za mehke manipulatorje. Z izboljšanjem pogonov se bodo lahko mehki manipulatorji premikali hitreje in bodo imeli več moči. Kot odgovor na naštete pomanjkljivosti klasičnih manipulatorjev je bil v predstavljeni raziskavi analiziran nov mehki manipulator z več zračnimi blazinami za povečano trenje in njegovo delovanje.

Za novi manipulator je bil izbran pnevmatski pogon in opravljena je bila analiza po metodi končnih elementov. Analiza značilnih parametrov je pokazala, da je bila dosežena optimalna struktura manipulatorja. Nato je bila dokončano konstruiranje in sledila je izdelava mehkega manipulatorja. Deformacija osnovnega materiala manipulatorja je opisana z neo-Hookovo funkcijo deformacijskega dela. Funkcija deformacijskega dela za silika gel je bila preučena skladno z zahtevami analize po metodi končnih elementov za mehke snovi. Neo-Hookova funkcija deformacijskega dela je bila ugotovljena z nateznim preizkusom. Določene so bile materialne lastnosti neo-Hookovega silika gela in koeficienti neo-Hookove funkcije. Na podlagi funkcije je bila izvedena analiza po metodi končnih elementov za preučitev vpliva dimenzijskih parametrov mehkega manipulatorja na upogibno silo. Rezultati teoretične analize potrjujejo pravilnost izsledkov analize po metodi končnih elementov.

Dimenzije mehkega manipulatorja so bile določene na osnovi rezultatov analize po metodi končnih elementov in zahtev glede minimalne debeline sten. Po izdelavi mehkega manipulatorja so bili opravljeni preizkusi upogibnega kota. Sledil je še preizkus prijemanja čaše z vključenim merilnim in nadzornim sistemom mehkega manipulatorja. Masa čaše je bila 147,7 g, dvignjena teža pa se je povečevala z dolivanjem vode. Končna dolita masa vode je bila 150 ml in mehki manipulator je torej dvignil 300 gramov, s čimer sta bila potrjena uspeh optimizacije in uporabnost mehkega manipulatorja.

Ključne besede: manipulatorji, značilni parametri, optimizacija, analiza po metodi končnih elementov, funkcija deformacijskega dela, eksperiment s prijemanjem

*Naslov avtorja za dopisovanje: Kitajska univerza za nafto, Kolidž za strojništvo in elektrotehniko, Changjiang West Road 66, Qingdao, Kitajska, liuyhupc@163.com

Strojniški vestnik - Journal of Mechanical Engineering 66(2020)1, SI 7

Prejeto v recenzijo: 2019-05-27
Prejeto popravljeno: 2019-08-13
Odobreno za objavo: 2019-09-27

Analiza napetosti v cevovodu kot konstrukcijskem elementu hidroelektrarne

Stefan Ćulafić[1,*] – Taško Maneski[2] – Darko Bajić[1]
[1]Univerza v Črni gori, Fakulteta za strojništvo, Črna Gora
[2]Univerza v Beogradu, Fakulteta za strojništvo, Srbija

Analiza napetosti v tlačnih cevovodih je pomembna tako s teoretičnega kot tudi s praktičnega vidika. Napetostnega stanja v posameznih elementih cevovoda, kot so odcepi, ni mogoče izračunati analitično in zato je potreben pristop s kombinacijo numeričnih in eksperimentalnih metod. Pri analizi napetosti nastopi težava, da eksperimentalne študije niso izvedljive v realnih pogojih.

Članek obravnava problem analize napetosti v cevnem odcepu kot najbolj kompleksnem delu cevovoda, ki ne dopušča analitične obravnave. Avtorji so opravili numerično analizo po metodi končnih elementov (MKE) za realni cevni odcep in za model odcepa. Nato so bile opravljene še eksperimentalne raziskave na modelu cevnega odcepa v laboratorijskih pogojih, saj eksperimentalna študija v realnih pogojih na cevnem odcepu ni bila izvedljiva.

Najprej je bila opravljena numerična analiza napetosti po MKE za realni odcep pri različnih vrednostih notranjega tlaka. Ugotovljene so bile vrednosti napetosti v kritični točki odcepa. Nato je bila opravljena še numerična analiza po MKE za model odcepa. Zabeležene so bile vrednosti napetosti v opazovani kritični točki na odcepu zaradi primerjave, ali numerična analiza realnega odcepa in modela odcepa daje rezultate za napetost v opazovani točki, ki so primerljivi v okviru sprejemljive natančnosti. Omeniti je treba, da je model odcepa postavljen na kotlovski enačbi po teoriji podobnosti na osnovi enakosti napetosti za brezmomentne lupine. Narejena je bila tudi primerjava za določitev ujemanja laboratorijskih eksperimentalnih preizkusov modela odcepa z rezultati predhodnih numeričnih analiz. Rezultati so potrdili veljavnost kotlovske enačbe, na osnovi katere je bil izdelan model odcepa. To pa tudi pomeni, da so rezultati eksperimentalnih študij na modelu odcepa veljavni za realni odcep, torej da je napetostno polje v pravem odcepu mogoče opazovati posredno na modelu.

Rezultati predstavljene raziskave so:

- Relacija med napetostmi v opazovanem predelu in notranjim tlakom je zelo zadovoljivo linearna v območju elastičnosti. Napetosti zaradi upogibnega momenta je tako mogoče zanemariti. Poleg tega se odcep v območju elastičnosti vede kot membrana in kotlovska enačba, na osnovi katere je bil postavljen model odcepa, je zato pravilna.
- Določena je mejna vrednost notranjega tlaka, pri kateri napetosti v kritični točki odcepa presežejo območje linearnosti in se vrednost napetosti z dodatnim povečanjem tlaka ne povrne na nič.
- Varnostni faktor ne povzroča nelinearne odvisnosti med napetostjo in notranjim tlakom v odcepu pri realnih obratovalnih pogojih.

Najpomembnejši prispevki članka so:

1. Na osnovi numerične analize realnega odcepa in modela odcepa po MKE ter eksperimentalnih raziskav na modelu odcepa je bilo določeno napetostno stanje odcepa, ki je odvisno od notranjega tlaka. To je teoretični prispevek na področju odpornosti konstrukcij in mehanike deformabilnih teles.
2. Potrjeno je bilo, da je odcep kot element cevovoda mogoče obravnavati kot membrano z zelo zadovoljivo natančnostjo, kar predstavlja pomemben rezultat po teoretični plati.
3. Iz praktičnega vidika je pomembno spoznanje, da je s preizkusom modela mogoče določiti vrednost notranjega tlaka za konkreten realni cevovod, pri kateri izgine linearna povezava med napetostmi in notranjim tlakom. To pomeni, da se pri manjšem povišanju notranjega tlaka signifikantno povečajo napetosti v opazovani točki odcepa. Varnostni faktor se določi za vsak primer posebej.

Ključne besede: cevovod, odcep, hidroelektrarna, analiza napetosti, membrana, mejni tlak, varnostni faktor

*Naslov avtorja za dopisovanje: Univerza v Črni gori, Fakulteta za strojništvo, Blvd. G. Wash., 81000, Podgorica, Črna Gora, sculafic@ucg.ac.me

Strojniški vestnik - Journal of Mechanical Engineering 66(2020)1, SI 8

Prejeto v recenzijo: 2019-05-27
Prejeto popravljeno: 2019-08-13
Odobreno za objavo: 2019-09-27

Kibernetsko-fizični pristop k upravljanju in krmiljenju proizvodnih sistemov

Elvis Hozdić*[1] – Dominik Kozjek[1] – Peter Butala[1, 2]

[1] Univerza v Ljubljani, Fakulteta za strojništvo, Slovenija
[2] Tshwane tehniška univerza, Oddelek za industrijsko strojništvo, Južna Afrika

Industrija 4.0 zlasti na področju informacijskih in komunikacijskih tehnologij (ICT) odpira prostor za popolnoma nove pristope v industrijski proizvodnji in temelji na novih znanstvenih odkritjih, obogatenem znanju, novih materialih ter novih tehnologijah. Nove organizacijske oblike in principi inovativnega upravljanja, samoorganizacija, učenje, odprta inovativna okolja, kolaboracija ter mreženje ljudi in organizacij predstavljajo ključne elemente za transformacijo tradicionalnih proizvodnih sistemov v novo generacijo avtonomnih, distribuiranih in mrežno povezanih proizvodnih sistemov. Pri tem sta digitalizacija in kibernetizacija ključna procesa za preoblikovanje proizvodnih v kibernetsko-fizične sisteme.

Cilj predstavljene raziskave je razvoj novega koncepta kibernetsko-fizičnih proizvodnih sistemov (KFPS), ki bo omogočal preobrazbo proizvodnih v kibernetsko-fizične sisteme, in njegova implementacija na področju upravljanja in krmiljenja, ki je ključnega pomena za učinkovito obvladovanje proizvodnih sistemov v realnem času.

V članku je predstavljen novi generični konceptualni model KFPS. Ključna značilnost tega konceptualnega modela je strukturiranje elementov proizvodnega sistema v tri prostore, to je v: (1) fizični prostor, v katerem so fizični elementi, kot so: stroji, delovni procesi, orodja ipd.; (2) socialni prostor, v katerem so različni subjekti; (3) kibernetski prostor, v katerem so digitalni elementi in prek katerega se povezujejo fizični in socialni elementi. Povezovanje med prostori je realizirano preko komunikacijskih vmesnikov, na katerih prihaja do pretvorbe analognih signalov v digitalne in obratno. Znotraj posameznega prostora je mogoča horizontalna povezava med elementi.

Bistveni element kibernetskega prostora je kibernetski sistem, ki omogoča realizacijo vrste digitaliziranih proizvodnih funkcij, kot so: upravljanje s podatki in znanjem, učenje, simulacije, nadzor, krmiljenje ipd., hkrati pa tudi povezovanje s fizičnimi in socialnimi elementi in mrežno povezovanje v: internet stvari, internet storitev in proizvodne mreže. Kibernetski sistem omogoča tako vertikalno integracijo v kompleksne, sestavljene delovne strukture, kot horizontalno integracijo v različne mrežne strukture.

Na osnovi konceptualnega modela KFPS so izpeljani trije referenčni modeli, ki definirajo osnovne proizvodne strukture na treh nivojih proizvodnega sistema – na nivoju upravljanja, na nivoju vodenja in koordiniranja ter na operativnem nivoju. Raba konceptualnega modela in izpeljanih referenčnih modelov je demonstrirana na primeru planiranja in krmiljenja proizvodnje. Področje planiranja in krmiljenja proizvodnje je zelo zahtevno področje, še posebej v projektni proizvodnji, ki vključuje razvoj proizvoda po naročilu, saj gre za zelo raznoliko proizvodnjo in majhne serije. Njegove funkcije pa obstajajo na vseh nivojih – od nivoja tovarne do nivoja posameznih elementarnih delovnih sistemov.

Problem planiranja in krmiljenja proizvodnje je v tem, da prihaja med izvajanjem dela po urnikih do številnih sprememb in motenj, ki so lahko tudi naključne, vse to pa se izraža v zamudah, prekomernih obremenitvah posameznih delovnih sistemov, izpadih proizvodnje ipd. Gre za kompleksni problem, pri katerem klasični pristopi ne dajejo ustreznih rezultatov.

V članku je predstavljen nov pristop k planiranju in krmiljenju proizvodnje v realnem času na osnovi digitaliziranih in kibernetiziranih funkcij. Koncept je realiziran z uvedbo nove funkcije samoorganizacije, ki omogoča avtonomno odločanje posameznega elementarnega delovnega sistema o svojih aktivnostih, pri čemer upošteva navodila in omejitve nadrejenih organizacijskih in sistemskih struktur. Funkcija samoorganizacije se aktivira ob vsakem novem dogodku (npr. ko je dodeljena nova naloga, ko pride do zakasnitev v izvajanju naloge, ali če pride do alarmnih stanj zaradi napake v sistemu ipd.). Rezultat funkcije samoorganizacije je lokalna agenda oz. vrstni red nalog, ki čakajo na izvedbo v elementarnem delovnem sistemu. Agenda se dinamično prilagaja situaciji v proizvodnem sistemu na osnovi različnih heurističnih algoritmov, s čimer je omogočeno adaptivno upravljanje celotnega proizvodnega sistema.

Demonstracija predloženega koncepta kibernetsko-fizičnih proizvodnih sistemov in novega pristopa k planiranju ter krmiljenju proizvodnje je predstavljena s simulacijskim eksperimentom na osnovi realnih industrijskih podatkov iz podjetja za razvoj in proizvodnjo visokotehnoloških produktov na osnovi naročil. Primerjava rezultatov simulacije, ki so potekale po različnih scenarijih, kaže, da omogoča uvedba funkcije samoorganizacije in dodatnih komunikacij med elementi v kibernetskem sistemu boljšo proizvodno performanco z vidika izbranih kazalnikov uspešnosti.

Ključne besede: industrija 4.0, digitalizacija, kibernetizacija, kiberentsko-fizični proizvodni sistem, planiranje in krmiljenje proizvodnje, samoorganizacija

*Naslov avtorja za dopisovanje: Univerza v Ljubljani, Fakulteta za strojništvo, Aškerčeva 6, 1000 Ljubljana, Slovenija, ehozdic@yahoo.com

Information for Authors

All manuscripts must be in English. Pages should be numbered sequentially. The manuscript should be composed in accordance with the Article Template given above. The maximum length of contributions is 12 pages (approx. 5000 words). Longer contributions will only be accepted if authors provide justification in a cover letter. For full instructions see the Information for Authors section on the journal's website: http://en.sv-jme.eu .

SUBMISSION:

Submission to SV-JME is made with the implicit understanding that neither the manuscript nor the essence of its content has been published previously either in whole or in part and that it is not being considered for publication elsewhere. All the listed authors should have agreed on the content and the corresponding (submitting) author is responsible for having ensured that this agreement has been reached. The acceptance of an article is based entirely on its scientific merit, as judged by peer review. Scientific articles comprising simulations only will not be accepted for publication; simulations must be accompanied by experimental results carried out to confirm or deny the accuracy of the simulation. Every manuscript submitted to the SV-JME undergoes a peer-review process.

The authors are kindly invited to submit the paper through our web site: http://ojs.sv-jme.eu. The Author is able to track the submission through the editorial process - as well as participate in the copyediting and proofreading of submissions accepted for publication - by logging in, and using the username and password provided.

SUBMISSION CONTENT:

The typical submission material consists of:

- A **manuscript** (A PDF file, with title, all authors with affiliations, abstract, keywords, highlights, inserted figures and tables and references),
- Supplementary files:
  - a **manuscript** in a WORD file format
  - a **cover letter** (please see instructions for composing the cover letter)
  - a ZIP file containing **figures** in high resolution in one of the graphical formats (please see instructions for preparing the figure files)
  - possible **appendicies** (optional), cover materials, video materials, etc.

Incomplete or improperly prepared submissions will be rejected with explanatory comments provided. In this case we will kindly ask the authors to carefully read the Information for Authors and to resubmit their manuscripts taking into consideration our comments.

COVER LETTER INSTRUCTIONS:

Please add a **cover letter** stating the following information about the submitted paper:

1. Paper **title**, list of **authors** and their **affiliations**.
2. **Type of paper**: original scientific paper (1.01), review scientific paper (1.02) or short scientific paper (1.03).
3. A **declaration** that neither the manuscript nor the essence of its content has been published in whole or in part previously and that it is not being considered for publication elsewhere.
4. State the **value of the paper** or its practical, theoretical and scientific implications. What is new in the paper with respect to the state-of-the-art in the published papers? Do not repeat the content of your abstract for this purpose.
5. We kindly ask you to suggest at least two **reviewers** for your paper and give us their names, their full affiliation and contact information, and their scientific research interest. The suggested reviewers should have at least two relevant references (with an impact factor) to the scientific field concerned; they should not be from the same country as the authors and should have no close connection with the authors.

FORMAT OF THE MANUSCRIPT:

The manuscript should be composed in accordance with the Article Template. The manuscript should be written in the following format:

- A **Title** that adequately describes the content of the manuscript.
- A list of **Authors** and their **affiliations**.
- An **Abstract** that should not exceed 250 words. The Abstract should state the principal objectives and the scope of the investigation, as well as the methodology employed. It should summarize the results and state the principal conclusions.
- 4 to 6 significant **key words** should follow the abstract to aid indexing.
- 4 to 6 **highlights;** a short collection of bullet points that convey the core findings and provide readers with a quick textual overview of the article. These four to six bullet points should describe the essence of the research (e.g. results or conclusions) and highlight what is distinctive about it.
- An **Introduction** that should provide a review of recent literature and sufficient background information to allow the results of the article to be understood and evaluated.
- A **Methods** section detailing the theoretical or experimental methods used.
- An **Experimental section** that should provide details of the experimental set-up and the methods used to obtain the results.
- A **Results** section that should clearly and concisely present the data, using figures and tables where appropriate.
- A **Discussion** section that should describe the relationships and generalizations shown by the results and discuss the significance of the results, making comparisons with previously published work. (It may be appropriate to combine the Results and Discussion sections into a single section to improve clarity.)
- A **Conclusions** section that should present one or more conclusions drawn from the results and subsequent discussion and should not duplicate the Abstract.
- **Acknowledgement** (optional) of collaboration or preparation assistance may be included. Please note the source of funding for the research.
- **Nomenclature** (optional). Papers with many symbols should have a nomenclature that defines all symbols with units, inserted above the references. If one is used, it must contain all the symbols used in the manuscript and the definitions should not be repeated in the text. In all cases, identify the symbols used if they are not widely recognized in the profession. Define acronyms in the text, not in the nomenclature.
- **References** must be cited consecutively in the text using square brackets [1] and collected together in a reference list at the end of the manuscript.
- **Appendix(-icies)** if any.

SPECIAL NOTES

Units: The SI system of units for nomenclature, symbols and abbreviations should be followed closely. Symbols for physical quantities in the text should be written in italics (e.g. *v*, *T*, *n*, etc.). Symbols for units that consist of letters should be in plain text (e.g. ms^{-1}, K, min, mm, etc.). Please also see: http://physics.nist.gov/cuu/pdf/sp811.pdf .

Abbreviations should be spelt out in full on first appearance followed by the abbreviation in parentheses, e.g. variable time geometry (VTG). The meaning of symbols and units belonging to symbols should be explained in each case or cited in a **nomenclature** section at the end of the manuscript before the References.

Figures (figures, graphs, illustrations digital images, photographs) must be cited in consecutive numerical order in the text and referred to in both the text and the captions as Fig. 1, Fig. 2, etc. Figures should be prepared without borders and on white grounding and should be sent separately in their original formats. If a figure is composed of several parts, please mark each part with a), b), c), etc. and provide an explanation for each part in Figure caption. The caption should be self-explanatory. Letters and numbers should be readable (Arial or Times New Roman, min 6 pt with equal sizes and fonts in all figures). Graphics (submitted as supplementary files) may be exported in resolution good enough for printing (min. 300 dpi) in any common format, e.g. TIFF, BMP or JPG, PDF and should be named Fig1.jpg, Fig2.tif, etc. However, graphs and line drawings should be prepared as vector images, e.g. CDR, AI. Multi-curve graphs should have individual curves marked with a symbol or otherwise provide distinguishing differences using, for example, different thicknesses or dashing.

Tables should carry separate titles and must be numbered in consecutive numerical order in the text and referred to in both the text and the captions as Table 1, Table 2, etc. In addition to the physical quantities, such as *t* (in italics), the units [s] (normal text) should be added in square brackets. Tables should not duplicate data found elsewhere in the manuscript. Tables should be prepared using a table editor and not inserted as a graphic.

REFERENCES:

A reference list must be included using the following information as a guide. Only cited text references are to be included. Each reference is to be referred to in the text by a number enclosed in a square bracket (i.e. [3] or [2] to [4] for more references; do not combine more than 3 references, explain each). No reference to the author is necessary.

References must be numbered and ordered according to where they are first mentioned in the paper, not alphabetically. All references must be complete and accurate. Please add DOI code when available. Examples follow.

Journal Papers:

Surname 1, Initials, Surname 2, Initials (year). Title. Journal, volume, number, pages, DOI code.

[1] Hackenschmidt, R., Alber-Laukant, B., Rieg, F. (2010). Simulating nonlinear materials under centrifugal forces by using intelligent cross-linked simulations. *Strojniški vestnik - Journal of Mechanical Engineering*, vol. 57, no. 7-8, p. 531-538, DOI:10.5545/sv-jme.2011.013.

Journal titles should not be abbreviated. Note that journal title is set in italics.

Books:

Surname 1, Initials, Surname 2, Initials (year). Title. Publisher, place of publication.

[2] Groover, M.P. (2007). *Fundamentals of Modern Manufacturing*. John Wiley & Sons, Hoboken.

Note that the title of the book is italicized.

Chapters in Books:

Surname 1, Initials, Surname 2, Initials (year). Chapter title. Editor(s) of book, book title. Publisher, place of publication, pages.

[3] Carbone, G., Ceccarelli, M. (2005). Legged robotic systems. Kordić, V., Lazinica, A., Merdan, M. (Eds.), Cutting Edge Robotics. Pro literatur Verlag, Mammendorf, p. 553-576.

Proceedings Papers:

Surname 1, Initials, Surname 2, Initials (year). Paper title. Proceedings title, pages.

[4] Štefanić, N., Martinčević-Mikić, S., Tošanović, N. (2009). Applied lean system in process industry. *MOTSP Conference Proceedings*, p. 422-427.

Standards:

Standard-Code (year). Title. Organisation. Place.

[5] ISO/DIS 16000-6.2:2002. *Indoor Air – Part 6: Determination of Volatile Organic Compounds in Indoor and Chamber Air by Active Sampling on TENAX TA Sorbent, Thermal Desorption and Gas Chromatography using MSD/FID.* International Organization for Standardization. Geneva.

WWW pages:

Surname, Initials or Company name. Title, from http://address, date of access.

[6] Rockwell Automation. Arena, from *http://www.arenasimulation.com*, accessed on 2009-09-07.

EXTENDED ABSTRACT:

When the paper is accepted for publishing, the authors will be requested to send an **extended abstract** (approx. one A4 page or 3500 to 4000 characters or approx. 600 words). The instruction for composing the extended abstract are published on-line: http://www.sv-jme.eu/information-for-authors/ .

COPYRIGHT:

Authors submitting a manuscript do so on the understanding that the work has not been published before, is not being considered for publication elsewhere and has been read and approved by all authors. The submission of the manuscript by the authors means that the authors automatically agree to transfer copyright to SV-JME when the manuscript is accepted for publication. All accepted manuscripts must be accompanied by a Copyright Transfer Agreement, which should be sent to the editor. The work should be original work by the authors and not be published elsewhere in any language without the written consent of the publisher. The proof will be sent to the author showing the final layout of the article. Proof correction must be minimal and executed quickly. Thus it is essential that manuscripts are accurate when submitted. Authors can track the status of their accepted articles on http://en.sv-jme.eu/.

PUBLICATION FEE:

Authors will be asked to pay a publication fee for each article prior to the article appearing in the journal. However, this fee only needs to be paid after the article has been accepted for publishing. The fee is 380 EUR (for articles with maximum of 6 pages), 470 EUR (for articles with maximum of 10 pages), plus 50 EUR for each additional page. The additional cost for a color page is 90.00 EUR (only for a journal hard copy; optional upon author's request). These fees do not include tax.

Strojniški vestnik -Journal of Mechanical Engineering
Aškerčeva 6, 1000 Ljubljana, Slovenia, e-mail: info@sv-jme.eu

9 770039 248001
ISSN 0039-2480

http://www.sv-jme.eu

Contents

Papers